

# Wind Tunnel Studies of Shear Stress Partitioning in Live Plant Canopies

THÈSE N° 5403 (2012)

PRÉSENTÉE LE 6 SEPTEMBRE 2012

À LA FACULTÉ DE L'ENVIRONNEMENT NATUREL, ARCHITECTURAL ET CONSTRUIT  
LABORATOIRE DES SCIENCES CRYOSPHÉRIQUES  
PROGRAMME DOCTORAL EN GÉNIE CIVIL ET ENVIRONNEMENT

ÉCOLE POLYTECHNIQUE FÉDÉRALE DE LAUSANNE

POUR L'OBTENTION DU GRADE DE DOCTEUR ÈS SCIENCES

PAR

**Benjamin Andreas WALTER**

acceptée sur proposition du jury:

Prof. C. Ancey, président du jury  
Prof. M. Lehning, Prof. M. Parlange, directeurs de thèse  
Dr C. Gromke, rapporteur  
Dr C. Manes, rapporteur  
Prof. F. Porté Agel, rapporteur



ÉCOLE POLYTECHNIQUE  
FÉDÉRALE DE LAUSANNE

Suisse  
2012



## **Abstract**

The earth's surface is permanently exposed to the atmosphere and accordingly to strong wind forces in many regions. Aerodynamic entrainment, transport and redeposition of sand, soil or snow are able to considerably reshape the surface morphology and influence the environment in areas ranging from deserts to polar regions. Even in moderate climate zones, entrainment and transport of dust, particulate matter and pollen or seeds by wind may have a strong impact on the local atmosphere and vegetation. Many of these processes exert negative influences on our sensitive natural environment. Land degradation, desertification or dust storms, increased particulate matter concentrations in the atmosphere or reduced accumulation of snow in arid regions are just a few examples of the impacts of wind erosion.

Vegetation on the ground can provide an efficient sheltering effect against wind erosion. Plants influence sediment erosion mainly by the following four mechanisms: by reducing the surface exposed to the wind, by trapping particles in motion, by local stress concentration and by absorbing momentum from the flow. The latter results in lower surface shear stress on the ground beneath the plant canopies. The peak of the surface shear stress is responsible for the onset of erosion and the spatial mean is commonly used to estimate particle mass fluxes. To quantify the sheltering effect of vegetation, a method called shear stress partitioning has been extensively investigated in the past. This method determines the fraction of the total fluid stress on the entire canopy acting directly on the substrate surface. However, previous studies have limitations: they were either field-based, mainly using live plants, with the limitation that wind conditions could not be controlled, or from wind tunnels using rigid and non porous plant imitations, that poorly reflect the aerodynamic behaviour of live vegetation. This study takes a new approach, performing shear stress partitioning experiments in a controlled wind tunnel environment to systematically quantify the sheltering effect of live, flexible and porous plants. Subsequently, the data was used to test and improve a theoretical model that predicts the stress partition for vegetation canopies.

This dissertation is divided into four sections. The main results of each section are discussed in this thesis and have also been published as one conference (Chapter 2) and three journal articles (Chapter 3-5).

In Chapter 2, the flow conditions produced in the wind tunnel over live vegetation canopies were investigated to identify the suitability of the boundary-layer flow for these new investigations of shear stress partitioning. Flow characteristics like vertical Reynolds stress and integral length scale profiles and power spectral densities were determined from two-component hot-film anemometry measurements. The results were in good agreement with established literature, suggesting that well developed boundary-layers over live vegetation canopies can be generated in this wind tunnel.

In Chapter 3, the experimental setup and the building, calibration and testing of the measurement technique for measuring surface shear stress in the wind tunnel are presented. The experimental setup consisted of wooden boards in which the live plants, grown in plastic tubes, were arranged in staggered rows. The surface shear stress sensors (Irwin sensors) and the required multi-channel pressure scanner were custom designed and built. Accuracy tests verified that reliable surface shear stress measurements with an average accuracy of about

$\pm 5\%$  can be performed when using a universal calibration function for all Irwin sensors built for this study. The surface shear stress distribution around a single wall-mounted rectangular block was measured as a test case and can serve as high-resolution validation data for CFD simulations.

The surface shear stress distributions on the ground beneath the different densities of live plant canopies were measured with previously unmatched high spatial and temporal resolution, the results of which are presented in Chapter 4. Vertical velocity profiles were measured with a two-component hot-film anemometer to determine the total stress above the canopy as well as additional flow characteristics. For comparison, similar experiments were performed with rigid blocks as substitutes for the plants to systematically investigate the influence of the plants' flexibility and porosity on their sheltering effect against sediment erosion. Several distinctive differences in the sheltering effect of live plants and rigid blocks were found: (i) Flow speed-up around the blocks caused higher peak surface shear stress than in experiments with plants. (ii) The sheltered areas in the lee of the plants are significantly narrower and longer with higher surface shear stress than those found in the lee of the blocks. (iii) The streamlining behaviour of the flexible plants results in a decreasing sheltering effect at increasing wind speeds. (iv) Turbulence intensity distributions close to the ground suggest a suppression of horseshoe vortices in the plant case. Another important result is that the percentage of time when a particle entrainment threshold surface shear stress value is locally exceeded is found to be a useful parameter for determining local erosion and deposition rates.

In Chapter 5, a shear stress partitioning model (Raupach 1992) was tested against the measured data. The model allows the prediction of the total shear stress on the entire canopy as well as the peak and average shear stress ratios. This study is the first, to systematically investigate the model's ability to account for shape differences of various roughness elements. The model can predict the general difference between the plant and the block experiments correctly, although the model limitations were clearly revealed and are discussed in this chapter. The model constant  $c$ , relating the size of an effective shelter area and volume to flow parameters and which was poorly specified prior to this study, was found to have a value of about  $c = 0.27$ . Values for the model parameter  $m$ , which relates the peak surface shear stress to the spatial average shear stress, are difficult to determine because  $m$  was found to be a function of the roughness density, the wind velocity and the roughness element shape. A new, more physically based parameter  $a$  referred to as the peak-mean stress ratio is suggested as a substitute for  $m$  which is solely a function of the roughness element shape. According to this, values for  $a$  are much easier to determine than values for  $m$ . As a result, a method to identify values for the new  $a$ -parameter for different kinds of roughness elements is presented.

**Keywords:** Aeolian processes, Aerodynamic entrainment, Boundary-layer flow, Drag partitioning, Friction velocity, Hot-film anemometry, Irwin sensor, Particle transport, Plant canopy, Shear-stress ratio, Surface shear-stress, Turbulent boundary-layer, Vegetation aerodynamics, Wall-mounted block, Wind erosion, Wind tunnel.



## Zusammenfassung

Die Erdoberfläche ist permanent der Atmosphäre und somit gebietsweise starken Winden ausgesetzt. Von trockenen Sandwüsten bis hin zu schneereichen Polargebieten sind dabei viele Regionen von Erosion und Verfrachtung von Sand, Boden oder Schnee durch Wind geprägt. Auch in gemäßigten Klimaregionen kann Wind durch Feinstaubentstehung oder Pollen- und Samentransport einen starken Einfluss auf die lokale Atmosphäre und Vegetation haben. Viele dieser Prozesse haben allerdings einen negativen Einfluss auf unsere natürliche Umgebung und Gesundheit. Die Verwüstung von fruchtbarem Land, Sand- und Staubstürme, erhöhte Feinstaub-Konzentrationen in der Atmosphäre oder reduzierte Ablagerung von Schnee in trockenen, ariden Gebieten sind nur einige von vielen Beispielen, die aufzeigen wie stark Wind unsere Natur und Umwelt beeinflussen kann.

Vegetation leistet einen hervorragenden Schutz gegen Winderosion. Pflanzen beeinflussen Erosion hauptsächlich durch die vier folgenden Eigenschaften: Sie reduzieren die dem Wind ausgesetzte Bodenoberfläche; sie können mit dem Wind transportierte Partikel abfangen; sie führen zu lokal erhöhten Windkräften auf den Boden und sie besitzen die Fähigkeit, Impuls aus dem Wind zu absorbieren. Letzteres führt dazu, dass die durch den Wind erzeugten Schubspannungen auf den Boden geringer werden. Der Spitzenwert dieser Bodenschubspannungen ist verantwortlich für das Einsetzen von Winderosion und mit dem Mittelwert der Schubspannungen können Partikelmassenflüsse bestimmt werden. Eine Methode zur Quantifizierung der Schutzwirkung von Vegetation gegen Winderosion ist die Bestimmung des Anteils der Gesamtschubspannung oberhalb der Vegetationsdecke, die auf den Boden zwischen den Pflanzen wirkt. Diese so genannte Schubspannungsaufteilung wurde in der Vergangenheit ausgiebig untersucht. Jedoch wurden sämtliche Studien entweder im Freien an natürlichen Pflanzen oder im Windkanal an Pflanzenimitaten durchgeführt. Der Nachteil der Experimente im Freien ist, dass die Windbedingungen nicht kontrolliert werden können, wobei die in Windkanaluntersuchungen verwendeten starren und unporösen Rauigkeitselemente, wie Würfel oder Zylinder, das aerodynamische Verhalten von echten Pflanzen schlecht repräsentieren. Der Ansatz dieser Studie war es die Schubspannungsaufteilung anhand von echten Pflanzen im Windkanal zu untersuchen, um systematisch Einflüsse wie Flexibilität und Porosität der Rauigkeitselemente auf die Schutzwirkung und Modellvorhersagen zu untersuchen.

Die Studie wurde in vier Abschnitte gegliedert. Die Ergebnisse der einzelnen Abschnitte werden in dieser Doktorarbeit vorgestellt und wurden anhand eines Konferenzartikels (Kapitel 2) und drei begutachteter Wissenschaftsartikel in internationalen Fachzeitschriften (Kapitel 3-5) publiziert.

Im ersten Abschnitt (Kapitel 2) wurde die im Windkanal erzeugte Strömung über einer natürlichen Vegetationsdecke untersucht, um die Qualität der Grenzschichtströmung für die weiterführenden Experimente zu ermitteln. Strömungscharakteristiken wie vertikale Profile der Reynolds-Spannung oder des Integralen Längenmasses sowie spektrale Leistungsdichten wurden anhand von Zweikomponenten-Hitzdrahtmessungen bestimmt. Die gute Übereinstimmung der Resultate mit Literaturdaten weist auf eine gut entwickelte Grenzschichtströmung über natürlichen Pflanzendecken hin.

Im zweiten Abschnitt (Kapitel 3) wurde der experimentelle Aufbau sowie die für die Bodenschubspannungsmessungen benötigte Messtechnik konstruiert und im Windkanal getestet. Der Messaufbau besteht aus hölzernen Tischen in denen die in Plastikrohren herangezüchteten echten Pflanzen angeordnet wurden. Die Bodenschubspannungssensoren (Irwin-Sensoren) und die mehrkanalige Druckmessanlage wurden speziell für dieses Projekt konstruiert und gefertigt. Tests zeigen, dass die Bodenschubspannungen unter Verwendung einer universellen Kalibrierfunktion für alle Sensoren mit einer Genauigkeit von  $\pm 5\%$  gemessen wurden. Als Beispiel wird die Schubspannungsverteilung auf den Boden um einen einzelnen, rechteckigen Block mit hoher räumlicher Auflösung präsentiert. Diese Messungen eignen sich gut zur Validierung von CFD Modellen.

Im dritten Abschnitt (Kapitel 4) wurden die Bodenschubspannungen für die unterschiedlich dichten Pflanzendecken mit einer bisher unerreichten räumlichen und zeitlichen Auflösung gemessen. Zusätzlich wurden vertikale Geschwindigkeits- und Reynolds-Spannungs-Profile mit einem Zweikomponenten-Hitzdrahtanemometer gemessen um die Gesamtschubspannung oberhalb der Pflanzendecke sowie andere Strömungsgrößen zu bestimmen. Zum Vergleich wurden Experimente mit starren und unporösen Blöcken anstelle der Pflanzen durchgeführt, um systematisch den Einfluss der Flexibilität und Porosität der Pflanzen auf die Schutzwirkung gegen Winderosion zu untersuchen. Mehrere markante Unterschiede in der Schutzwirkung von echten Pflanzen gegenüber starren Blöcken wurden festgestellt: (i) Die stärkere Beschleunigung der Strömung um die Blöcke verursacht größere Spitzenwerte der Bodenschubspannung im Vergleich zu den Pflanzen. (ii) Die geschützten Flächen im Lee der Pflanzen sind schmaler und länger mit größeren Bodenschubspannungen als die für die Blöcke. (iii) Das stromlinienförmige Ausrichten der Pflanzen mit dem Wind führt zu einer reduzierten Schutzwirkung bei höheren Windgeschwindigkeiten. (iv) Geringe bodennahe Turbulenzintensitäten weisen auf eine Unterdrückung von Hufeisenwirbeln bei Pflanzen hin. (v) Der prozentuale Anteil der Zeit, in der lokal ein Schwellwert für Partikelaufnahme überschritten wird, ist ein nützlicher Parameter um lokale Erosions- und Depositionsraten zu bestimmen.

Im vierten Abschnitt (Kapitel 5) wurde ein theoretisches Modell, mit welchem die totale Schubspannung auf die gesamte Vegetationsdecke sowie deren Anteile an maximalen und mittleren Bodenschubspannungen bestimmt werden können, anhand der Messdaten getestet und modifiziert. Zum ersten Mal wurde das Modell systematisch auf seine Fähigkeit zwischen unterschiedlichen Rauigkeitselementen zu unterscheiden untersucht. Das Modell ist generell in der Lage die Unterschiede richtig wiederzugeben, jedoch werden die Grenzen des Modells aufgezeigt und diskutiert. Die Modellkonstante  $c$ , welche die Größe einer effektiven Schutzfläche und eines effektiven Schutzvolumens mit Strömungsparametern in Beziehung setzt und bislang relativ unspezifiziert war, wurde in dieser Arbeit auf den Wert  $c = 0.27$  bestimmt. Werte für den empirischen Modellparameter  $m$ , welcher den Unterschied zwischen den maximalen und den mittleren Bodenschubspannungen definiert, sind schwer zu bestimmen, da  $m$  von der Rauigkeitsdichte, der Windgeschwindigkeit und der Form der Rauigkeitselemente abhängt. Ein neuer, auf physikalischen Grundlagen basierender Parameter  $a$ , definiert als Quotient aus der maximalen und der mittleren Bodenschubspannung, wurde als alternative zu  $m$  eingeführt, welcher ausschließlich eine Funktion der Form des Rauigkeitselements ist. Demnach sind Werte für  $a$  experimentell

einfacher zu bestimmen als Werte für  $m$ . Eine Methode zur Bestimmung von  $a$  für unterschiedliche Rauigkeitselemente wird vorgestellt.

**Schlüsselwörter:** Aerodynamisches Mitreißen, Windtransport Prozesse, Blockumströmung, Bodenschubspannung, Grenzschichtströmung, Hitzdraht Windgeschwindigkeitsmesser, Irwin Sensor, Partikeltransport, Pflanzendecke, Schubspannungsaufteilung, Schubspannungsgeschwindigkeit, Turbulente Grenzschicht, Vegetationsaerodynamik, Winderosion, Windkanal.



## Acknowledgements

Great thanks to all people that supported my work and that made it possible to bring it to a successful end: My supervisors, colleagues and friends that were involved in the project as well as my family and friends beside work.

Special thanks to Michael Lehning for being an excellent supervisor and thesis director, for his infectious motivation and for bringing me back on the track when I started to loose the red line. I would also like to thank Marc Parlange for taking over the official part of the supervision at the EPFL and Marie-Jose Pellaud for her essential support when struggling with bureaucracy. Thanks also to Fernando Porté-Agel, Christof Gromke, Costantino Manes and Christophe Ancey for reviewing the thesis and being part of the examination committee.

Furthermore, I am very grateful to Christof Gromke for technically supervising my work, for endless fruitful discussions on and off topic and for a great atmosphere in and outside the office. Thanks to Katherine Leonard and Katrin Burri for their great support in many areas, Benjamin Eggert for helping with the wind tunnel experiments and Andrew Clifton for his support when struggling with the measurement techniques.

Thanks also to all my colleagues that supported me during my studies in many aspects ranging from solving theoretical problems to technical support for the measurement techniques and for having a great time at the SLF: Rebecca Mott, Christine Groot Zwaafink, Susanna Hoinkes, Bernadette Köchle, Stefan Horender, Tobias Schuh, Thomas Grünewald, Nander Wever, Frank Graf, Matthias Jaggi, Hans Herranhof, Hansueli Steiner, Charles Fierz, Roland Meister, Christian Simeon, Stuart Bartlett, Silvio Burger, Chris Hughes, Michele Guala, Jan Magnusson, Walter Steinkogler, Marc Stal, Christoph Mitterer, Mathias Gergely, Edgar Schmucki, Fabiano Monti and many more.

My very special thank goes to Daniela Schindler for having an open ear for my problems anytime and for the wonderful time we share. I would also like to thank all my friends and colleagues in Davos for having a great time on the mountains, in the bars and elsewhere. Finally, great thanks to my family for their support during my PhD.

I would also like to thank the Vontobel foundation and the Swiss National Science Foundation (SNF) for financing this project. Thanks also to Costantino Manes for writing the proposal for the funding of this study.



# Contents

|  |           |
|--|-----------|
| Abstract.....  | i         |
| Zusammenfassung .....  | iii       |
| Acknowledgements .....   | vii       |
| <b>1 Introduction .....</b>  | <b>1</b>  |
| 1.1 Motivation .....   | 1         |
| 1.2 Background.....  | 2         |
| 1.2.1 Turbulent boundary-layer and surface shear-stress .....  | 2         |
| 1.2.2 Particle entrainment and transport processes.....  | 3         |
| 1.2.3 Shear-stress partitioning theory.....  | 4         |
| 1.3 Purpose and outline .....  | 5         |
| <b>2 The SLF boundary-layer wind tunnel - An experimental facility for<br/>aerodynamical investigations of living plants .....</b> | <b>7</b>  |
| 2.1 Introduction .....   | 7         |
| 2.2 Basic theory .....   | 8         |
| 2.3 Basic flow characteristics – smooth floor experiments .....  | 9         |
| 2.4 Air flow above living plants .....   | 9         |
| 2.4.1 Streamwise pressure gradients .....  | 9         |
| 2.4.2 The boundary-layer development.....  | 10        |
| 2.4.3 Integral length scales .....   | 10        |
| 2.4.4 The power spectral density (PSD).....  | 11        |
| 2.5 Conclusions .....  | 12        |
| <b>3 Spatially resolved skin friction velocity measurements using Irwin sensors:<br/>A calibration and accuracy analysis .....</b> | <b>13</b> |
| 3.1 Introduction .....   | 13        |
| 3.2 Measurement principles.....  | 14        |
| 3.3 Methods .....  | 16        |
| 3.3.1 Irwin sensor calibration .....   | 16        |
| 3.3.2 Calibration accuracy .....   | 19        |
| 3.4 Results and discussion .....   | 20        |
| 3.4.1 Measurement accuracy .....   | 20        |
| 3.4.2 Validation of the measurement setup .....  | 23        |
| 3.5 Wall-mounted block measurements .....  | 23        |
| 3.6 Summary and conclusions .....  | 26        |

|   |           |
|---|-----------|
| <b>4 Spatio-temporal surface shear-stress variability in live plant canopies and cube arrays.....</b> | <b>27</b> |
| 4.1 Introduction and background .....   | 27        |
| 4.2 Methods.....  | 29        |
| 4.2.1 Flow measurements.....  | 31        |
| 4.2.2 Surface shear-stress sensors .....  | 32        |
| 4.3 Results and discussion .....  | 34        |
| 4.3.1 Flow characteristics.....   | 34        |
| 4.3.2 Shear-stress partitioning.....  | 36        |
| 4.3.3 Surface Shear-stress Spatial Variability.....   | 37        |
| 4.3.4 Time Series Statistics .....  | 40        |
| 4.4 Summary and Conclusions.....  | 43        |
| <b>5 Shear-stress partitioning in live plant canopies and modifications to Raupach’s model.....</b>   | <b>45</b> |
| 5.1 Introduction.....   | 45        |
| 5.2 Background and Theory .....   | 47        |
| 5.3 Methodology .....   | 49        |
| 5.4 Results and discussion .....  | 51        |
| 5.4.1 Total Stress Prediction .....   | 51        |
| 5.4.2 Shear Stress Partitioning .....   | 53        |
| 5.4.3 The $m$ -parameter .....  | 57        |
| 5.4.4 The peak-mean stress ratio $a$ .....  | 60        |
| 5.5 Conclusions and Outlook .....   | 65        |
| APPENDIX: $Re_h$ -independency of $a$ for plants .....  | 67        |
| <b>6 Overall summary and conclusions.....</b>   | <b>69</b> |
| <b>7 Limitations and outlook.....</b>   | <b>73</b> |
| <b>List of symbols: .....</b>   | <b>75</b> |
| <b>Bibliography:.....</b>   | <b>77</b> |



# 1 Introduction

## 1.1 Motivation

In times of global warming and the aggravation of desertification and land degradation, investigations of aeolian processes have become more and more significant in environmental sciences. Processes like the entrainment, transport and deposition of sand, soil, snow, pollen and seeds or particulate matter are directly related to desertification, land degradation, the development of dust storms, air quality or local water storage in the form of snow (e.g. Bagnold 1943 and Shao 2008). These drastic implications of wind erosion on ecosystems and human societies demonstrate the high importance of investigating aeolian processes to identify reasonable and sustainable counteractive measures.

Vegetation canopies are able to reduce wind erosion by providing a significant sheltering effect to inhibit wind erosion of sediments. Plants influence erosion by reducing the area of ground exposed to the wind, by trapping particles in motion, by local stress concentration and by absorbing momentum from the flow, resulting in lower surface shear-stress  $\tau_S$  on the ground beneath the plant canopy (e.g. Wolfe and Nickling 1996). The surface shear-stress  $\tau_S$  is the key to quantifying the sheltering effect of vegetation. The lower the surface shear stress, the better the sheltering effect. Numerous wind tunnel and field investigations of the sheltering effect of plants have been conducted. However, most of these studies used very simplified geometries like solid cylinders, cubes or hemispheres to imitate the plants (Marshall 1971; Wooding et al. 1973; Gillette and Stockton 1989; Musick et al. 1996; Crawley and Nickling 2003; Brown et al. 2008). These solid roughness elements poorly simulate the aerodynamic shape of plants. Live plants have highly irregular structures that can be extremely flexible and porous resulting in considerable changes to the drag and flow regimes relative to rigid imitations (Gillies et al. 2002). On the other hand, field studies using live plants suffer from wind conditions that cannot be controlled (Musick and Gillette 1990; Wolfe and Nickling 1996; Wyatt and Nickling 1997; Lancaster and Baas 1998; King et al. 2006; Gillies et al. 2007). In field experiments it is difficult to decouple the influences of the plants on surface shear-stress from those induced by the variations in the wind. Furthermore, mainly spatially and temporally averaged surface shear stress measurements were performed

so far and only limited data are available on local peak shear-stress values (Crawley and Nickling 2003; King et al. 2006; Brown et al. 2008) or temporal variations of surface shear-stress (Sutton and McKenna-Neumann 2008).

The intention of this study is to improve the understanding and the prediction of the sheltering effect of different dense live vegetation canopies against wind erosion. This especially requires surface shear-stress measurements in live plant canopies under controlled wind tunnel conditions with high spatial and temporal resolution to account for the research gaps identified above. To improve the prediction of the sheltering effect of various vegetation canopies, a comparison of the measured data with a theoretical shear stress partitioning model is required to identify the model's ability in predicting the stress ratios and to modify the model if necessary.

## 1.2 Background

### 1.2.1 Turbulent boundary-layer and surface shear-stress

Wind blowing over the earth's surface frequently results in the development of turbulent boundary-layers with irregular swirls of motion called eddies (Stull 1988). In neutral atmospheric conditions, the frictional drag of the surface on the mean wind results in wind shear which in turn generates large turbulent eddies. These large eddies contain the major amount of turbulent kinetic energy of the boundary-layer and gradually decay to smaller eddies. At the smallest eddies, where viscous forces dominate, turbulent kinetic energy gets dissipated into heat. This process is called the eddy cascade of a turbulent boundary-layer (Fig. 1.1).

A rough wall turbulent boundary-layer can be divided into several layers (Fig. 1.1): First the outer region below the free stream which is characterized by low velocity gradients, low Reynolds stresses and mean velocities close to the free stream velocity. Below, in the inertial sublayer, which is sometimes referred to as the constant stress layer, the Reynolds stress is constant with height indicating a constant vertical flux of horizontal momentum and the mean velocity profile can be approximated by the logarithmic law of the wall. In these two upper layers, the roughness elements have an integral influence on the flow. The flow in the lower layer, the roughness sublayer, is directly influenced by the individual roughness elements and their turbulent wakes. For plant canopies, the upper part of the roughness sublayer around the top of the plants is sometimes called "mixing layer" because vegetation canopies often show typical mixing layer characteristics like the inflection of the mean velocity profile (Raupach et al., 1996). The plant's ability to absorb momentum from the flow results in a reduced downward momentum flux and lower Reynolds stress in the roughness sublayer (Fig. 1.1). Momentum is absorbed by skin friction at the roughness element surface and by form drag induced by the pressure difference between the up and downstream sides of the roughness elements. The lowest few millimetres above the surface, where the viscous forces dominate over the turbulent forces are called the viscous sublayer. The thickness of neutral turbulent

boundary-layers can vary from a few meters for flat grass land with low surface roughness to several hundreds of meters for cities or mountainous regions.

The plant's ability to absorb momentum from the flow in the roughness sublayer and the canopy layer results in a partitioning of the total stress  $\tau$  which acts on the entire canopy: a fraction  $\tau_R$  acting on the plants and a fraction  $\tau_S$  acting on the substrate surface beneath the plants (Fig. 1.1). Schlichting (1936) first defined the shear stress partition as  $\tau = \tau_R + \tau_S$  which was experimentally validated e.g. by Marshall (1971). How strong the surface shear stress  $\tau_S$  is reduced for a certain plant density quantifies the sheltering effect of the canopy because  $\tau_S$  is responsible for the initiation of particle entrainment. In case the surface shear stress  $\tau_S$  locally exceeds a threshold value, the fluid forces on the particles are strong enough to overcome the gravitational and other restoring forces and the particle gets aerodynamically entrained.

### 1.2.2 Particle entrainment and transport processes

In case of larger sediment particles with high gravitational or restoring forces and relatively low surface shear stress induced by the wind,  $\tau_S$  is not strong enough to lift the particles and the sediment rolls over the ground being mostly in contact with the surface. This transport mechanism is called rolling or creeping (Fig. 1.1). For smaller particles and higher surface shear stress,  $\tau_S$  is high enough to aerodynamically entrain the particle although gravitation is still strong enough to force the particle back to the surface. This transport mode, where the particles follow parabolic, ballistic paths near the surface is called saltation (Fig. 1.1). In case of small particles and a high surface shear stress, particles can be aerodynamically entrained and the turbulent boundary-layer results in particles transported over long distances without contacting the surface. This mechanism is called turbulent suspension (Fig. 1.1).

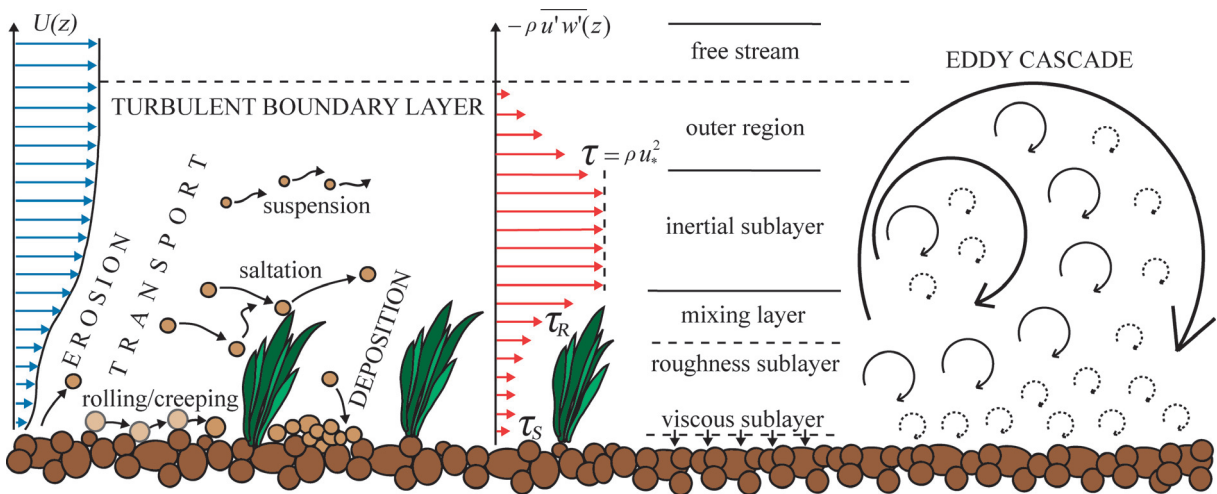


Fig. 1.1: The turbulent boundary-layer. From left to right: Mean wind velocity profile  $U(z)$ ; Aeolian transport processes; Vertical Reynolds stress profile  $\tau(z)$ ; Different Layers and the Eddy cascade of a turbulent boundary-layer.

Typically, all three transport mechanisms occur simultaneously whereas the major fraction of sediment is transported by saltation (Bagnold, 1943). In case of saltation, particles with high momentum collide with the ground transferring a part of their kinetic energy to still particles which get entrained by impact. According to this, particle impact entrainment occurs for shear stress lower than the threshold shear stress for aerodynamic entrainment. The spatial peak surface shear stress  $\tau_S''$  on the ground beneath the plants thus defines the onset of sediment erosion on the ground. The spatial average surface shear stress  $\tau_S'$  can be used to determine magnitudes of particle mass fluxes (e.g., Bagnold 1943). In places with low velocities like in the sheltered areas downstream of a plant, the surface shear stress  $\tau_S$  is typically small enough so that no particle entrainment takes place. Furthermore, particles with high momentum might hit the plant, losing most of their momentum and thus have a high probability of being deposited in these areas (Fig. 1.1).

### 1.2.3 Shear-stress partitioning theory

A shear stress partitioning model that allows the prediction of the total stress  $\tau = \rho u_*^2$  as well as the peak  $(\tau_S''/\tau)^{1/2}$  and the spatial average  $(\tau_S'/\tau)^{1/2}$  shear stress ratios for vegetation canopies of various roughness densities was developed by Raupach (1992) and Raupach et al. (1993). The main equations to calculate the total stress and the stress ratios as functions of parameters describing the geometric and the aerodynamic roughness of the substrate surface and the roughness elements are:

$$\frac{U_h}{u_*} = (C_S + \lambda C_R)^{-1/2} \exp\left[\frac{c\lambda}{2} \left(\frac{U_h}{u_*}\right)\right] \quad (1.1)$$

$$\left(\frac{\tau_S}{\tau}\right)^{1/2} = \left(\frac{1}{(1-\sigma\lambda)(1+\beta\lambda)}\right)^{1/2} \quad (1.2)$$

$$\left(\frac{\tau_S''}{\tau}\right)^{1/2} = \left(\frac{1}{(1-m\sigma\lambda)(1+m\beta\lambda)}\right)^{1/2} \quad (1.3)$$

Here,  $U_h$  is the mean streamwise velocity at the top of the roughness elements,  $u_*$  is the friction velocity,  $C_S$  and  $C_R$  are the surface and the roughness element drag coefficients,  $\lambda$  is the roughness density defined as the roughness element frontal area divided by the ground area per roughness element and  $c$  is a constant of proportionality of  $O(1)$ . The parameter  $\sigma$  is the ratio of the roughness element basal to frontal area,  $\beta = C_R/C_S$  and  $m$  is defined as  $\tau_S''(\lambda) = \tau_S'(m\lambda)$ . A detailed model description can be found in Chapter 5.

The model was extensively tested by several field and wind tunnel studies (e.g., Marshall 1971; Musick et al. 1996; Wolfe and Nickling 1996; Wyatt and Nickling 1997; Crawley and Nickling 2003; King et al. 2006; Gillies et al. 2007; Brown et al. 2008). Most of these shear-stress ratio measurements are generally in good agreement with each other and the

model, however, variations between them exist, resulting from different experimental set-ups, types of roughness elements used and the distribution of the roughness elements over the surface. The field studies are limited by unsteady wind conditions and the wind tunnel studies are limited by the use of rigid and non porous plant imitations as discussed in Chapter 1.1. As a result, a large range of possible values for the model parameters exists. This makes it difficult for modellers to identify appropriate values for a specific vegetation canopy of interest.

### 1.3 Purpose and outline

The purpose of this study is to improve the prediction of shear stress ratios for live plant canopies to obtain more accurate estimates of the sheltering effect of vegetation against wind erosion. This requires spatiotemporally highly resolved surface shear stress and friction velocity measurements within and above plant canopies to capture the air-vegetation interaction in the turbulent boundary-layer. Therefore, highly sophisticated measurement techniques and an extensive experimental setup with live plants are needed to obtain high measurement resolutions and accuracies. The four main objectives of this PhD study can be outlined as follows:

1. Characterization of the turbulent boundary-layer over a live vegetation canopy produced in the SLF wind tunnel.
2. Development, construction and calibration of the surface shear stress measurement technique and determination of the measurement accuracies.
3. Measurements of the surface shear stress in different dense live plant canopies and block arrays and qualitative discussion of the results.
4. Application of a shear stress partitioning model to the data obtained under point 3 to identify the model parameters and to modify the model where necessary.

These four objectives were treated in one conference and three peer-reviewed journal articles. In this thesis, each publication is presented in a separate Chapter:

- Chapter 2: The SLF Boundary-layer Wind Tunnel - An Experimental Facility for Aerodynamical Investigations of Living Plants

*Walter B, Gromke C, Lehning M (2009) The SLF boundary-layer wind tunnel - an experimental facility for aerodynamical investigations of living plants. Proceedings of the 2<sup>nd</sup> International Conference on Wind Effects on Trees, Freiburg, Germany*

Based on two-component hot-film anemometry measurements, the flow conditions over a live vegetation canopy produced in the SLF wind tunnel is investigated to

identify the quality of the turbulent boundary-layer for the investigations on shear stress partitioning.

- Chapter 3: Spatially resolved skin friction velocity measurements using Irwin sensors: A calibration and accuracy analysis

*Walter B, Gromke C, Leonard K, Clifton A, Lehning M (2012a) Spatially resolved skin friction velocity measurements using Irwin sensors: A calibration and accuracy analysis. Journal of Wind Engineering and Industrial Aerodynamics, doi:10.1016/j.jweia.2012.02.018*

In this chapter, the calibration of the surface shear stress sensors (Irwin 1981) and the resulting measurement accuracy is introduced. The main sources of error are quantified and discussed and the measurement technique is validated. The surface shear stress distribution around a single wall-mounted rectangular block is presented and discussed as a test case.

- Chapter 4: Spatio-temporal surface shear-stress variability in live plant canopies and cube arrays

*Walter B, Gromke C, Leonard K, Manes C, Lehning M (2012b) Spatio-temporal surface shear-stress variability in live plant canopies and cube arrays. Boundary-Layer Meteorology, doi:10.1007/s10546-011-9690-5*

The surface shear stress measurements for the different dense live plant canopies and block arrays are presented. The results are used to investigate how the flexibility and porosity of live plants influence the sheltering effect compared to artificial plant imitations used in previous wind tunnel studies. The differences between the plant and the block results are discussed and compared to sand erosion experiments.

- Chapter 5: Shear stress partitioning in live plant canopies and modifications to Raupach's model

*Walter B, Gromke C, Lehning M (2012c) Shear stress partitioning in live plant canopies and modifications to Raupach's model. Boundary-Layer Meteorology, doi:10.1007/s10546-012-9719-4*

In this chapter, the model of Raupach (1992) and Raupach et al. (1993) is tested against the measured shear stress data and the model parameters are determined. The model's ability to distinguish between different kinds of roughness elements and the influence of the live plants flexibility and porosity on the shear stress partition is investigated and discussed. A model modification is suggested which improves its applicability.

The individual methods are presented in each chapter or publication respectively. An overall summary and the conclusions are presented in Chapter 6. The limitations of this study and an outlook on potential future research are presented in Chapter 7.



## **2 The SLF boundary-layer wind tunnel - An experimental facility for aerodynamical investigations of living plants**

*Walter B, Gromke C, Lehning M (2009) The SLF boundary-layer wind tunnel - an experimental facility for aerodynamical investigations of living plants. Proceedings of the 2<sup>nd</sup> International Conference on Wind Effects on Trees, Freiburg, Germany*

### **2.1 Introduction**

Plants affect processes like erosion, transport and deposition of soil and snow that may occur when the atmospheric wind interacts with the ground. A lack of knowledge of the details of these processes exists due to their complexity. So far, artificial plant imitations instead of real living plants have been used in most wind tunnel studies. However, real plants display a highly irregular structure that can be extremely flexible and porous in contrast to the often rigid and non-porous artificial plant imitations. Due to their flexibility, real plants align with the flow at higher wind speeds (streamlining) and considerable changes in drag and flow regimes occur. Accordingly, significant differences in air flow and soil erosion can be expected in contrast to investigations using plant imitations. The novelty of our approach lies in the use of real living plants instead of artificial imitations.

The SLF wind tunnel (Fig. 2.1) is situated at 1640 m a.s.l. in Davos, Switzerland. The wind tunnel has thus far been used to investigate threshold wind speeds for snow transport (Clifton et al., 2006), to investigate snow ventilation (Clifton et al., 2008) and saltation of fresh snow (Guala et al., 2008) and to improve saltation models (Clifton and Lehning, 2008). For this contribution, velocity measurements have been performed using two-dimensional hot-wire anemometry (HWA) to identify the flow conditions produced in the wind tunnel for different setups. Basic flow characteristics over a smooth floor setup without plants and the boundary-layer development over a vegetation covered surface have been investigated. The first has already been analyzed in detail in a previous work (Ambühl, 2004). The latter has been done with and without spires and additional rigid roughness elements in the fetch. Influences of streamwise pressure gradients and the implications on the flow field have been

studied. Integral length scales have been calculated for different positions within the vegetation canopy and compared to literature. Power spectral densities have been determined and compared to the von Karman spectrum. The results provide basic information and are a first step of investigating shear stress partitioning within living plants using Irwin sensors.

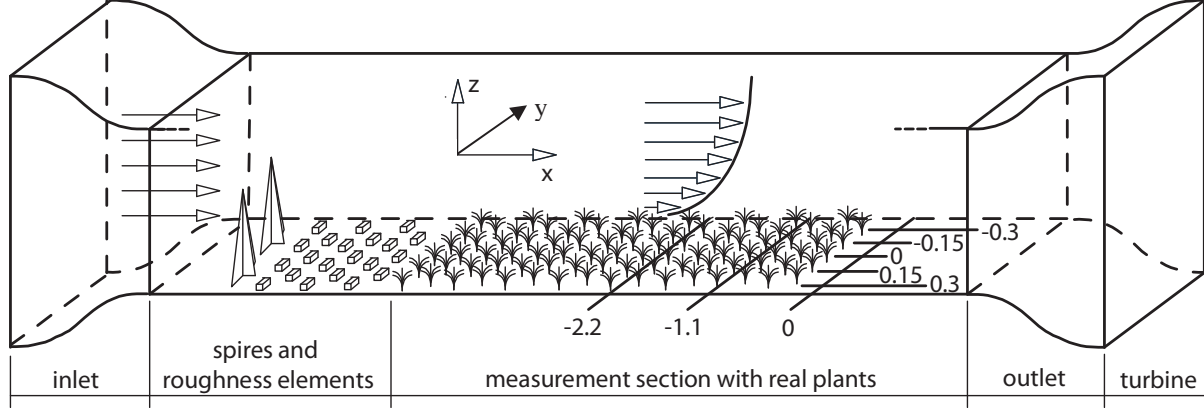


Fig. 2.1: Sketch of the SLF boundary-layer wind tunnel (length  $\times$  width  $\times$  height = 14 m  $\times$  1 m  $\times$  1 m). The wind tunnel operates in suction mode. Measurement positions are denoted. All values are given in meters.

## 2.2 Basic theory

The mean horizontal wind velocity  $u(z)$  in the constant stress layer of a boundary-layer flow can be described by means of the logarithmic law  $u(z) = u_* / \kappa \ln((z-d)/z_0)$  where  $u_*$  is the friction velocity,  $\kappa = 0.41$  the von Karman constant,  $z$  the height above the ground,  $d$  the zero plane displacement height and  $z_0$  the aerodynamic roughness length. Turbulent fluctuations  $u'$ ,  $v'$  and  $w'$  are superimposed to the mean flow  $u$ ,  $v$  and  $w$  in the  $x$ ,  $y$  and  $z$  direction, respectively. Important turbulence characteristics are described by the shear stress velocity  $(-\overline{u'w'})^{1/2} = (\tau_t(z)/\rho)^{1/2}$ , the integral length scale  $L_u(z)$  and the power spectral density  $S_{uu}(f)$  (e.g. Gromke et al., 2005; e.g. Gromke, 2009). The shear stress velocity increases from zero at the surface to a constant value in the logarithmic layer (friction velocity  $u_*$ ) and decreases to zero in the free stream. Using Taylor's hypothesis of frozen turbulence (Stull, 1988), the integral length scale  $L_u(z)$  is defined by

$$L_u(z) = \frac{u(z)}{\sigma_u^2(z)} \int_0^\infty \overline{u'(z,t)u'(z,t+\tau)} d\tau \quad (2.1)$$

where the integrand is the autocorrelation function of  $u'(z,t)$ .  $L_u(z)$  is a measure for streamwise spatial dimensions of the largest gusts. The power spectral density

$$S_{uu}(z, f) = \int_{-\infty}^\infty \overline{u'(z,t)u'(z,t+\tau)} e^{-i2\pi f\tau} d\tau \quad (2.2)$$

is the Fourier transform of the autocorrelation function and gives the distribution of turbulent kinetic energy in the frequency domain.



## 2.3 Basic flow characteristics – smooth floor experiments

Velocity measurements have been performed over a smooth wooden floor in the empty wind tunnel without spires and roughness elements to characterize the basic flow conditions. Vertical profiles of the horizontal velocity  $u(z)$  have been measured at  $x = y = 0$  m (Fig. 2.1) for different free stream velocities  $U_\delta$ . Normalizing the profiles by  $U_\delta$  resulted in a collapse of the velocity profiles (not shown here). Hence, a Reynolds number independent flow is produced. The lateral homogeneity and the influences of the side walls on the air flow have been investigated by means of velocity profiles at five lateral positions. The three profiles around the centre of the tunnel at  $y = -0.15, 0, 0.15$  m and  $x = 0$  m are reasonably homogeneous with mean wind speed  $u(z)$  deviations less than 6% (not shown here). Decelerated wind speeds in the outer velocity profiles next to the side walls are within acceptable limits.

## 2.4 Air flow above living plants

Velocity measurements at various positions between and above real plants (Fig. 2.2) have been performed. Streamwise pressure gradients, the development of the boundary-layer as well as integral length scales and power spectral densities have been investigated and compared to literature data for rough wall turbulent boundary-layers.

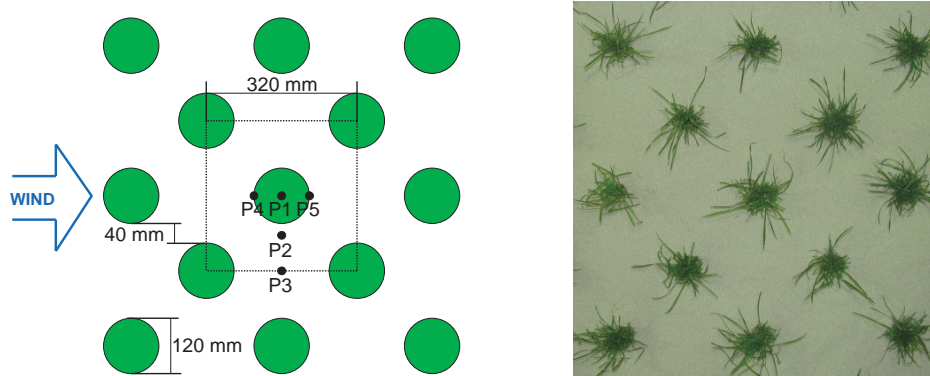


Fig. 2.2: Sketch and photograph of vegetation canopy with measurement positions.

### 2.4.1 Streamwise pressure gradients

Pressure gradients along the flow direction of natural atmospheric boundary-layer flows are negligible on typical wind tunnel dimensions. Hence, prevailing streamwise pressure gradients have to be eliminated in a wind tunnel in order to simulate a natural boundary-layer flow. In a wind tunnel with constant cross section, the free stream velocity  $U_\delta$  has to increase in the  $x$ -direction due to the growth of the boundary-layer thickness  $\delta$ . This results in streamwise negative pressure gradients. The pressure gradients can be avoided by adjusting the ceiling of the wind tunnel in order to keep the free stream velocity constant. As can be seen in Fig. 2.3, in case of a non-adjusted ceiling, the free stream velocity layer is not present

since we find  $du/dx \neq 0$  and  $du/dz \neq 0$  also above the boundary-layer and thus  $(-\bar{u}'w')^{1/2} \neq 0$  as well (profile 5). Contrary, in case of an adjusted ceiling with vanishing pressure gradient, the shear stress velocities  $(-\bar{u}'w')^{1/2}$  are zero indicating the existence of a free stream velocity layer.

## 2.4.2 The boundary-layer development

The boundary-layer above the plants has to be sufficiently developed in the measurement section to perform reliable measurements. Vertical shear stress velocity profiles at various positions are used to investigate the streamwise increase of the boundary-layer thickness  $\delta$  (Fig. 2.3). The boundary-layer thickness  $\delta$  is defined as the height above the ground where  $u(z) = 0.99U_\delta$  and  $-\bar{u}'w' = 0$ . An increase of  $\delta$  from 370 mm at  $x = -2.2$  m to 500 mm at  $x = 0$  m is found (profiles 1-3). Spires and artificial roughness elements in the fetch result in an increased boundary-layer thickness in the measurement section (profile 4). That both  $-\bar{u}'w'$  profiles with and without spires and roughness elements collapse quite well at  $x = 0$  up to a height of  $z \approx 250$  mm (profile 1 and 4) is an indication of a sufficiently developed boundary-layer in the interesting range close to the vegetation canopy.

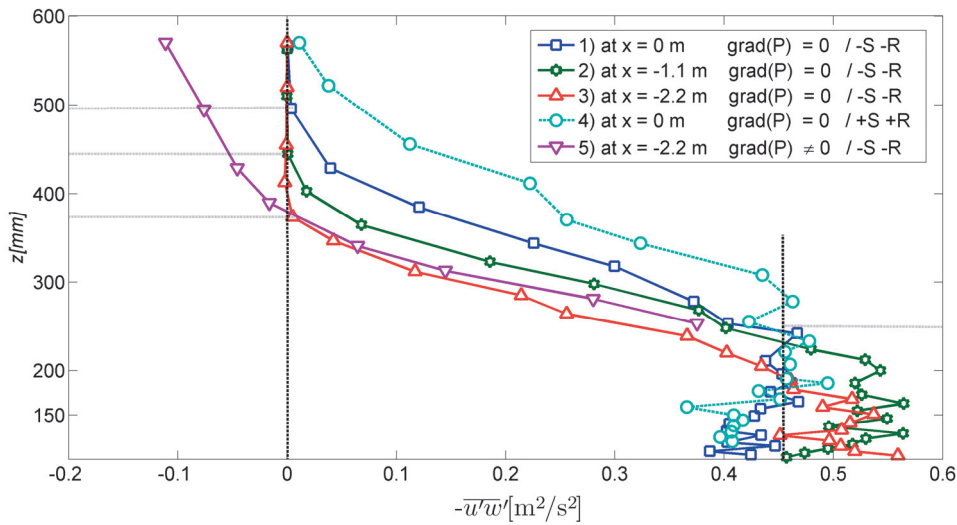


Fig. 2.3: Vertical shear stress velocity profiles  $-\bar{u}'w'$  with and without pressure gradients and with (+S +R) and without (-S -R) spires and roughness elements.

## 2.4.3 Integral length scales

The integral length scales  $L_u(z)$  and  $L_w(z)$  shown in Fig. 2.4 have been calculated at five measurement positions (Fig. 2.2) using Eq. (2.1). A criteria for Taylor's hypothesis is that the turbulence intensity  $I_u(z) = \sigma_u(z)/u(z) < 0.5$ . This is fulfilled for all measurement positions P1-P5. A comparison of the measurements with literature (Raupach, 1991) shows good agreement, with  $L_u/h \approx 1$  and  $L_w/h \approx 0.5$  at the canopy height. A strong decrease of both  $L_u(z)$  and  $L_w(z)$  at  $z/h \approx 1$  is found at the measurement position P5 directly leeward of a plant. The plant accelerates the decay of gusts into smaller scales, which is reflected by smaller integral length scales.

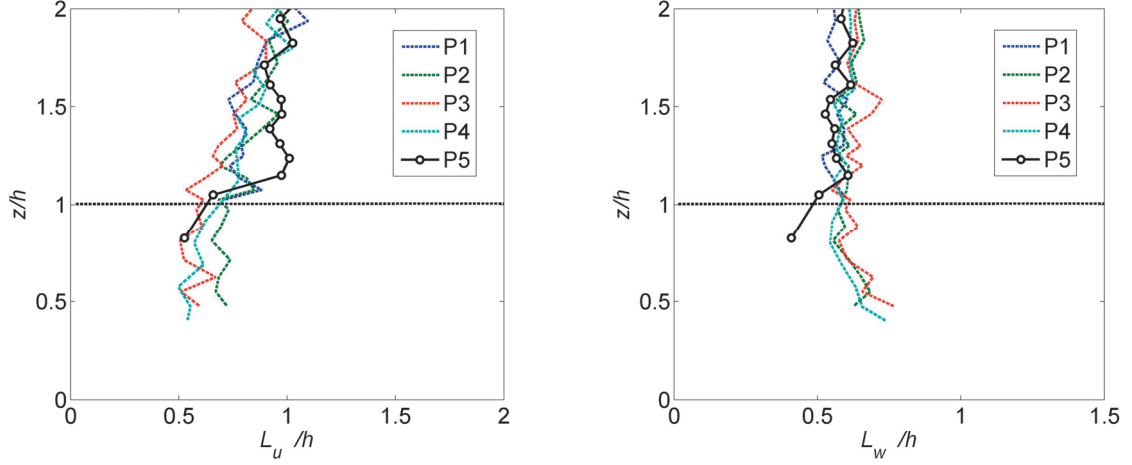


Fig. 2.4: Normalized integral length scale profiles  $L_u(z)/h$  and  $L_w(z)/h$  ( $h$ : canopy height) at positions P1-P5.

#### 2.4.4 The power spectral density (PSD)

The distribution of turbulent kinetic energy in the frequency domain is given by the power spectral density  $S_{uu}(f)$  (Eq. (2.2)) which can be described by the von Karman spectrum (e.g. Gromke, 2009)

$$\frac{f S_{uu}(f)}{\sigma_u^2} = \frac{4 f_n}{(1 + 70.78 f_n^2)^{5/6}} \quad (2.3)$$

with  $f_n = f L_u(z)/u(z)$ . The normalized values of  $S_{uu}(f)$  calculated from a 60 seconds HWA measurement time series ( $f = 20$  kHz,  $z = 450$  mm,  $U_\delta = 15$  m/s) are shown in Fig. 2.5. The measurement data fit the von Karman spectrum well and show the increase of the spectrum in the energy production range up to  $f_n \approx 0.1$ . This range contains the bulk of turbulent kinetic energy, where turbulent kinetic energy is produced by shear. In the inertial subrange, turbulent kinetic energy is neither produced nor dissipated but handed down to smaller scales and the spectrum decreases with a slope of  $m = -2/3$  (Kaimal and Finnigan, 1994). At the high frequency end of the spectrum, turbulent kinetic energy is dissipated and converted into internal energy. This dissipation range is not described by the von Karman spectrum. The smallest structures of a turbulent flow in the dissipation range are called the Kolmogorov micro-scales. They are governed by the dissipation rate  $\varepsilon$  and the kinematic viscosity  $\nu$ . The Kolmogorov time scale is defined as  $\tau_k = (\nu/\varepsilon)^{1/2}$  (Wissink, 2006). In our case,  $\tau_k$  can be estimated using  $\nu = \nu_{air} = 1.5 \cdot 10^{-5}$  m<sup>2</sup>/s and  $\varepsilon \sim U^3/L$  where  $U$  and  $L$  are characteristic macroscopic velocity and length scales. The corresponding frequency  $f_n^{Kolmogorov}$  is calculated by

$$f_n^{Kolmogorov} = \frac{1}{\tau_k} \frac{L_u(z)}{u(z)} \quad (2.4)$$

and is also shown in (Fig. 2.5). With  $U = u(z) = 13.7$  m/s and  $L \approx \delta \approx 0.5$  m,  $f_n^{Kolmogorov} \approx 300$  and is within one order of magnitude with the smallest scales as seen from the measured spectrum.

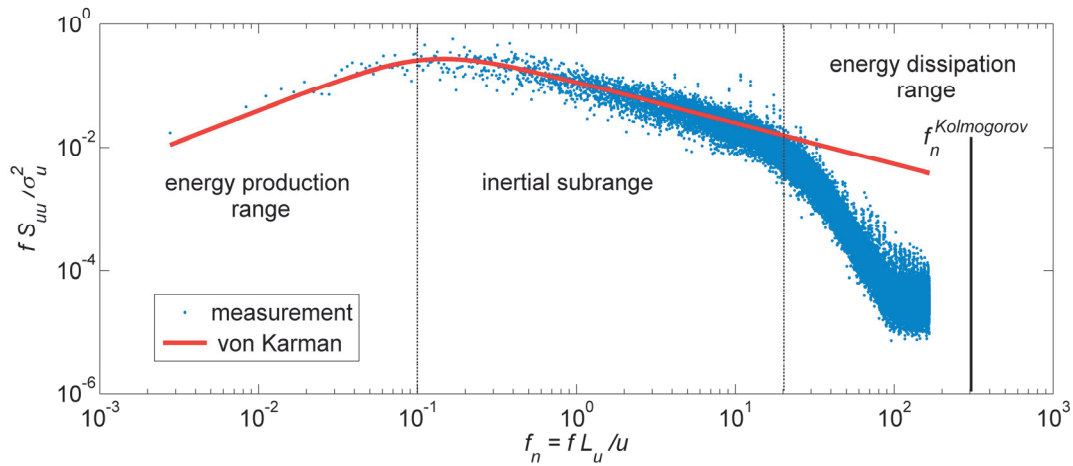


Fig. 2.5: Measured normalized power spectral density  $S_{uu}(f)$  and von Karman spectrum given by Eq. (2.3).

## 2.5 Conclusions

The investigations show that the SLF boundary-layer wind tunnel is well suited for future experiments on shear stress partitioning with living plants using Irwin sensors. The adjusted ceiling allows producing boundary-layer flows with vanishing pressure gradients resulting in sufficiently developed boundary-layers in the measurement section. Spires and additional roughness elements in the fetch lead to an increased boundary-layer thickness over the plant canopy. The comparison of integral length scales and power spectral densities show good agreement with established literature data.

## Acknowledgement

The authors are indebted to the Vontobel Foundation and the Swiss National Science Foundation (SNF), Switzerland, for funding this research project.

# 3 Spatially resolved skin friction velocity measurements using Irwin sensors: A calibration and accuracy analysis

Walter B, Gromke C, Leonard K, Clifton A, Lehning M (2012a) Spatially resolved skin friction velocity measurements using Irwin sensors: A calibration and accuracy analysis. *Journal of Wind Engineering and Industrial Aerodynamics*, doi:10.1016/j.jweia.2012.02.018

## 3.1 Introduction

The fluid dynamic shear-stress  $\tau_s$  acting on surfaces under various flow conditions is of great interest to researchers in fields ranging from aerospace engineering to sedimentary geology. Surface shear-stress measurements are essential for either applied industrial or fundamental scientific investigations of fluid dynamical problems. Additionally, such measurements provide valuable data for validating CFD models. In environmental fluid mechanics, the surface shear-stress  $\tau_s = \rho u_\tau^2$ , where  $u_\tau$  is the skin friction velocity and  $\rho$  the air density, is useful in understanding processes including soil erosion, drifting snow and particulate matter entrainment. The maximum of  $\tau_s$  defines the onset of particle erosion when it exceeds some threshold value, and its spatiotemporal average can be used to quantify particle mass fluxes on surfaces. For any such study, the surface shear-stress or the skin friction velocity needs to be measured as precisely as possible, ideally with a high spatial and temporal resolution. However, different types of experiments require different measurement techniques depending on basic conditions like the fluid used or the spatial dimensions of the experiment. Wind tunnel or field experiments investigating sediment erosion for example require very robust sensors because of relatively harsh ambient conditions.

A wide range of techniques for measuring surface shear-stress in boundary-layer flows have been developed, from very simple to highly sophisticated sensors (e.g. Haritonidis, 1989). A simple, well known sensor that is practical and relatively easy to use is the Preston tube (Preston, 1953) which is actually a circular pitot tube lying on the surface. The pressure difference between the dynamic pressure measured at the Preston tube and the static pressure can be related to the local skin friction velocity. A disadvantage of the Preston tube is its directionality, making it of limited use in 3D flows. Nowadays, so-called Micro-Electro-Mechanical Systems (MEMS) are often used for measuring surface shear-stress. These sensors transform the mechanical shear-stress of the fluid on the sensor into an electrical

signal (e.g. Ho and Tai, 1998). A recently developed technique is the Micro-Pillar Shear-Stress sensor (MPS<sup>3</sup>) which uses thin cylindrical structures on a surface immersed in the viscous sub-layer that bend due to the fluid stress together with optical detection techniques (Grosse and Schröder, 2009). MEMS and MPS<sup>3</sup> sensors are very sensitive and relatively difficult to use, thus they have not been widely used in environmental fluid mechanics studies to date.

The Irwin sensor (Irwin, 1981) is a device for measuring local pressure differences close to a wall. It is similar to the Preston tube in that it can be calibrated against skin friction velocities  $u_\tau$ . The pressure difference is measured between a small sensor tube protruding into the boundary-layer and a pressure tap around the sensor tube flush with the ground. Irwin sensors are axially symmetric and require no alignment with the direction of the flow making them suitable for 3D flows, which is an advantage over the Preston tube. The measurement principle of the Irwin sensors is discussed in the following section (Section 3.2). Irwin sensors have been widely used and their functionality has been confirmed by various environmental fluid mechanics studies investigating shear-stress partitioning for vegetation canopies (e.g. Crawley and Nickling, 2003; Walter et al, 2012a) as well as in wind comfort studies measuring pedestrian level wind velocities (e.g. Durgin, 1992; Wu and Stathopoulos, 1993).

Modern instrumentation allows the simultaneous measurement of pressure differences  $\Delta p$  of a multitude of Irwin sensors enabling instantaneous determination of the spatial distribution of skin friction velocity on a surface. However, determining several individual calibration functions for each Irwin sensor used for the measurements is very time consuming, especially when the sensors need to be reinstalled between different measurement setups. Such rearrangement of the sensors requires a recalibration of each sensor for each new setup, because the degree to which a sensor is mounted flush with the ground and the sensor location in the wind tunnel has an influence on the sensor performance. The goal of this study is to investigate the measurement accuracy when using multiple Irwin sensors together with a universal calibration function to measure spatially resolved but temporally averaged skin friction velocity distributions on the ground, e.g. beneath wall mounted obstacles.

The experimental methods used in this study and the determination and the accuracy of the universal calibration function are introduced in Section 3.3. Section 3.4 deals with the accuracy and the validation of the whole measurement setup (the measurement technique together with the experimental setup in the wind tunnel). Finally, in Section 3.5 the skin friction velocity distribution around a single wall-mounted rectangular block is presented, discussed and compared to literature data.

## 3.2 Measurement principles

Fig. 3.1a shows an engineering drawing of an Irwin sensor (cross-sectional view) as used in the SLF (WSL Institute for Snow and Avalanche Research, Davos, Switzerland) wind tunnel. The sensor consists of a small cylindrical body with a pressure tap (sensor tube) protruding out of the sensor into the turbulent boundary-layer up to a height  $h$ . The sensor plate is mounted flush with the wind tunnel floor, leaving the small tube exposed to the flow. A pressure similar to the static wall pressure is available at a second pressure tap that is located around the sensor tube (the sensor hole). Both the sensor tube and hole are connected to the





universality of this calibration function is an advantageous result because it can be used for a range of varying Irwin sensor geometries or  $h/d$  ratios. Wu and Stathopoulos (1993) investigated interference effects of the sensor tubes and found no significant influence if the distance between the sensor tubes is greater than  $14d$  in the streamwise direction and  $5d$  in the direction transverse to the flow. All sensors used in this study were further apart than this ( $30d$  in the streamwise direction and  $13d$  in the direction transverse to the flow).

### 3.3 Methods

All experiments presented in this study were performed in the SLF boundary-layer wind tunnel. This wind tunnel has a cross section of  $1\text{ m} \times 1\text{ m}$ , an 8 m long test section and a 6 m long fetch upwind of the test section. It operates in suction mode and has an adjustable ceiling to allow the development of boundary-layers with negligible streamwise pressure gradients over various surfaces (e.g. Clifton, 2007; Walter et al, 2009). The acceleration parameter  $K$ , defined as  $K = \nu/U_\delta^2 (dU_\delta/dx)$ , where  $U_\delta$  is the free stream velocity and  $x$  the direction of the flow, can be used to assess streamwise pressure gradients and is typically smaller than  $1 \times 10^{-8}$  in the SLF wind tunnel. This indicates a nearly zero streamwise pressure gradient (Schultz and Flack, 2007). The tunnel has recently been used to investigate the sheltering effect of live plants against soil erosion (Burri et al, 2011a; Burri et al, 2011b; Walter et al, 2012a) and for investigations of snow-wind interaction (Clifton et al, 2006; Clifton et al, 2008; Guala et al, 2008; Gromke et al, 2011). In general, spires and artificial roughness elements (referred to hereafter as S&R) are used in the SLF wind tunnel on the fetch upwind of the test section to facilitate the boundary-layer development. However, while beneficial for our former sediment transport experiments with saltating sand or snow, the use of S&R bears some difficulties for non particle laden flows, as will be discussed later in section 3.3.1.

All hot-film and Irwin sensor measurements were performed at the downwind end of the 8 m test section covered with smooth wooden plates (Fig. 3.1b). Our Irwin sensor dimensions closely follow the specifications presented by Irwin (1981) with the same diameters for the sensor hole ( $D = 2.6\text{ mm}$ ) and tube (external diameter  $d = 1.7\text{ mm}$ ) (Fig. 3.1a). The pressure differences  $\Delta p$  of the Irwin sensors were measured using a custom made 32-channel pressure scanner (range:  $\pm 100\text{ Pa}$ , accuracy:  $\pm 0.2\text{ Pa}$  typically, sampling rate: 200 Hz). The pressure transducers used in the pressure scanner are from *Sensortronics GmbH* (part number: *HCLA02X5*). Measurements of the friction velocity  $u_*$  in the constant stress layer and the mean wind velocity  $U$  were obtained using two-component hot-film anemometry (e.g. Bruun, 1995). The hot-film anemometer (*Dantec, Streamline*) was validated against a calibrated fan anemometer (*Schiltknecht, MiniAir*) prior to each experiment.

#### 3.3.1 Irwin sensor calibration

In this section we present a procedure to determine a universal calibration function, similar to that from Eq. (3.2), which can be used for a multitude of Irwin sensors. In the process, a set of four Irwin sensors with tube heights  $h = 1.7, 3, 5$  and  $7\text{ mm}$  was used and calibrated against the friction velocities  $u_*$  measured with the two-component hot-film anemometer in the constant stress layer. For the calibration,  $u_*$  and  $\Delta p$  at the four Irwin sensors were



simultaneously measured in a turbulent boundary-layer at nine different free-stream velocities ranging from  $U_\delta = 2 - 18 \text{ m s}^{-1}$ . The boundary-layer was assumed to be well-developed and in equilibrium at the downwind end of the test section as found by Walter et al. (2009). For an equilibrium boundary-layer, the friction velocity  $u_*$  in the constant stress layer is equal to the skin friction velocity  $u_\tau$  at the surface (e.g. Stull, 1988).

To determine  $u_*$ , the cross correlation  $-\overline{u'w'}$  of the fluctuating parts  $u'$  and  $w'$  of the mean streamwise  $U$  and vertical  $W$  velocity components were averaged over the constant stress layer, e.g. the height-level where the maximum values of  $-\overline{u'w'}$  vary less than  $\pm 10\%$ . Fig. 3.2 shows the normalized mean velocity profile  $U(z)/U_\delta$  and the normalized kinematic Reynolds stress profile  $-\overline{u'w'}(z)/u_*^2$  for a free stream velocity of  $U_\delta = 16 \text{ m s}^{-1}$  ( $u_* = 0.51 \text{ m s}^{-1}$ ) in a case with S&R on the flow preconditioning fetch. For the purpose of comparison, Fig. 3.2 includes the Reynolds stress profile at the same  $U_\delta = 16 \text{ m s}^{-1}$  but measured without S&R.

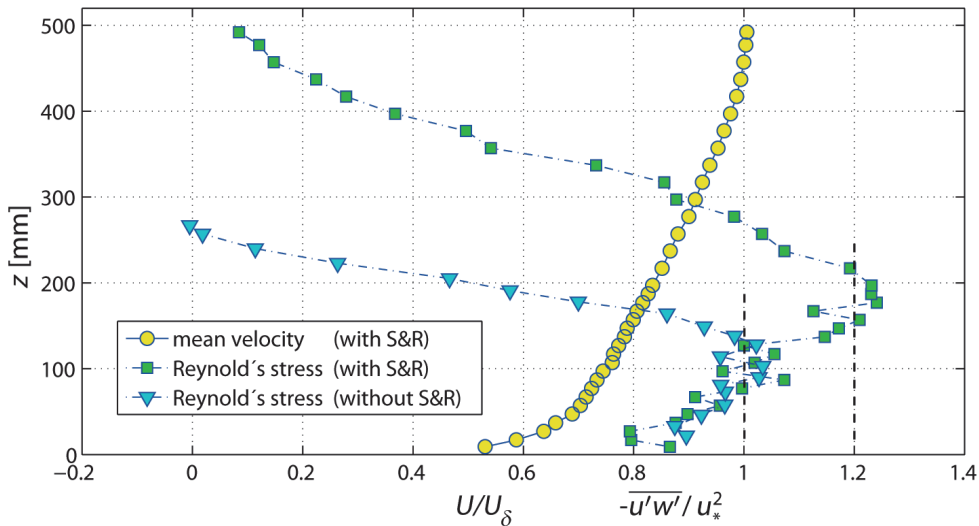


Fig. 3.2: Normalized vertical profiles of the mean velocity  $U(z)$  and the kinematic Reynolds stress  $-\overline{u'w'}(z)$  (with and without spires and artificial roughness elements) measured with two-component hot-film anemometry for a wooden wind tunnel floor (free stream velocity:  $U_\delta = 16.0 \text{ m s}^{-1}$ ; friction velocity:  $u_* = 0.51 \text{ m s}^{-1}$ ).

Both  $-\overline{u'w'}(z)$  profiles match very well up to a height of  $z = 150 \text{ mm}$ . However, the S&R result in the development of an internal boundary-layer (e.g. Stull, 1988). Whereas the constant stress layer without S&R is in-between  $50 \text{ mm} < z < 150 \text{ mm}$ , the profile with S&R exhibits two constant stress layers. The lower one is at the same level as the constant stress layer measured without S&R and belongs to the internal boundary-layer developing over the smooth wooden floor. The residual layer above, which also appears as a constant stress layer with Reynolds stresses being 20% higher than in the first, originates from the flow conditioning by the S&R. The boundary-layer thickness  $\delta$  is defined as the height where  $U(z) = 0.99 \times U_{max}$  or  $-\overline{u'w'} = 0$  and increases strongly from  $\delta \approx 250 \text{ mm}$  in the case without S&R to  $\delta \approx 500 \text{ mm}$  in the case with S&R. For the following measurements presented in this manuscript, S&R were used and the friction velocities  $u_*$  were determined in the constant stress layer of the internal boundary-layer ( $z < 150 \text{ mm}$ ). The variation of  $-\overline{u'w'}$  in the constant stress layer was typically less than  $\pm 5\%$  (one standard deviation). The collapse of

both Reynolds stress profiles in the constant stress region of the smooth floor boundary-layer (Fig. 3.2) suggests that the S&R did not influence the skin friction velocity measurement results presented in this study. The fact that the normalized  $U(z)/U_\delta$  profiles vary less than 1.5% between  $U_\delta = 8 - 16 \text{ m s}^{-1}$  (not shown here), proves that a Reynolds number independent flow was generated in the wind tunnel.

In parallel with the hot-film measurements, the pressure differences  $\Delta p$  were measured at the four Irwin sensors using the multi channel pressure scanner. Since the pressure difference  $\Delta p$  increases either with tube height  $h$  or with wind velocity, different tube heights  $h = 1.7, 3, 5$  and  $7 \text{ mm}$  and free-stream velocities  $U_\delta = 2 - 18 \text{ m s}^{-1}$  were chosen. As a result, a large range of pressure differences and thus calibration range is covered which improves the quality and universality of the calibration function.

Fig. 3.3 shows Irwin's original calibration function (Eq. (3.2)) together with our calibration data and our fit to the data:

$$\frac{u_\tau h}{\nu} = 6.0 + 0.181 \left( \frac{\Delta p h^2}{\rho \nu^2} \right)^{0.461} \quad (3.3)$$

The kinematic viscosity of air was  $\nu = 1.76 \times 10^{-5} \text{ m}^2 \text{ s}^{-1}$  and the air density  $\rho = 1.02 \text{ kg m}^{-3}$  for the calibration measurements. Note that the SLF wind tunnel is located 1650 m above sea level.

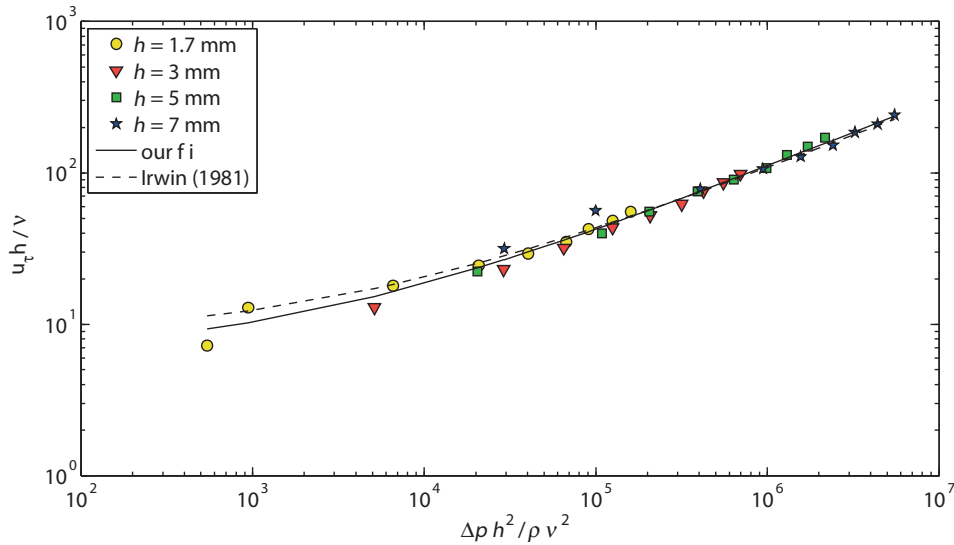


Fig. 3.3: Calibration data of four Irwin sensors with different tube heights  $h$  together with our universal calibration (our fit,  $R^2 = 0.992$ ) function and the original calibration function from Irwin (1981).

The calibration data and our universal calibration function show excellent correlation with Irwin's original calibration (Eq. (3.2) and (3.3), Fig. 3.3) supporting the validity of Eq. (3.1) as well as the high accuracy of our friction velocity measurements with the hot-film anemometer. Stronger deviations of the calibration data from the fit at low pressure differences for each Irwin sensor are mainly a result of the limited accuracies of the Irwin sensors and the pressure scanner at low wind velocities (Fig. 3.3). The use of this universal calibration function for each sensor results in slightly reduced but still good accuracies as discussed in the following sections. Nevertheless, an intercomparison of all sensors prior to the measurements needs to be carried out to guarantee their functionality and to reject sensors

with poor agreement with the sensors used for the calibration and thus the universal calibration function. Measuring the Irwin sensors used for the calibration simultaneously with the ones that need to be tested on a smooth wooden floor and comparing the pressure differences  $\Delta p$  provides a quick performance test.

### 3.3.2 Calibration accuracy

In this section, we demonstrate that the universal calibration function (Eq. (3.3)) results in only slightly lower calibration accuracies relative to individual calibration functions for each Irwin sensor. Fig. 3.4 shows the normalized deviations of the skin friction velocity measured with the hot-film anemometer  $u_{\tau, HF}$  to those calculated using the calibration function  $u_{\tau, cal}$  plotted against  $u_{\tau, HF}$ . This represents the deviations of the calibration measurement data in Fig. 3.3 from the fitted curve parallel to the ordinate. The free stream velocities for the calibration ranged from  $U_\delta = 2$  to  $18 \text{ m s}^{-1}$  in steps of  $2 \text{ m s}^{-1}$  resulting in nine almost equidistant steps for  $u_{\tau, HF}$  on the abscissa in Fig. 3.4. The average deviation is about  $\pm 5\%$  for  $u_{\tau, HF} \geq 0.2 \text{ m s}^{-1}$  in the case of the universal calibration function which is reflected by the high coefficient of determination of  $R^2 = 0.992$  (our fit, Fig. 3.3). Only slightly lower deviations of about  $\pm 3\%$  in average were found when applying individual calibration functions to each of the four Irwin sensors with different tube heights  $h$ . Here, the coefficient of determination merely improved to  $R^2 = 0.995$  on average. The deviations increase towards lower skin friction velocities ( $u_{\tau, HF} < 0.2 \text{ m s}^{-1}$ ) for both the universal and the individual calibration functions. This results primarily from the decreasing accuracies of the Irwin sensors and the pressure scanner at low pressure differences  $\Delta p$ . Furthermore, the calibration suggested by Irwin (1981) (Eq. (3.2)) is applied to a large range of  $\Delta p$  resulting in stronger relative deviations of the calibration data to the fitted curve at lower  $\Delta p$  or  $u_\tau$  values respectively (note the logarithmic representation of the data in Fig. 3.3).

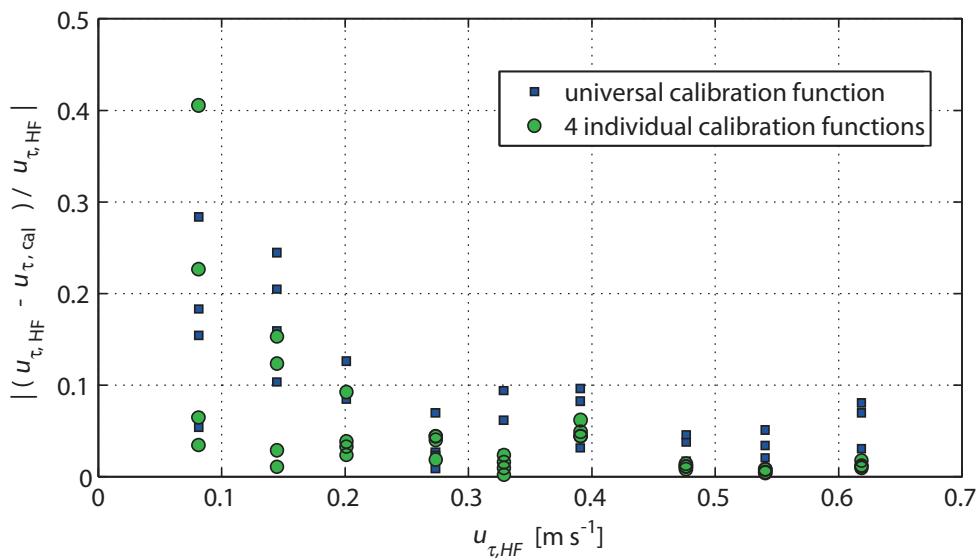


Fig. 3.4: Irwin sensor calibration accuracy for a universal calibration function compared to four individual calibration functions for each sensor.

This calibration accuracy test demonstrates that slightly lower accuracies resulting from the use of a universal calibration function are probably inconsequential relative to the errors that would be introduced if individual calibrations could be performed. However, the final acceptability of the universal calibration to individual calibrations will depend on the application. In cases where considerable change in surface shear-stress is expected and multiple Irwin sensors are needed to obtain high spatial resolutions, the universal calibration may be preferred. If the skin friction velocity variations are more subtle, an individual calibration may be required.

## 3.4 Results and discussion

### 3.4.1 Measurement accuracy

In this section, the accuracy of the measurement setup (the measurement technique together with the experimental setup in the wind tunnel) is discussed including the most important sources of error. We show that reliable skin friction velocity measurements can be performed despite the fact that a universal calibration function is used for all sensors. The main sources of errors in the measurement setup are listed below:

- i) Flush-mounting of the sensors: A raised or recessed sensor, compared to the ideal flush mounting, has a strong influence on the measured pressure difference  $\Delta p$  and thus on  $u_\tau$ . Fig. 3.5 shows the deviations of  $u_\tau$  for an Irwin sensor that is one millimetre below or protruding out of the surface relative to a flush mounted Irwin sensor for a range of different free stream velocities ( $U_\delta = 2 - 20 \text{ m s}^{-1}$ ). As a result, about 10-20% decreased or increased skin friction velocities were measured relative to a flush mounted sensor.

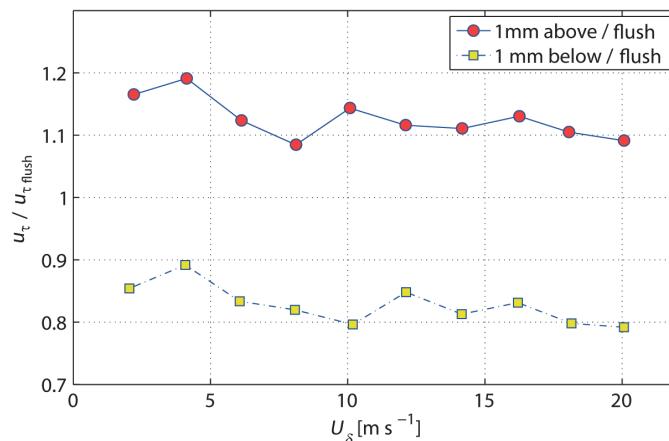


Fig. 3.5: Deviation of skin friction velocities measured with a not perfectly flush mounted Irwin sensor (1 mm above and 1 mm below the surface) relative to a flush mounted sensor.

- ii) Sensor position in the wind tunnel: wind tunnels are not able to produce a perfectly homogeneous boundary-layer. Inhomogeneities in the air flow are introduced by the side walls, the fan, or an imperfectly adjusted wind tunnel ceiling. In our wind tunnel,

the near surface mean velocities  $U(z = 30 \text{ mm})$  in the middle of the wind tunnel are about 8% lower than 250 mm towards the side walls. This propagates to about 10% lower skin friction velocities in the centre of the wind tunnel relative to locations closer to the side walls. This effect is shown in Fig. 3.6a, which shows the spatial variability of the skin friction velocity on a smooth wooden wind tunnel floor measured with 40 Irwin sensors mounted in a triangular array. More details about these measurements can be found at the end of this section.

iii) Pressure scanner inaccuracies: The pressure differences at the Irwin sensors are relatively low, ranging from  $\Delta p \approx 0$  to 60 Pa depending on the tube length  $h$  and the wind velocity. Modern capacitive pressure transducers have a very good accuracy but are quite expensive and limited to low sampling frequencies. Piezoresistive pressure transducers, in contrast, are relatively cheap and allow for sampling frequencies up to  $f = 1 \text{ kHz}$  and more. Our multi-channel pressure scanner uses piezoresistive transducers and has a maximum error of  $\pm 0.5 \text{ Pa}$ . The typical error is  $\pm 0.2 \text{ Pa}$ , which leads to uncertainties in the friction velocity of  $\Delta u_\tau \approx \pm 0.01 \text{ m s}^{-1}$  for  $\Delta u_\tau < 0.13 \text{ m s}^{-1}$  and to  $\Delta u_\tau \approx \pm 0.001 \text{ m s}^{-1}$  for  $\Delta u_\tau > 0.4 \text{ m s}^{-1}$ .

iv) Irwin sensor geometry variations: Slight geometric variations such as an imperfectly concentric tube or small burrs seem to have a very minor influence on sensor performance relative to the other points discussed above. However, the tube length  $h$  is used in the calibration function and thus needs to be measured carefully for each sensor used for the experiments. Measuring the sensor tube length  $h$  with an accuracy of  $\Delta h = \pm 0.1 \text{ mm}$  results in a skin friction velocity variation of maximum  $\Delta u_\tau \approx 0.002 \text{ m s}^{-1}$  at high skin friction velocities ( $u_\tau > 0.5 \text{ m s}^{-1}$ ) which decreases strongly for lower skin friction velocities.

v) Two-component hot-film anemometry errors: The two-component hot-film anemometer (sampling rate: 20 kHz) was validated against a certified fan anemometer (accuracy:  $\pm 0.1 \text{ m s}^{-1}$ ) prior to each experiment. For the calibration, the voltages at the hot-film and the wind velocities at the fan anemometer were simultaneously measured in the free stream ( $U_\delta = 2\text{-}18 \text{ m s}^{-1}$ ). The calibration function typically fits the data with  $R^2 > 0.99$ . The calibration and the hot-film measurement system itself introduced inaccuracies that are not further quantified in this work but have an influence on the Irwin sensor calibration and are partly responsible for the errors shown in Fig. 3.4. However, the excellent agreement of our calibration function with Irwin's original function (Eq. (3.2) and (3.3), Fig. 3.3) confirms the high accuracy of both Irwin's and our calibration.

To provide an estimate of the influence of the above mentioned errors on measured skin friction velocities, 40 Irwin sensors with  $h = 5 \text{ mm}$  were positioned in a triangular array on the smooth wooden wind tunnel floor and  $u_\tau(x,y)$  measured for a free stream velocity of  $U_\delta = 16 \text{ m s}^{-1}$  (Fig. 3.6a). Here,  $y$  is the direction transverse to the flow. The wind direction was from left to right and the positions of the Irwin sensors are marked as black dots. The measurement

data was interpolated onto a regular grid using a simple linear interpolation. A perfect measurement setup would result in a uniform  $u_\tau$  - distribution. However, variations in the experiment setup (points i and ii) and inaccuracies of the measurement technique (points iii and iv) result in a distribution that shows small deviations of up to  $\pm 5\%$  from the spatially averaged mean value  $\langle u_\tau \rangle = 0.5 \text{ m s}^{-1}$ . The inhomogeneous flow in the wind tunnel is reflected by slightly larger  $u_\tau$  values at  $y = \pm 200 - 300 \text{ mm}$  relative to the centre of the wind tunnel at  $y = 0$  as mentioned before. However, this trend is rather weakly represented and suppressed by other measurement inaccuracies (errors i, iii and iv) that are randomly superimposed on the skin friction velocity distribution in Fig. 3.6a.

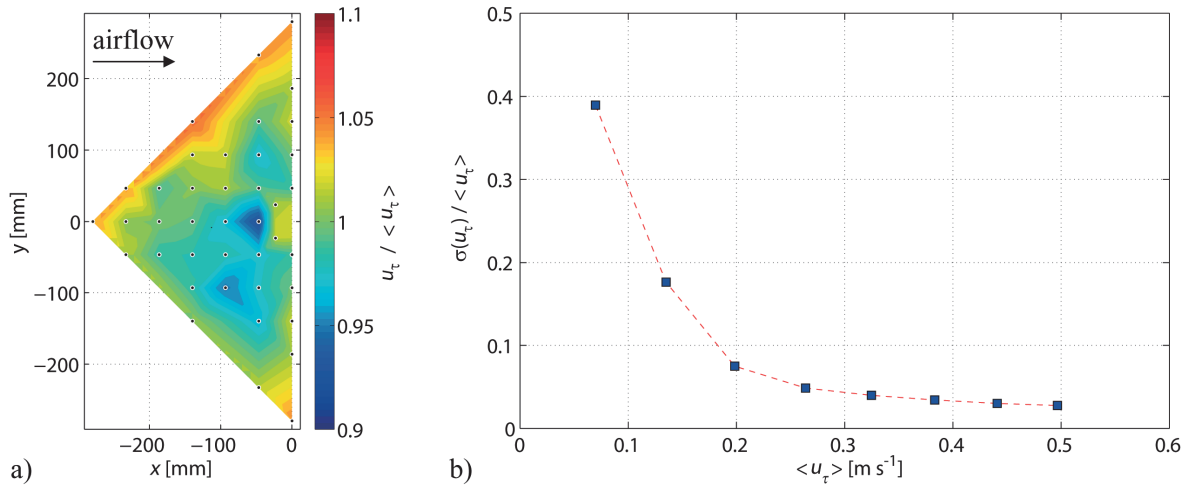


Fig. 3.6: a) Normalized, temporally averaged skin friction velocity distribution  $u_\tau(x,y)$  (spatial average  $\langle u_\tau \rangle = 0.5 \text{ m s}^{-1}$ ) for a smooth wooden wind tunnel floor with slight variations resulting from measurement errors i to iv ( $U_\delta = 16 \text{ m s}^{-1}$ ). b) Variations of skin friction velocity  $\sigma(u_\tau)/\langle u_\tau \rangle$  for 32 Irwin sensors simultaneously measured on a smooth wooden floor at different free stream velocities ( $U_\delta = 2 - 16 \text{ m s}^{-1}$ ).

Similar measurements have been performed at additional free stream velocities ( $U_\delta = 2 - 14 \text{ m s}^{-1}$ ) to assess the influence of the measurement inaccuracies over the whole skin friction velocity range. The spatial variations average to  $\sigma(u_\tau)/\langle u_\tau \rangle \approx 0.05$  for intermediate to high skin friction velocities ( $0.13 \text{ m s}^{-1} < u_\tau < 0.5 \text{ m s}^{-1}$ ) and increase to  $\sigma(u_\tau)/\langle u_\tau \rangle > 0.2$  for  $u_\tau < 0.13 \text{ m s}^{-1}$  (Fig. 3.6b). The large variations  $\sigma(u_\tau)/\langle u_\tau \rangle$  at low skin friction velocities result from the limited accuracy of the pressure scanner at low pressure differences  $\Delta p$  and the Irwin sensors at low wind velocities (Irwin, 1981). Fig. 3.6b reveals the limitations of skin friction velocity measurements using multiple Irwin sensors together with a universal calibration function. The eight chosen free stream velocities with increments of  $2 \text{ m s}^{-1}$  result in eight equidistant skin friction velocity steps on the abscissa. In Fig. 3.6, the error includes only skin friction velocity variations resulting from the errors i to iv. The accuracy of our mean  $u_\tau$  values and the calibration are substantiated by their remarkable agreement with Irwin's original calibration function (Eq. (3.2) and (3.3), Fig. 3.3) and the subsequent validation of the measurement setup. This excellent agreement with Irwin's original calibration function further suggests that acceptable measurements with similar accuracies to those discussed in this section can be performed even if Irwin's original function (Eq. (3.2)) is used without



performing a sensor calibration at all. However, this assumes the application of pressure transducers with accuracies similar to those of the pressure scanner used in this study.

### 3.4.2 Validation of the measurement setup

The measurement setup is validated by investigating the relationship between the skin friction velocity  $u_\tau$  measured with the Irwin sensors and the free stream velocity  $U_\delta$  measured with a fan anemometer for a smooth wooden wind tunnel floor. Fig. 3.7 is based on the same data used in Fig. 3.6 and shows the average skin friction velocity  $\langle u_\tau \rangle$  of all 32 Irwin sensors against  $U_\delta$ . An excellent linear relationship ( $R^2 = 0.9995$ ) was found between  $\langle u_\tau \rangle$  and  $U_\delta$  with a slope of 0.031 which is a first indicator for the high accuracy of our skin friction velocity measurements. Additionally, kinematic Reynolds stress profiles  $-\overline{u'w'}(z)$  at free stream velocities  $U_\delta = 8, 12$  and  $16 \text{ m s}^{-1}$  were measured using the two-component hot-film anemometer. The friction velocities  $u_*$  in the constant stress layer of these profiles are included as well. Very good agreement exists between the hot-film data and the Irwin sensor measurements. Fig. 3.7 proves that the Irwin sensor measurement technique works well and produces consistent and reliable skin friction velocity data.

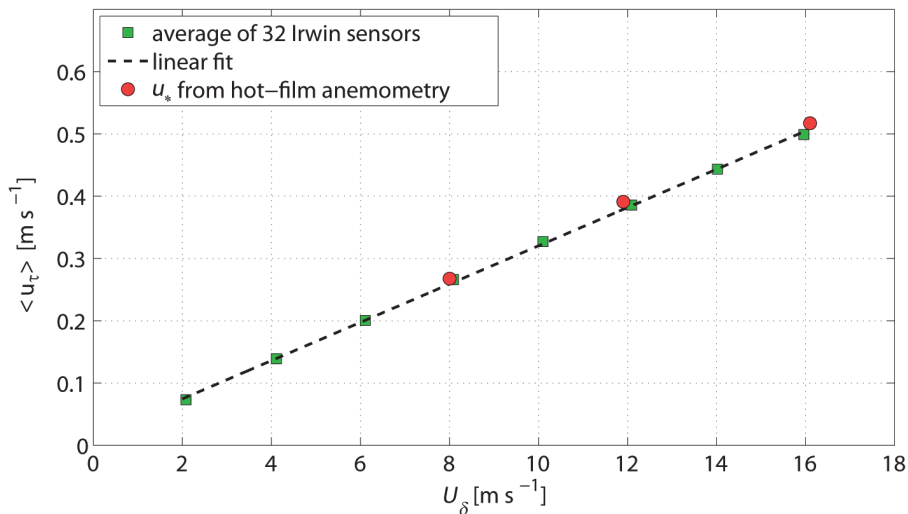


Fig. 3.7: Average skin friction velocity  $\langle u_\tau \rangle$  for the smooth wooden wind tunnel floor measured with Irwin sensors and friction velocity  $u_*$  measured with two-component hot-film anemometry against the free stream velocity  $U_\delta$ .

## 3.5 Wall-mounted block measurements

In this section, the skin friction velocity distribution  $u_\tau(x,y)$  around a single, wall-mounted rectangular block (length  $\times$  width  $\times$  height =  $60 \times 60 \times 100 \text{ mm}$ ) is presented and briefly discussed as a demonstration of the application and reliability of Irwin sensor skin friction velocity measurements (Fig. 3.8a). For the measurements, a row of 23 Irwin sensors with tube length  $h = 5 \text{ mm}$  was mounted flush with the ground transverse to the mean flow at the downwind end of the test section (Fig. 3.1b). The block was moved piecewise in the direction of the flow to measure the 2D skin friction velocity distribution  $u_\tau(x,y)$ . This resulted in a total of 773 measurement locations on an area of  $506 \text{ mm} \times 1200 \text{ mm}$ . The approaching flow is

characterized by the same profiles as shown in Fig. 3.2 (with S&R). The free stream velocity was  $U_\delta = 15.75 \text{ m s}^{-1}$  and the average skin friction velocity in the undisturbed flow was  $u_{\tau,avg} = 0.49 \text{ m s}^{-1}$  during the measurement. This corresponds to a Reynolds number  $Re_h = U_h h_b / \nu = 80000$  where  $U_h = 12.1 \text{ m s}^{-1}$  is the mean wind velocity at the block height  $h_b = 0.1 \text{ m}$  measured with the hot-film anemometer. The spatial resolution of the measurement varies from  $22 \text{ mm} \times 25 \text{ mm}$  close to the block to  $22 \text{ mm} \times 100 \text{ mm}$  further away. Each skin friction velocity  $u_\tau$  is a temporal average of 30 seconds which is sufficiently long to obtain a stable mean.

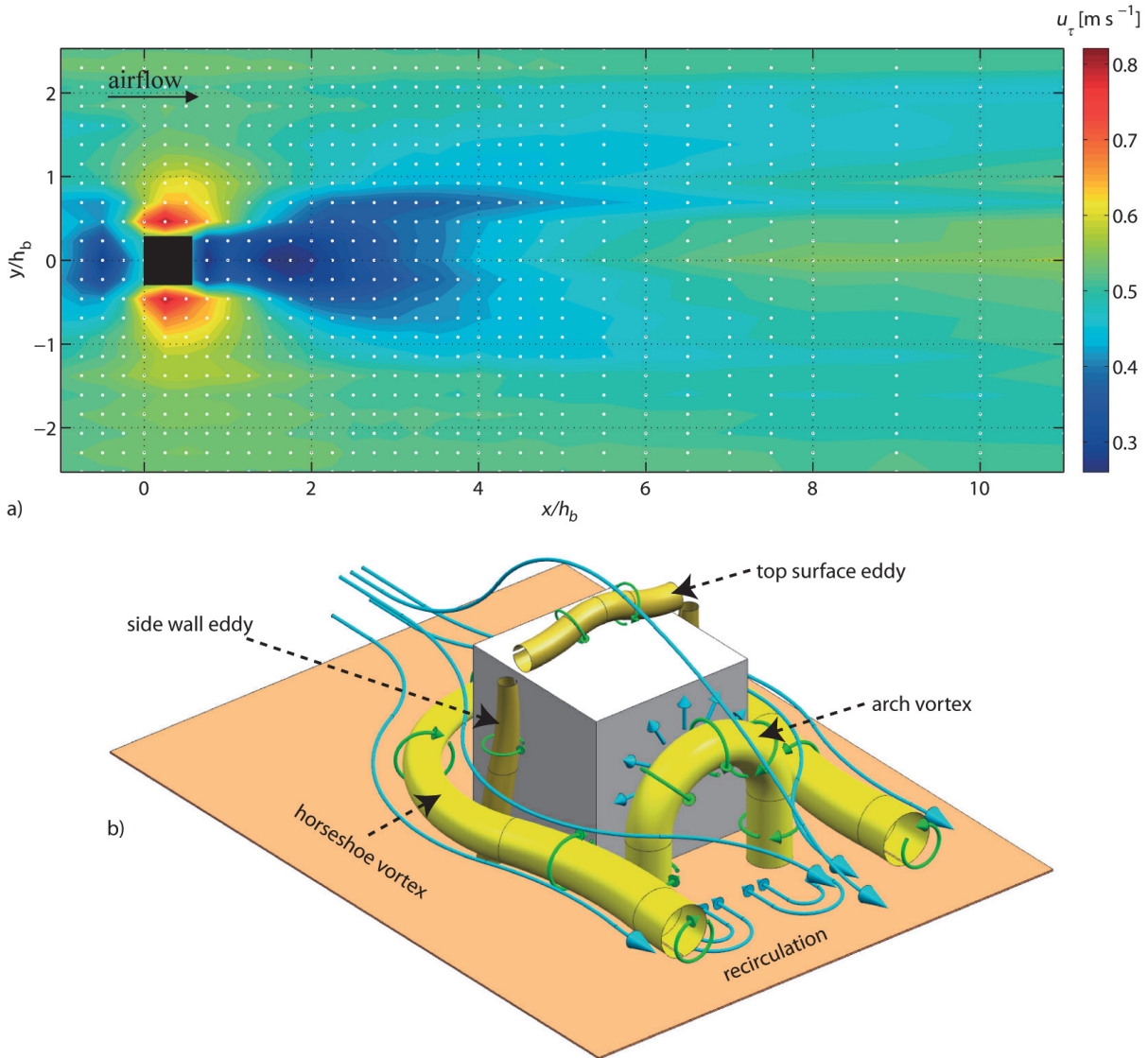


Fig. 3.8: a) Temporally averaged skin friction velocity distribution  $u_\tau(x,y)$  around a single wall-mounted rectangular block (length  $\times$  width  $\times$  height =  $60 \times 60 \times 100 \text{ mm}$ ;  $U_\delta = 15.75 \text{ m s}^{-1}$ ). b) Schematic representation of vortex structures developing around a single wall-mounted cube (based on Martinuzzi and Tropea, 1993).

A simple linear interpolation was used for the contour plot in Fig. 3.8a to depict the data as cleanly as possible, avoiding artefacts resulting from more sophisticated interpolation algorithms. The location of the block is a singularity and the skin friction velocity in the near vicinity of the block varies strongly from very low to very high  $u_\tau$  - values. To resolve these variations, a higher spatial measurement resolution would be required than is possible to



obtain using Irwin sensors. A sensitivity study showed that using any assumption for the value of  $u_\tau$  at the location of the roughness element (e.g.  $u_\tau = 0$  or  $u_\tau = u_{\tau,avg}$ ) for the interpolation resulted in similarly non-physical representations of the skin friction velocity close to the element. Therefore, for the purpose of data visualization,  $u_\tau$  was set equal to  $u_{\tau,avg}$  at the location of the block and the friction velocity was interpolated across that location. The values in that location were then discarded. The streamwise left ( $y > 0$ ) and right ( $y < 0$ ) halves of the skin friction velocity distribution are very similar showing an excellent streamwise symmetry with a maximum difference between the 2 sides of  $u_\tau = 0.05 \text{ m s}^{-1}$  and typically less than  $u_\tau = 0.017 \text{ m s}^{-1}$  (one standard deviation). This provides a further demonstration of the high quality, repeatability, and accuracy of these Irwin sensor measurements (Fig. 3.8a).

To provide a connection between our measured surface skin friction velocity distribution (Fig. 3.8a) and classic fluid dynamics theory, the flow structures developing around a single wall-mounted cube are briefly discussed: Fig. 3.8b (based on Martinuzzi and Tropea, 1993) shows a schematic representation of the vortices shed by a cube. Well-defined flow separation is found at the cube's front corners, resulting in smaller eddies developing close to the top surface and the side-walls of the cube. A large horseshoe vortex wraps around the upstream faces of the cube. Directly downwind of the cube, an arch vortex develops with a reverse flow direction close to the ground. At the downwind end of this recirculation region, flow stagnation occurs and the outer flow reattaches to the ground.

The skin friction velocity distribution  $u_\tau(x,y)$  for the block (Fig. 3.8a) is qualitatively in very good agreement with the surface shear-stress distribution measurements  $\tau_s(x,y)$  around a single cylinder presented by Sutton and McKenna-Neumann (2008). Those authors also used Irwin sensors for their measurements. Flow stagnation due to an adverse pressure gradient upwind of the block and the cylinder results in lower skin friction velocities. Flow separation and reattachment downwind of the block and the cylinder results in a sheltered area with the lowest measured  $u_\tau$ -values. Downwind of the sheltered area of the block, in a region where the trailing vortices reattach to the surface, a local maximum occurs with  $u_\tau \approx 0.55 \text{ m s}^{-1}$  (at  $x/h_b \approx 6 - 8$ ). Sutton and McKenna-Neumann (2008) found a local maximum at a similar location. The highest skin friction velocities of  $u_\tau = 0.82 \text{ m s}^{-1}$  were found in the speed-up zones at both sides of the block, resulting from locally high wind velocities due to flow convergence. The sheltered area, beginning at the downwind edge of the block, extends to  $3 \times h_b$  in the streamwise direction which is in good agreement with the dimensions of the sheltered area found by Sutton and McKenna-Neumann (2008) for the cylinder. Lakehal and Rodi (1997) modelled the flow around a surface mounted cube using various turbulence models, compared their results with the measurements of Martinuzzi and Tropea (1993) and found that all models over-predict the size of the sheltered area downstream of the cube. Spatially resolved skin friction velocity distributions like those presented in the previous paragraph thus also provide useful validation data for numerical models. Metadata describing measurements of the  $u_\tau$ -distribution around the single wall-mounted block (Fig. 3.8a) can be found on the internet platform [www.swiss-experiment.ch](http://www.swiss-experiment.ch) (Walter, 2011) and processed or raw data can be made available on request.

### 3.6 Summary and conclusions

This study introduced an experimental setup for measuring spatially resolved skin friction velocity distributions around wall-mounted obstacles using Irwin sensors. First, a sensor calibration procedure to determine a universal calibration function that can be applied to multiple sensors without significant reduction in accuracy was demonstrated. The universal calibration function allows significant savings in experimental time when using multiple sensors for the measurements. The coefficients of the universal calibration function are in excellent agreement with those originally determined by Irwin (1981), supporting the validity of both calibrations. This finding suggests that using Irwin's original calibration function without performing any calibration of identically-build sensors in general results in measurement accuracies similar to those found in this study.

Accuracy tests verified that reliable skin friction velocity distributions can be measured with the universal calibration function. The overall measurement accuracy averages to about  $\pm 5\%$  for  $u_\tau \approx 0.13 - 0.5 \text{ m s}^{-1}$  (Fig. 3.5). The reliability of the skin friction velocity measurements was validated by: i) the strong linear relationship between  $u_\tau$  and  $U_\delta$  (Fig. 3.7), ii) the good agreement of independent  $u_\tau$ - and  $u_*$ - measurements using Irwin sensors and the two-component hot-film anemometer (Fig. 3.7) and iii) the excellent streamwise symmetry of the skin friction velocity distribution around a single wall-mounted block (Fig. 3.8). Good qualitative agreement was found between the surface shear-stress measurements around a single cylinder presented by Sutton and McKenna-Neumann (2008) and our block measurements.

Overall, Irwin sensors were found to be well suited for measuring skin friction velocity distributions with high spatial resolution, and should thus be considered as an excellent resource for application in environmental fluid mechanics studies as well as their historic use in wind comfort issues. Skin friction velocity measurements like presented in this study may also provide validation data for CFD- (Computational Fluid Dynamics) models.

### Acknowledgements

We would like to thank the Vontobel foundation and the Swiss National Science Foundation (SNF) for financial support. The SLF workshop and GS Technology assisted in the development and the production of the measurement technique and the experiment setup. Hans Herranhof created the technical drawings presented in this manuscript. Katrin Burri and Benjamin Eggert helped with the wind tunnel experiments and participated in many fruitful discussions.

# 4 Spatio-temporal surface shear-stress variability in live plant canopies and cube arrays

Walter B, Gromke C, Leonard K, Manes C, Lehning M (2012b) Spatio-temporal surface shear-stress variability in live plant canopies and cube arrays. *Boundary-Layer Meteorology*, doi:10.1007/s10546-011-9690-5

## 4.1 Introduction and background

Soil erosion, drifting snow, and the entrainment and transport of pollen, seeds and particulate matter are examples of processes governed by airflow over an erodible surface (Bagnold 1943). These processes are directly related to land degradation, desertification, air quality, local water storage in the form of snow, and to reduced biodiversity with strong implications for ecosystems and human societies (Shao 2008). Plants influence these processes by reducing the area of ground exposed to the wind, by trapping particles in motion, by local stress concentration and by absorbing momentum from the flow, resulting in lower surface shear-stress  $\tau_s$  on the ground beneath the plant canopy (e.g. Wolfe and Nickling 1993).

The distribution of surface shear-stress  $\tau_s$  is the key to quantifying the sheltering effect of non-erodible roughness elements because its magnitude and spatiotemporal variations determine the onset and degree of differential erosion. The initiation of particle erosion is governed by the fluid threshold friction velocity  $u_{*t}$ , i.e. particle movement on a surface begins when the friction velocity  $u_* > u_{*t}$ . The threshold value  $u_{*t}$  for a given sediment is defined as the friction velocity  $u_* = (-\overline{u'w'})^{1/2} = (\tau/\rho)^{1/2}$  in the constant-stress layer at the commencement of particle entrainment. Here,  $u'$  and  $w'$  are the fluctuations in the mean streamwise and vertical velocity components,  $\tau$  is the total stress on the whole surface and  $\rho$  the air density. This threshold value  $u_{*t}$  is an important parameter because most mass transport models use  $Q \propto (u_* - u_{*t})^3$  to predict the mass transport rate  $Q$  (e.g. Anderson and Sorensen 1991).

Numerous investigations of the sheltering effect of plants have been conducted but all of them are constrained by one or more of the following three limitations:

- (i) Use of artificial rigid roughness elements (Marshall 1971; Wooding et al. 1973; Gillette and Stockton 1989; Musick et al. 1996; Crawley and Nickling 2003; Brown et al. 2008). Solid rigid cylinders or cubes poorly simulate the aerodynamical shape of

live plants. Live plants have highly irregular structures that can be extremely flexible and porous resulting in considerable changes to the drag and flow regimes relative to rigid imitations (Gillies et al. 2002). Crawley and Nickling (2003) conducted drag partition measurements to determine model parameters for the Raupach (1992) drag partition model and found that the surface shear-stress inhomogeneity parameter  $m$  should be revised. Brown et al. (2008) found no significant effect of different spatial arrangements of non-erodible roughness elements on the drag partition.

(ii) Field experiments with no control over the wind conditions (Musick and Gillette 1990; Wolfe and Nickling 1996; Wyatt and Nickling 1997; Lancaster and Baas 1998; King et al. 2006; Gillies et al. 2007). In field experiments it is difficult to decouple the influences of the plants on surface shear-stress from those induced by the variations in the wind. Wyatt and Nickling (1997) performed shear-stress measurements in sparse desert creosote communities and found greater roughness element drag coefficients for porous shrubs than for solid elements. Gillies et al. (2007) found that the Raupach (1992) drag partition model performed very well for regular arrays of solid elements of different roughness densities within a large open area.

(iii) Spatial and temporal averages: only limited data are available on local peak shear-stress values (Crawley and Nickling 2003; King et al. 2006; Brown et al. 2008) or temporal variations of surface shear-stress (Sutton and McKenna-Neumann 2008). Sutton and McKenna-Neumann (2008) examined bed level flow patterns around solid cylinders for varying roughness densities and correlated vortices shed by the obstacles with their erosive capability.

Several wind-tunnel studies have measured the mean surface shear-stress on the underlying surface using drag balances to investigate the sheltering effect of non-erodible roughness elements (e.g. Crawley and Nickling 2003). However, Raupach et al. (1993) stated that the peak surface shear-stress  $\tau_s''$  rather than the average surface shear-stress on the exposed surface area  $\tau_s'$  is responsible for the initiation of particle erosion and developed a model that predicts the peak as well as the average surface shear-stress partition:

$$\left(\frac{\tau_s''}{\tau}\right)^{\frac{1}{2}} = \left[\frac{1}{(1-m\sigma\lambda)(1+m\beta\lambda)}\right]^{\frac{1}{2}} \quad (4.1)$$

Here,  $\lambda = A_f/S$  is the roughness density where  $A_f$  is the roughness element frontal area,  $S$  is the ground area per roughness element,  $\sigma$  is the ratio of roughness element basal to frontal area and  $\beta$  is defined as the ratio of the roughness element to surface drag coefficient. The parameter  $m$  is defined as  $\tau_s'' = \tau_s'(m\lambda)$ , which means that the peak surface shear-stress is equal to the surface average shear-stress at a lower roughness density ( $m < 1$ ). To predict the average surface shear-stress partition  $(\tau_s'/\tau)^{1/2}$ , we set  $m = 1$ .

Some wind-tunnel and field investigations have used Irwin sensors (Irwin 1981; Wu and Stathopoulos 1993) to obtain point measurements of surface shear-stress at positions where the largest shear-stress values were expected (Crawley and Nickling 2003; King et al.

2006; Brown et al. 2008). These measurements support the Raupach et al. (1993) model (Eq. (4.1)) very well. To fully quantify the sheltering effect of different roughness elements against erosion, however, the spatial and temporal distribution of surface shear-stress  $\tau_s(t, x, y)$  on the ground are needed. Sutton and McKenna-Neumann (2008) first measured temporally-resolved surface shear-stress distributions on the surface beneath wooden cylinder arrays using Irwin sensors. Unfortunately it was not possible for them to sample very large arrays that filled the entire floor of the wind-tunnel, preventing the generation of a well-developed boundary-layer.

Most of the shear-stress ratio measurements referenced above are generally in good agreement with each other. However, variations between them exist, of order  $\Delta(\tau_s'/\tau)^{1/2} \approx \Delta(\tau_s''/\tau)^{1/2} \approx \pm 0.1$ . These variations result from different experimental set-ups, types of roughness elements used, and the distribution of the roughness elements over the surface. This makes it difficult for practitioners and modellers to select realistic surface shear-stress values for vegetation canopies over a range of planting densities. It also remains unknown how well rigid and non-porous roughness elements represent the sheltering effect of live plants, and if conclusions drawn from such experiments can be assumed to hold true for live plant canopies in natural environments.

The goal of our wind-tunnel study was to quantify the sheltering capability of different densities of live plant canopies against wind erosion under controlled conditions. The results are compared to similar experiments performed using wooden cube arrays of the same densities because previous wind-tunnel studies quantifying the sheltering effect of plants have mainly used rigid and non-porous plant imitations such as cubes and cylinders for their experiments. Although our live plant arrays are not natural vegetation canopies, the fact that our plants are of similar size, trimmed to a standard height and arranged with regular spacing allows us to systematically investigate the influence of plant flexibility and porosity on the sheltering effect. In addition, the live plant canopies used here are far closer to natural plant canopies than any roughness array used in previous wind-tunnel investigations of shear-stress partitioning. While the use of live plants in wind-tunnel studies is not novel (e.g. Kim et al. 2000 and Burri et al. 2011a, 2011b), this is the first study to investigate the surface shear-stress distribution in live plant canopies of different densities.

## 4.2 Methods

We performed wind-tunnel measurements of spatially- and temporally-resolved surface shear-stress distributions  $\tau_s(t, x, y)$  on the ground beneath live plant canopies using Irwin sensors (Irwin, 1981) (Fig. 4.1a). For comparison, similar measurements were made substituting rigid cubes at the same locations as the plants (Fig. 4.1b). Cubes were chosen because of their simple geometry with well-defined flow separation at the edges and because the shear-stress distributions in the cube arrays provide a data base for CFD (Computational Fluid Dynamics) model validation. Four different canopy densities (0, 5.25, 24.5, 55 roughness elements per  $\text{m}^2$ , hereafter named as the smooth floor, low, medium and high density cases) were investigated at free-stream velocities ranging from  $U_\delta = 8 - 16 \text{ m s}^{-1}$ . The corresponding roughness densities  $\lambda$  are given in Table 4.1. Because they streamline with the airflow, the plants frontal area  $A_f$  and thus the roughness density  $\lambda$  decrease at higher wind speeds (Fig. 4.1c). To determine  $\lambda$ , photographs of the plants' upstream vertical faces were taken at the



different wind speeds inside the wind-tunnel to determine  $A_f$  by digital image processing (Fig. 4.1d). For an overview of the experiments and a summary of the measurement results see Table 4.1.

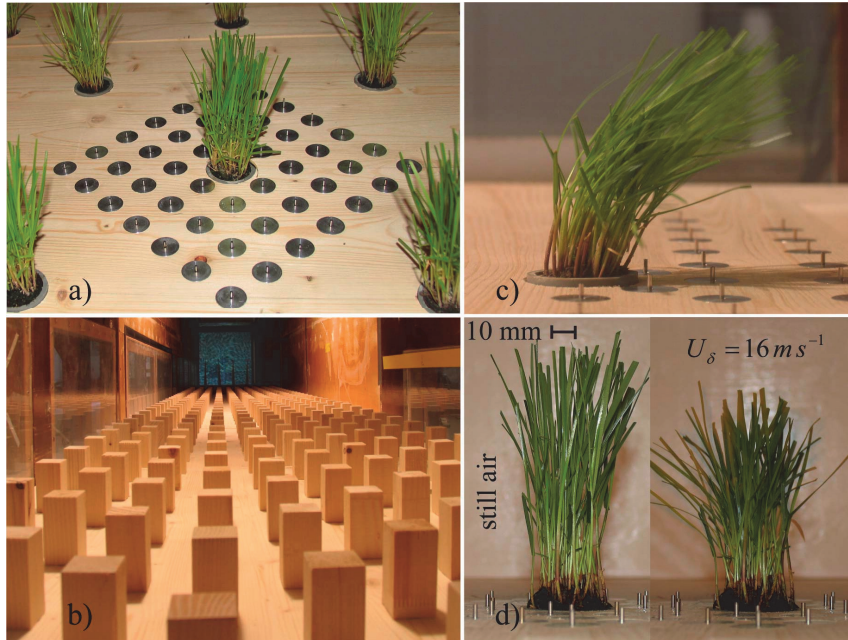


Fig. 4.1: (a) Flush mounted Irwin sensors in a live plant canopy (medium density case,  $\lambda = 0.08$ ). (b) 8 meter test section covered with cubes (high density case,  $\lambda = 0.176$ ). (c) Plant (*lolium perenne*) streamlining with the flow (low density case,  $\lambda = 0.015$ ,  $U_\delta = 16 \text{ m s}^{-1}$ ). (d) Front view pictures (streamwise direction) of a plant in still air and for  $U_\delta = 16 \text{ m s}^{-1}$  (high density case,  $\lambda = 0.178$ ).

The SLF (WSL Institute for Snow and Avalanche Research, Davos, Switzerland) boundary-layer wind-tunnel is 18 m long in total, has an 8 m long test section, a 6 m long fetch upwind of the test section, a cross-sectional area of  $1 \text{ m} \times 1 \text{ m}$  and operates in suction mode. It has successfully been used for investigating snow-wind interaction (e.g. Clifton and Lehning, 2008 and Gromke et al. 2011) and more recently to investigate soil erosion in live plant canopies (e.g. Burri et al. 2011a and 2011b). An adjustable ceiling allows for the development of a natural boundary-layer over various surfaces. The experimental set-up consists of wooden boards in which live plants (*lolium perenne*) grown in plastic tubes were arranged in staggered rows (Fig. 4.1a).

All measurements were performed at the downwind end of the test section. Spires and additional artificial roughness elements were positioned on the fetch upwind of the test section for preconditioning of the boundary-layer flow, as in Burri (2011c). Burri (2011c) performed a similar study at the SLF wind-tunnel investigating sediment mass flux profiles in live plant canopies of the same densities as investigated in this study. The flow conditioning guarantees the comparability of our shear-stress measurements with results found by Burri (2011b, 2011c). With or without flow conditioning on the upwind fetch, the total stress  $\tau$  above the medium density canopy case was very similar at the measurement location (Walter et al. 2009).

Table 4.1: Experiment summary: (a) Number of roughness elements per square meter, (b) Roughness density  $\lambda$ , (c) Free-stream velocity  $U_\delta$  at  $z = 0.5$  m, (d) Friction velocity  $u_*$ , (e) Average surface shear-stress  $\tau_s'$  on exposed surface area, (f) Standard deviation of the spatial variations of  $\tau_s(x,y)$ , (g) Minimum and (h) peak surface shear-stress.

| MEASUREMENT SET-UP: |                   | HOTFILM DATA: |                                    | IRWIN SENSOR DATA:            |                                   |  |  |                                    |
|---------------------|-------------------|---------------|------------------------------------|-------------------------------|-----------------------------------|--|--|------------------------------------|
|                     | (a)               | (b)           | (c)                                | (d)                           | (e)                               | (f)                                      | (g)                                    | (h)                                |
|                     | # m <sup>-2</sup> | $\lambda$     | $U_\delta$<br>[m s <sup>-1</sup> ] | $u_*$<br>[m s <sup>-1</sup> ] | $\tau_s'$<br>[N m <sup>-2</sup> ] | $\sigma(\tau_s)$<br>[N m <sup>-2</sup> ] | $\tau_{s,min}$<br>[N m <sup>-2</sup> ] | $\tau_s''$<br>[N m <sup>-2</sup> ] |
| Smooth:             | 0                 | 0             | 8.0                                | 0.27                          | 0.072                             | 0.005                                    | 0.052                                  | 0.080                              |
|                     | 0                 | 0             | 11.7                               | 0.39                          | 0.150                             | 0.007                                    | 0.122                                  | 0.165                              |
|                     | 0                 | 0             | 16.3                               | 0.57                          | 0.252                             | 0.010                                    | 0.215                                  | 0.277                              |
| Plants:             | 5.25              | 0.0175        | 8.3                                | 0.40                          | 0.055                             | 0.009                                    | 0.021                                  | 0.073                              |
|                     | 5.25              | 0.0166        | 12.1                               | 0.56                          | 0.128                             | 0.018                                    | 0.065                                  | 0.158                              |
|                     | 5.25              | 0.0152        | 16.6                               | 0.73                          | 0.227                             | 0.028                                    | 0.127                                  | 0.275                              |
|                     | 24.5              | 0.0881        | 7.7                                | 0.45                          | 0.020                             | 0.003                                    | 0.011                                  | 0.027                              |
|                     | 24.5              | 0.0879        | 11.4                               | 0.64                          | 0.047                             | 0.006                                    | 0.028                                  | 0.062                              |
|                     | 24.5              | 0.0808        | 15.1                               | 0.79                          | 0.091                             | 0.012                                    | 0.052                                  | 0.122                              |
|                     | 55                | 0.200         | 8.3                                | 0.49                          | 0.010                             | 0.002                                    | 0.004                                  | 0.013                              |
|                     | 55                | 0.189         | 12.6                               | 0.70                          | 0.020                             | 0.002                                    | 0.013                                  | 0.024                              |
|                     | 55                | 0.178         | 16.2                               | 0.87                          | 0.037                             | 0.003                                    | 0.027                                  | 0.043                              |
| Cubes:              | 5.25              | 0.0168        | 12.4                               | 0.63                          | 0.097                             | 0.015                                    | 0.027                                  | 0.168                              |
|                     | 24.5              | 0.0784        | 12.4                               | 0.67                          | 0.039                             | 0.010                                    | 0.014                                  | 0.073                              |
|                     | 55                | 0.176         | 12.3                               | 0.65                          | 0.026                             | 0.005                                    | 0.012                                  | 0.037                              |

### 4.2.1 Flow measurements

Two-component hot-film measurements using a Dantec (*Streamline*, sampling frequency  $f = 20$  kHz) measurement device were carried out to determine basic flow characteristics including vertical profiles of the mean streamwise wind velocity  $u$  and the kinematic Reynolds stress  $-\overline{u'w'}$ . These flow characteristics were used to demonstrate that a well developed natural boundary-layer was generated for the different roughness densities and to provide a link between the total stress  $\tau$  above the roughness elements and the surface shear-stress  $\tau_s$  measured using Irwin sensors. Following Schlichting (1936), the total shear-stress  $\tau$  on a rough surface can be split into a component acting on the roughness elements  $\tau_R$  and a component acting on the exposed surface area  $\tau_s$  so that  $\tau = \tau_s + \tau_R$ . Vertical hot-film profiles (each with 29 levels) were measured at three different locations for each cube density and for the smooth floor case to obtain one spatially-averaged vertical profile for each roughness density. One profile was measured in the speed-up zone beside, one directly above and one in the wake area downwind of a roughness element. For the plants, eight vertical profiles were measured for the low, seven for the medium, and five for the high density cases at the same locations as mentioned before and at some additional locations. A summary of the hot-film measurement results is given in Table 4.1.

## 4.2.2 Surface shear-stress sensors

Irwin sensors were mounted flush with the surface in an array surrounding a roughness element (Fig. 4.1a) to determine the spatial and temporal variation of the shear-stress  $\tau_s(t, x, y)$  (Irwin 1981; Wu and Stathopoulos 1993). The pressure difference  $\Delta p$  measured at the Irwin sensor was calibrated against the friction velocity  $u_*$  in the constant-stress layer measured with the two-component hot-film anemometer. For the smooth wind-tunnel floor,  $u_*$  is equal to the skin friction velocity  $u_\tau = (\tau_s/\rho)^{1/2}$ . A universal calibration function  $u_\tau = f(\Delta p)$  was determined for all 32 Irwin sensors used in this study with the calibration showing excellent correlation with Irwin's original calibration (Walter et al. 2011). A custom-made 32-channel pressure scanner (range:  $\pm 100$  Pa; accuracy:  $\pm 0.2$  Pa typically; sampling rate: 200 Hz) was used to measure the pressure difference  $\Delta p$ . Each Irwin sensor was connected by urethane tubing (length: 0.51 m; inner diameter: 1.65 mm) to one transducer of the pressure scanner for the measurements.

To estimate the influence of measurement errors on the surface shear-stress variations, all 32 Irwin sensors with a sensor tube height of  $h_s = 5$  mm were simultaneously operated at free-stream velocities  $U_\delta = 2 - 16$  m s<sup>-1</sup> on the smooth wooden wind-tunnel floor without roughness elements (Fig. 4.2a). The variations averaged  $\sigma(\tau_s)/\tau_s = 0.05$  for intermediate to high surface shear-stress ( $0.017$  N m<sup>-2</sup>  $< \tau_s < 0.25$  N m<sup>-2</sup>) with a strong increase in variability at very low shear-stress ( $\tau_s < 0.017$  N m<sup>-2</sup>). Thus, moderate to high free-stream velocities ( $U_\delta = 8 - 16$  m s<sup>-1</sup>) were chosen for the experiments to obtain measurable surface shear-stress variations even in the highest roughness density cases. More details about the experiment set-up, the Irwin sensor calibration and the measurement accuracies can be found in Walter et al. (2012a).

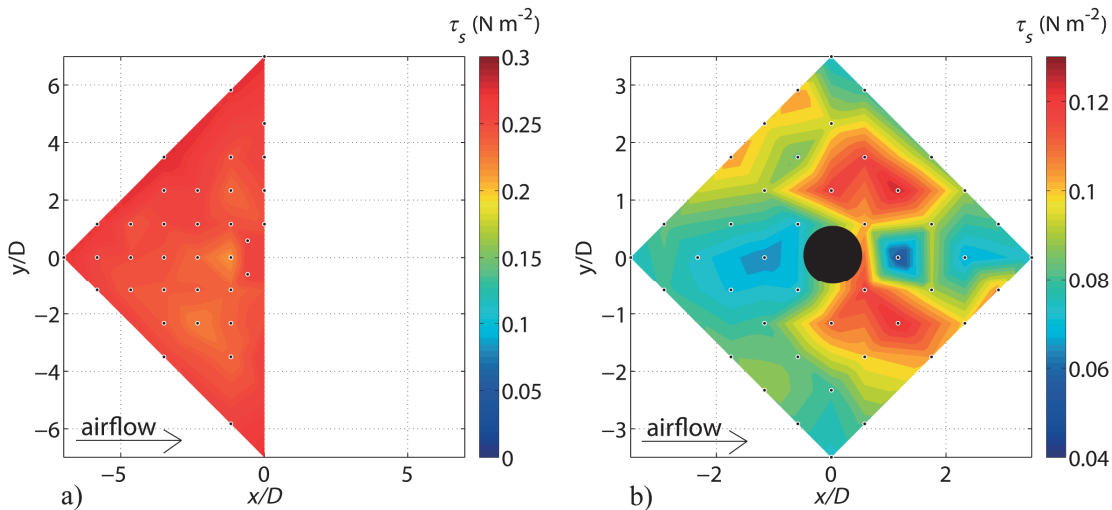


Fig. 4.2: Temporally averaged shear-stress distribution  $\tau_s(x, y)$  for (a) the smooth floor case, where slight variations approximate the measurement uncertainty ( $U_\delta = 16$  m s<sup>-1</sup>,  $\lambda = 0$ ,  $D = 40$  mm) and (b) the medium plant canopy density for a single measured case without averaging for measurement repetitions and for streamwise symmetry ( $U_\delta = 16$  m s<sup>-1</sup>,  $\lambda = 0.088$ ,  $D = 40$  mm).



### 4.2.2.1 Spatial Resolution and Data Processing

The spatial resolution of the Irwin sensor measurements was  $46 \text{ mm} \times 46 \text{ mm}$  for the unplanted and the low density case,  $33 \text{ mm} \times 33 \text{ mm}$  for the medium and  $25 \text{ mm} \times 25 \text{ mm}$  for the high density case (e.g. a). Due to the limited number of 32 pressure transducers available, it was not possible to measure the surface shear-stress at every grid position. Higher measurement densities were chosen close to the roughness elements because the highest spatial variations of the surface shear-stress were observed in these regions in preliminary experiments. The positions of Irwin sensor measurements are marked as black or white dots and the wind direction is from the left to the right in all figures.

The measured shear-stress data were linearly interpolated onto a regular grid that is assumed to represent the pattern around every plant in the canopy at the measurement section. The location of the roughness element is a singularity with a high spatial variability of the surface shear-stress in close proximity to it. A sensitivity study showed no significant difference between the surface shear-stress distributions at the roughness element to surface interface when assuming different conditions at the roughness element location, e.g.  $\tau_S = \tau_{S0}$  (average  $\tau_S$  in the absence of roughness elements) or  $\tau_S = 0$ . Any of these alternatives result in physically questionable representations of  $\tau_S$  at that interface when considering the very high spatial variability of the surface shear-stress in that area together with our measurement resolution. For simplicity, the shear-stress was interpolated across that part of the grid and the values in that location were discarded.

Fig. 4.2b shows the raw temporally-averaged (over 30 sec) shear-stress distribution for a measurement of the medium density plant canopy at  $U_\delta = 16 \text{ m s}^{-1}$ . Variations in the experiment set-up and the measurement technique result in a distribution that shows slight deviations from streamwise symmetry for the left ( $y/D > 0$ ) and the right ( $y/D < 0$ ) halves of the measurement grid. Here,  $D$  is the average plant or cube diameter. In all other presentations of these data, the left and the right half (streamwise sides) were averaged to obtain symmetry and thus a clearer picture of the systematic patterns. Additionally, all figures (except those in Fig. 4.2) are an average of three measurement repetitions, each with different plants in the positions around the Irwin sensors to account for slight variations in plant shape that might affect the shear-stress distribution.

### 4.2.2.2 Temporally-resolved surface shear-stress data

Measuring the surface shear-stress at a frequency of 200 Hz allows for statistical analysis of temporal surface shear-stress variations. Irwin (1981) found a good correlation between velocity time series simultaneously measured with an Irwin sensor and a hot-wire anemometer at the same location (at the Irwin sensor tube height  $h_s$ ). The tube connecting their Irwin sensor to a pressure transducer was 0.61 m long (similar to our set-up). In the spectral domain, the magnitudes of the Irwin sensor velocities agreed within  $\pm 10\%$  with the hot-wire measurements in a range from  $f = 0$  to 80 Hz. The combination of the original Irwin calibration function for wind velocities at the sensor tube height  $U_s = f(\Delta p)$  with that for the skin friction velocity  $u_\tau = f(\Delta p)$  (Irwin, 1981) involves a linear relation  $u_\tau = f(U_s) \approx c_1 U_s + c_2$  where  $c_1$  and  $c_2$  are constants. The magnitudes of our skin friction velocity time series  $u_\tau(t)$  are thus assumed to be correct within the same range of accuracy of  $\pm 10\%$ . The damping of the

signal induced by the tubing resulted in a steadily increasing phase shift of the signals relative to the hot-wire measurements with increasing frequency (Irwin, 1981). Our pressure time series  $\Delta p(t)$  measured at the Irwin sensors, each  $\Delta T = 30$  s long, were digitally lowpass filtered with a cut-off frequency of  $f_c = 80$  Hz. Irwin (1981) defined the standard deviation of the wind speed  $u(t)$  at the height of the Irwin sensor tube as

$$\sigma_u = \sqrt{u'^2} = \frac{\beta_c}{2} \frac{\sqrt{\Delta p'^2}}{\sqrt{\Delta p}} \quad (4.2)$$

where  $\beta_c$  is a calibration constant arising from the calibration of the Irwin sensors against wind speed and  $\Delta p'$  is the pressure fluctuation around the mean value. Note that Irwin sensor measurements contain no information on the direction of the airflow, so the wind speed  $u(t)$  is not the streamwise velocity component in the case of Irwin sensor measurements. Sutton and McKenna-Neumann (2008) defined a measure  $\xi$ , which they referred to as a normalized turbulence intensity, and which gives the relative increase or decrease in the standard deviation  $\sigma_u$  introduced by the roughness elements relative to the smooth floor case:

$$\xi = \frac{\sigma_{u,R}}{\sigma_{u,s}} \quad (4.3)$$

The local skin friction velocity  $u_\tau(t, x, y)$  on the ground beneath the non-erodible roughness elements is not constant with time and may (or may not) exceed a fluid threshold skin friction velocity  $u_{\tau t}$ , above which particle erosion begins for some fraction of time even if the average surface shear-stress velocity  $u_\tau$  is smaller than  $u_{\tau t}$ . The percentage of time  $\Delta t$  while the surface shear-stress velocity  $u_\tau > u_{\tau t}$  can be used to assess the local predominance of erosion and deposition mechanisms:

$$\psi(x, y) = \frac{\Delta t(u_\tau(t, x, y) > u_{\tau t})}{\Delta T} \quad (4.4)$$

Note that the fluid threshold  $u_{\tau t}$  defined here is greater than the average fluid threshold friction velocity  $u_{*t}$  measured in the constant-stress layer at the commencement of particle erosion. The reason for this is that the peak values of  $u_\tau(t, x, y)$ , not the spatiotemporal average, are responsible for the onset of particle erosion. The procedure to estimate  $u_{\tau t}$  is described in Section 3.4.2.

## 4.3 Results and discussion

### 4.3.1 Flow characteristics

Fig. 4.3 shows the vertical profiles of the normalized mean streamwise wind velocity  $u$  and the normalized kinematic Reynolds stress  $u'w'$  for the different roughness configurations at the reference free-stream velocity  $U_\delta = 12$  m s<sup>-1</sup>. Each of the vertical profiles represents a spatial average of at least three and up to eight two-component hot-film profiles measured at different locations above the roughness elements.

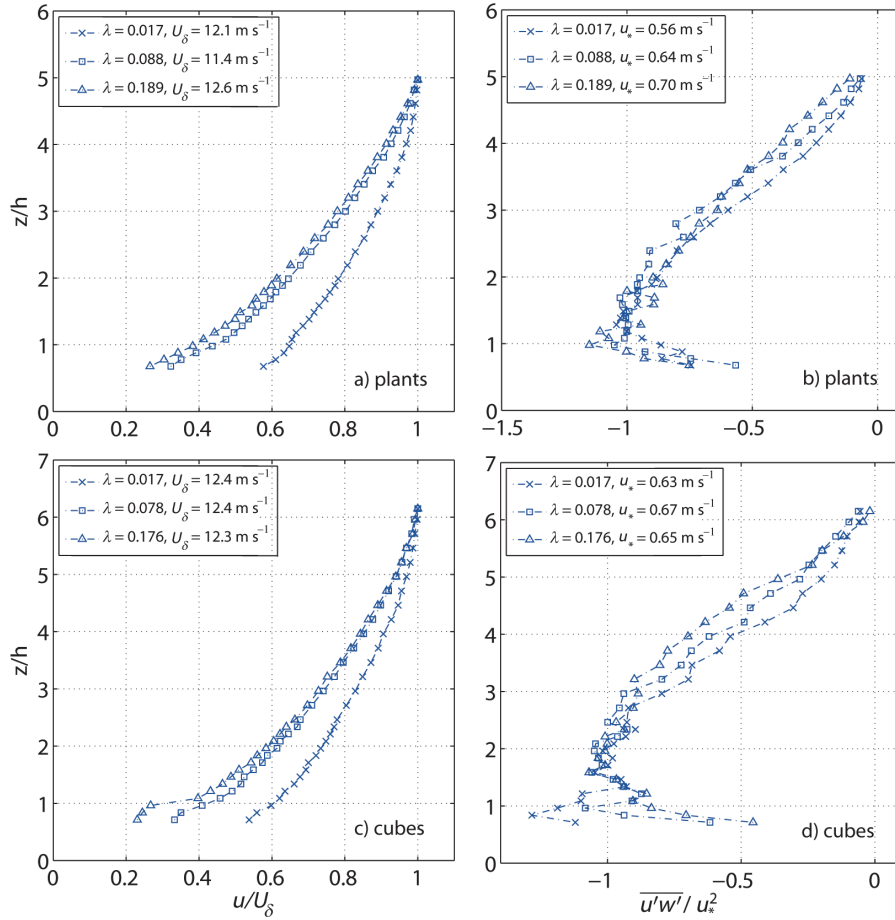


Fig. 4.3: Normalized mean wind  $u$  and kinematic Reynolds stress  $\overline{u'w'}$  profiles: (a) and (b) for the plant experiments, (c) and (d) for the cube experiments.  $U_\delta = 12 \text{ m s}^{-1}$ ;  $h = 0.1 \text{ m}$  for the plant and  $h = 0.08 \text{ m}$  for the cube cases.

The mean wind velocities directly above the roughness elements  $u(z/h = 1)$  were similar for the plant and the cube experiments at each roughness density  $\lambda$  (Fig. 4.3a and c). This demonstrates that flow conditions were comparable in the two cases, allowing comparison of the surface shear-stress distributions on the ground beneath the plants and the cubes. Plants streamline with the flow at higher wind velocities, resulting in aerodynamical shapes, reduced flow resistances of the plants, and thus in slightly higher wind velocities  $u(z/h = 1)$  compared to the cubes as shown in Fig. 4.3a and c. The mean velocity profile  $u(z)$  for the high density cube case shows a strong inflection near the top of the cubes consistent with a skimming flow regime where the flow above the roughness elements is weakly coupled with the flow among the roughness elements (Morris 1955). In the high density plant case the inflection is not clearly visible. This may be due to the fluctuating motions of the plants and their porous structure that may cause a weakening or even a suppression of flow separation around the plants. The low and the medium roughness densities are considered to be cases of isolated roughness and wake interference flow, and the associated shear-stress distributions will be discussed in the following section.

While keeping the free-stream velocity constant, the friction velocity in the constant-stress layer  $u_*$  increases steadily from  $u_* = 0.56 \text{ m s}^{-1}$  in the low to  $u_* = 0.70 \text{ m s}^{-1}$  in the

high density plant case (Table 4.1). For the cubes,  $u_* = 0.67 \text{ m s}^{-1}$  for the medium density, but decreases to  $u_* = 0.65 \text{ m s}^{-1}$  for the high density case suggesting a slight decrease in flow resistance induced by the high cube density due to the skimming flow regime. However,  $u_*$  is larger for the plants than for the cubes in the high density case suggesting an increase in flow resistance induced by the plants fluctuating motion. For both the plant and the cube cases, a maximum in the absolute values of the kinematic Reynolds stress profiles was found directly above the roughness elements at  $z/h \approx 1$  and remained nearly constant up to  $z/h \approx 2$  in the plant and  $z/h \approx 2.5$  in the cube case, similar to constant-stress layers found in the neutral boundary-layer.

### 4.3.2 Shear-stress partitioning

A common way to quantify the sheltering effect of non-erodible roughness elements is to determine the stress partition  $(\tau_s/\tau)^{1/2}$ , i.e. the surface shear-stress divided by the total stress above the canopy (Eq. (4.1)). Numerous wind-tunnel and field investigations have provided data on shear-stress partitioning by various types of roughness elements, roughness densities and roughness configurations. Fig. 4.4 shows a summary of some of these results along with our new measurements. These include the shear-stress partition for the average surface shear-stress on the exposed surface area  $(\tau_s'/\tau)^{1/2}$  (Fig. 4.4a) and the peak surface shear-stress  $(\tau_s''/\tau)^{1/2}$  (Fig. 4.4b). Good agreement was found between our data and these earlier studies, demonstrating that the Irwin sensors produce reliable surface shear-stress data. Both the average and the peak shear-stress on the surface decrease with increasing roughness densities  $\lambda$  as expected, with notable differences between the plant and cube experiments.

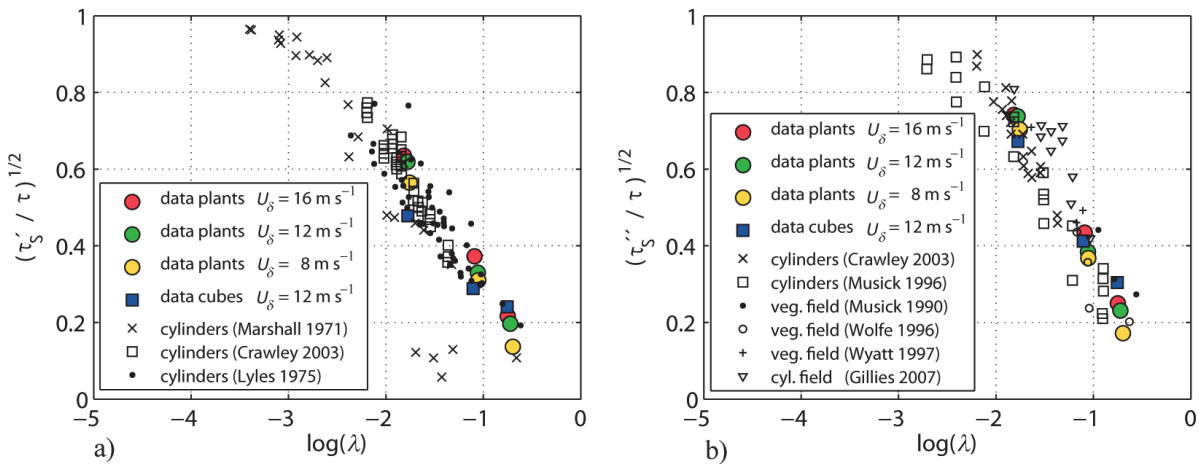


Fig. 4.4: Comparison of measured surface shear-stress ratios with literature data: (a) average surface shear-stress on exposed surface area  $\tau_s'$  and (b) peak surface shear-stress  $\tau_s''$ . Literature values measured in field experiments are indicated with “field” whereas the remaining data points were obtained by wind-tunnel measurements.

Because plants streamline with the flow, their frontal area  $A_f$  and thus the roughness density  $\lambda$  decrease with increasing wind speeds and become a function of the Reynolds number as demonstrated by Gillies et al. (2002) (Fig. 4.1c and d). The frontal area  $A_f$  first increases slightly by about 3% relative to  $A_f \approx 0.0033 \text{ m}^2$  in still air between  $U_\delta = 4 - 8 \text{ m s}^{-1}$  because the

plants flutter and expand in low to moderate winds. At higher wind velocities  $A_f$  decreases because the plants streamline with the flow, reaching about 90% of their still-air frontal area at  $U_\delta = 16 \text{ m s}^{-1}$ . The percentage increase and decrease of  $A_f$  are average values from multiple plants and several plant photographs, since the plants waving motion results in rapidly changing frontal areas. No significant differences in the change of  $A_f$  with wind speed were found for the three different roughness densities. This streamlining of the roughness elements results in higher wind speeds close to the ground and thus in increased average ( $\tau_s'$ ) and peak ( $\tau_s''$ ) surface shear-stress at the ground. The three data points for each plant canopy density  $\lambda$  in Fig. 4.4 correspond to three different free-stream velocities ( $U_\delta = 8, 12$  and  $16 \text{ m s}^{-1}$ ) and thus to three different Reynolds numbers defined as  $Re_h = U_\delta h/\nu$  where  $\nu = 1.5 \times 10^{-5} \text{ m}^2 \text{ s}^{-1}$  is the kinematic viscosity of air and  $h = 103, 99$  and  $94 \text{ mm}$  the average height of the plants at  $U_\delta = 8, 12$  and  $16 \text{ m s}^{-1}$ , respectively. Fig. 4.4 shows that with increasing  $Re_h$ ,  $(\tau_s'/\tau)^{1/2}$  and  $(\tau_s''/\tau)^{1/2}$  also increase.

Both the average and peak shear-stress partitions are larger for the plants than the cubes at the low roughness density ( $\log(\lambda) \approx -1.7$ ). The opposite is true at the high roughness density ( $\log(\lambda) \approx -0.7$ ), where the cubes result in larger shear-stress partitions. We hypothesize that in the high density plant canopy the flexible plants bend to cover a larger fraction of the surface, resulting in very low surface shear-stress. In the high density cube case, the flow penetrates slightly deeper into the canopy resulting in higher surface shear-stresses than in the plant case. Additionally, the total shear-stress  $\tau$  is lower for the high density cube case than for the high density plant case as discussed before in Section 4.3.1. This demonstrates that the shear-stress partition depends strongly on the type of roughness element used and that results based on rigid and non-porous roughness elements may not be adequate for the evaluation of erosion and sediment transport in real plant canopies.

### 4.3.3 Surface Shear-stress Spatial Variability

The shear-stress partitions from the previous section are either spatial averages  $(\tau_s'/\tau)^{1/2}$  or point data  $(\tau_s''/\tau)^{1/2}$  that might be used to estimate the integral total mass flux of sediment transport above a vegetation canopy or to determine the onset of particle erosion. Estimation of these quantities is a clear practical application of this study. However, for more precise modelling of sediment mass fluxes or the patterns of erosion and deposition expected on a partially-sheltered surface, the spatial and temporal variability of the surface shear-stress  $\tau_s(t, x, y)$  must also be known. Fig. 4.5 shows the spatial patterns of the surface shear-stress partition  $(\tau_s(x, y)/\tau)^{1/2}$  for the plants (left column) and cubes (right column). The shear-stress scaling at each canopy density is the same for the plant and cube cases and the lower limit is the same for all plots. The  $x$ - and  $y$ -axes were normalized by the cube side length and the average plant diameter, which are both  $D = 40 \text{ mm}$ .

Several features of the mean flow around the roughness elements can be inferred from the stress distributions shown in Fig. 4.5. The low shear-stress measured directly upwind of the roughness elements indicates the presence of a flow stagnation zone with reduced wind speeds. Within the wake region downwind of the roughness element, flow separation and reattachment result in a sheltered area with the lowest surface shear-stress. The flow convergence beside the roughness elements results in speed-up zones characterized by the



largest surface shear-stress. Sutton and McKenna-Neumann (2008) reported that rigid and non-porous roughness elements with well-defined flow separation at the edges result in the development of flow structures similar to horseshoe vortices wrapping around and paired counter-rotating eddies with a vertical axis immediately in the lee of the roughness element. Our plants consist of various small stems and blades shedding much smaller eddies than the cubes in diverse directions, suggesting that flow structures like horseshoe vortices and counter-rotating eddies may be less organized and coherent for vegetation than for the rigid cylinders used in their study. Increased shear-stress directly in front and behind the roughness elements (strongest in Fig. 4.5b, e) are interpolation artefacts that can be explained by the measurement resolution.

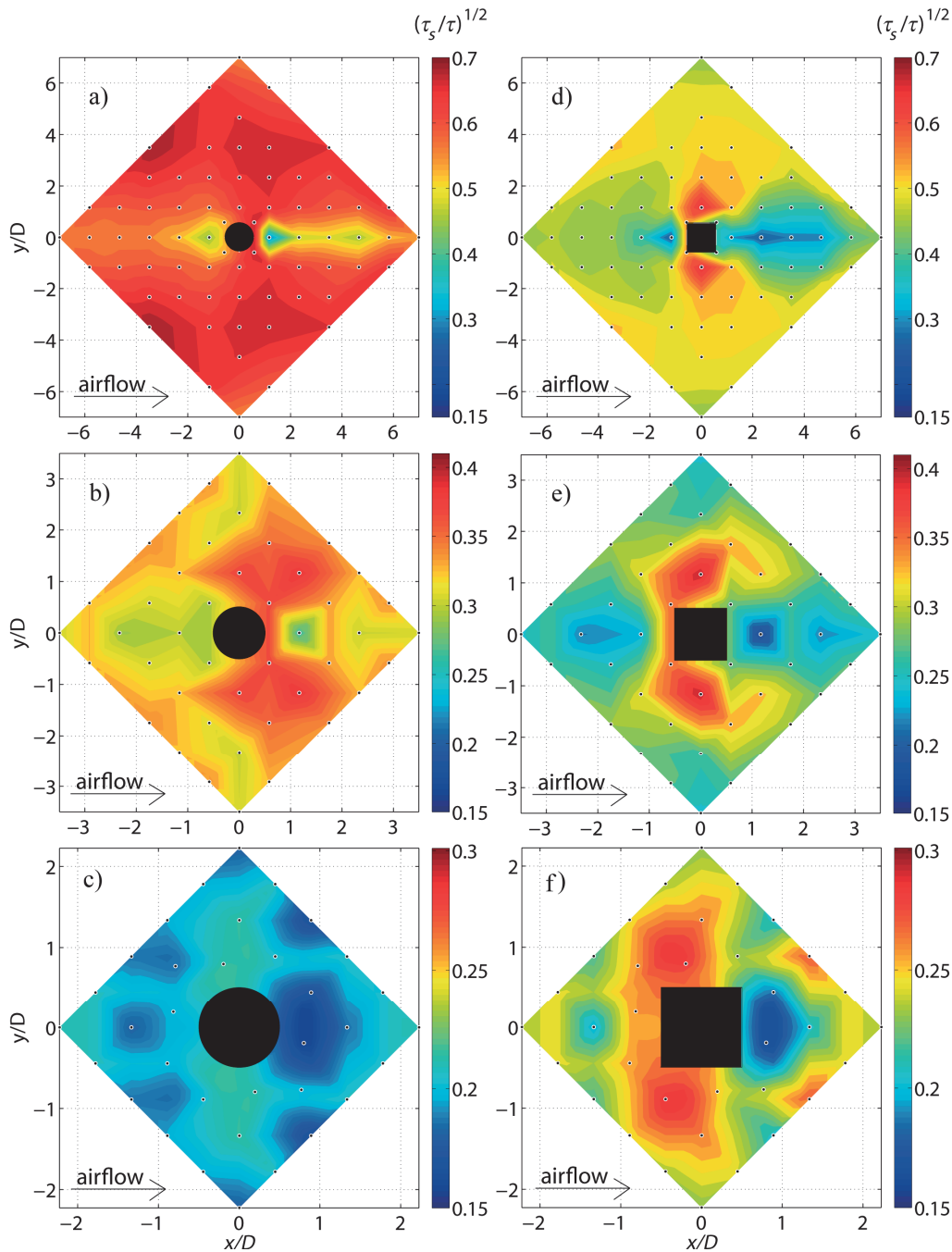


Fig. 4.5: Spatial distributions of the shear-stress partition  $(\tau_s(x, y)/\tau)^{1/2}$  for the three different roughness densities: (a)-(c) plants and (d)-(f) cubes for the low/medium/high roughness density cases at  $U_\delta = 12 \text{ m s}^{-1}$  ( $D = 40 \text{ mm}$ ).

As mentioned in the previous section, results from different roughness densities represent different flow regimes. The sheltered areas in both low roughness density cases do not reach the next roughness element downstream, so the low-density configuration in both cases (Fig. 4.5a, d) represents isolated roughness flow as defined by Morris (1955). In the medium density cases, the sheltered area reaches the next roughness element downstream while a significant fraction of the surface remains unsheltered, so these cases (Fig. 4.5b, e) are good examples of wake interference flow. For the high density plant case, the surface is almost completely sheltered suggesting a skimming flow regime (Fig. 4.5c). For the high density cube case, a maximum shear-stress partition of  $(\tau_s(x, y)/\tau)^{1/2} \approx 0.3$  was found in the speed-up zones, suggesting that the surface was not completely sheltered (Fig. 4.5f). However, the strong inflection found for the  $u(z)$  profiles in Section 4.3.1 indicates that this case was also a skimming flow regime. Comparing the surface shear-stress distributions for the plants with those for the cubes shows strong differences between the two, suggesting that a different sheltering effect can be expected from plants than from rigid roughness elements. This suggests that different local as well as total erosion and deposition rates can be expected, resulting in different erosion patterns and total mass fluxes.

Solid and inflexible roughness elements such as cubes generate a stronger lateral deflection of the airflow than do plants, resulting in higher flow speeds along their sides. This is substantiated by the fact that higher peak shear-stress values  $\tau_s''$  were found for the cubes than for the plants at all roughness densities (Table 4.1). Since the peak shear-stresses are responsible for the initiation of soil erosion, our results suggests that plants provide a better sheltering effect than cubes or other more natural rigid roughness elements such as stones. However, the fact that the total stresses  $\tau$  in the cube experiments are also larger than for the plants results in similar peak shear-stress partition values for the low and medium roughness densities (Fig. 4.4b and Fig. 4.5a,b,d,e). This is why the peak shear-stress partitions  $(\tau_s''/\tau)^{1/2}$  for the plants, cubes and other roughness elements from the literature are all within the same range (Fig. 4.4b). The stronger flow deflections around rigid obstacles result in higher peak surface shear-stresses as well as higher total shear-stress above the roughness elements due to increased flow resistance imposed by rigid rather than porous and flexible roughness elements.

The sheltered areas in the lee of the plants are significantly narrower with higher shear-stress ratios  $(\tau_s/\tau)^{1/2}$  than the cubes. This is most evident in Fig. 4.5a, d. The streamlining of the plants results in increasingly narrow sheltered areas at higher wind velocities. This can be shown by comparing the surface shear-stress in the planted cases with the surface shear-stress in the absence of any roughness elements  $\tau_{s0}$  as  $(\tau_s(x, y) - \tau_{s0})/\tau_{s0}$  at different free-stream velocities  $U_\delta$  (not shown here). For the cubes, however, these  $(\tau_s(x, y) - \tau_{s0})/\tau_{s0}$  plots are identical at different  $U_\delta$ , suggesting a Reynolds-independent flow. The Reynolds number  $Re_h$  for the cube cases varies between 42,000 and 85,000 with a consistent cube height  $h = 80$  mm. In this range, the drag coefficient of cylinders or cubes are Reynolds-number independent (Schlichting 1936) confirming our finding that the sheltering effect of the cubes is not dependent on the speed of the flow.

Solid circular cylinders may have provided a better representation of real plants, since their bulk shape is more similar to that of a plant than the cube shape. However, preliminary experiments comparing the surface shear-stress on the ground beneath a single live plant and



a single circular cylinder of similar size show differences comparable to those found between the plant canopies and the cube arrays, e.g. larger shelter areas and higher peak stress values  $\tau_s''$  for the cylinder. Furthermore, the cylinder was found to result in even higher  $\tau_s''$  values than the cubes. This can be explained by the flow separation at the vertical windward edges of a cube that results in higher turbulence generated and less speed-up of the flow than around a cylinder with a more streamlined shape. This finding suggests that in some cases, cubes may actually be better representations of live plants than cylinders.

### 4.3.4 Time Series Statistics

#### 4.3.4.1 Turbulence Intensities

The normalized turbulence intensity distributions  $\zeta(x, y)$  (Eq. (4.3)) for the low roughness density cases shown in Fig. 4.6 display the increase or decrease in  $\sigma_u$  caused by the roughness elements relative to the smooth floor case. Higher normalized turbulence intensities  $\zeta$  were found at all roughness densities in experiments with cubes than those with plants. The peak values of the normalized turbulence intensity  $\zeta$  for the plants were found in the wake areas and are consistent from the low to the high density case with an increase in  $\sigma_u$  of about 40% ( $\zeta = 1.4$ ) relative to the smooth floor case. In contrast, the peak values for  $\zeta$  in the cube cases ( $\zeta = 2.2$  for the low,  $\zeta = 1.7$  for the medium and  $\zeta = 1.5$  for the high density) are mainly found upwind and at the sides of the cubes, a region that matches the horseshoe vortices observed by Sutton and McKenna-Neumann (2008) (Fig. 4.6b). This suggests that the high turbulence intensities  $\zeta$  in the cube cases may result from horseshoe vortices. Furthermore, the low values of  $\zeta$  in the plant cases supports the hypothesis that horseshoe vortices are suppressed as suggested in Section 4.3.3.

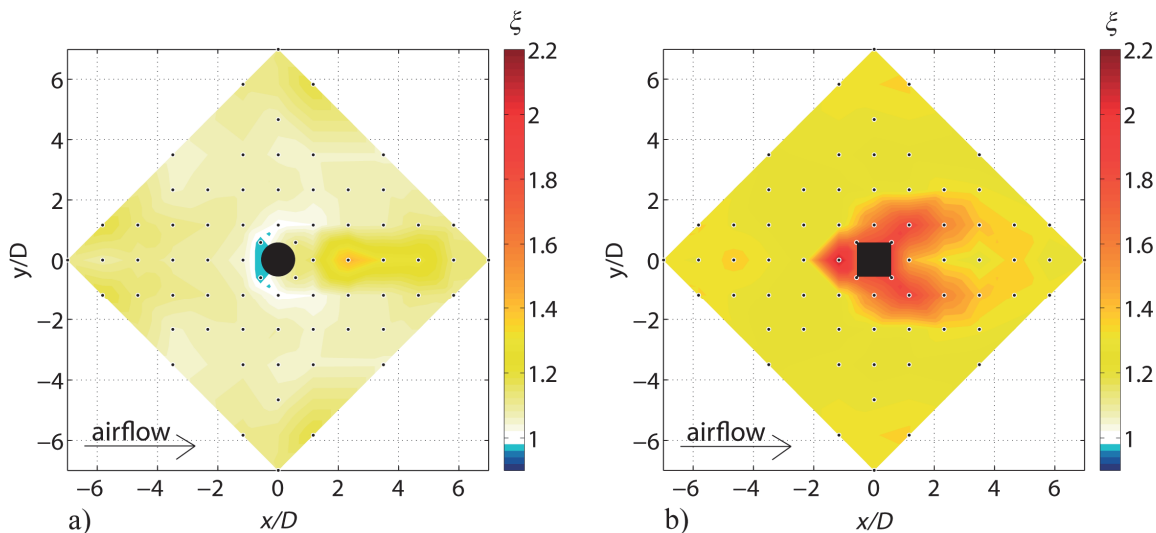


Fig. 4.6: Normalized turbulence intensity distributions  $\zeta(x, y)$  showing the increase in  $\sigma_u$  close to the ground relative to the smooth floor case: (a) plants and (b) cubes (low roughness density,  $U_\delta = 16 \text{ m s}^{-1}$ ,  $D = 40 \text{ mm}$ ).

Plants appear to cause lower turbulence levels close to the ground than cubes due to the streamlining behaviour of the plants resulting in more favourable aerodynamical shapes. The lower near ground turbulence intensities also support our finding that plants provide a better

sheltering effect than rigid roughness elements. It is remarkable that even for the low near-ground mean wind velocities in the high density plant and cube case,  $\sigma_{u,R}$  is everywhere still larger than  $\sigma_{u,S}$ , e.g.  $\xi > 1$  (not shown here). These results agree with those of Sutton and McKenna-Neumann (2008). Values of  $\xi$  slightly lower than one are found directly upwind of the plants in the low density case. Despite the increased turbulence intensities found in the presence of roughness elements, the horizontal velocity variations  $u'$  in the sheltered area downwind of the roughness elements seem to be poorly correlated with the vertical velocity fluctuations  $w'$ . This is due to a reduced downward momentum flux and thus reduced surface shear-stress found in the wake area of the roughness elements (see Fig. 4.5 and Fig. 4.6).

#### 4.3.4.2 Threshold Friction Velocity

The spatial patterns of the percentage of time  $\psi(x, y)$  (Eq. (4.4)) that a fluid threshold skin friction velocity  $u_{\tau t} = 0.35 \text{ m s}^{-1}$  was exceeded during our experiments show interesting similarities to patterns of erosion and deposition found in an earlier study at the SLF wind-tunnel (Burri et al. 2011b and Burri, 2011c). Burri et al. (2011b) investigated the vertical profiles of drifting sediment mass flux in live plant canopies of various densities. The sediment used in that study was a commercial quartz sand with grain diameters between  $d = 0.4 - 0.8 \text{ mm}$ . Those authors found a fluid threshold friction velocity of  $u_{*t} = 0.3 \text{ m s}^{-1}$  (at  $U_\delta = 8 \text{ m s}^{-1}$ ) at the onset of erosion for an unplanted sand surface. We calculate their fluid threshold skin friction velocity (see Section 2.2.2) as  $u_{\tau t} = u_{*t} + 2\sigma(u_\tau)$ , where the standard deviation  $\sigma(u_\tau) = 0.025 \text{ m s}^{-1}$  at  $U_\delta = 8 \text{ m s}^{-1}$  was determined from the temporal skin friction velocity variations measured with Irwin sensors on the smooth wooden floor without roughness elements for the present study. By adding  $2\sigma(u_\tau)$  we assume that the 5% of the skin friction velocities that are higher than  $u_{*t} + 2\sigma(u_\tau)$  are responsible for the initiation of particle erosion on the unsheltered sand surface.

Fig. 4.7a-d show  $\psi(x, y)$  for the low and the medium density plant and cube case at  $U_\delta = 16 \text{ m s}^{-1}$ . For  $\psi = 1$ , the threshold  $u_{\tau t}$  at the surface is exceeded at all times, indicating a region of erosion. For  $\psi = 0$ , the sediment transport threshold was never exceeded, so deposition of incoming particles should always be possible. However, for  $0 < \psi < 1$ , erosion and deposition are both possible, and the magnitude of local net erosion or deposition depends on the value of  $\psi$ . For  $\psi = 0.5$ , the local temporally averaged skin friction velocity  $u_\tau$  approximately equals the threshold value  $u_{\tau t} = 0.35 \text{ m s}^{-1}$ . Local net deposition might thus be predicted for  $\psi < 0.5$  and local net erosion for  $\psi > 0.5$ . The parameter  $\psi$  was chosen to illustrate local erosion and deposition patterns rather than  $u_\tau$  because the upper and lower limit for erosion and deposition are clearly defined as  $\psi = 1$  and  $\psi = 0$ , and because  $\psi$  is directly related to the number of erosive events that occur when larger eddies hit the surface.

Fig. 4.7e, f are photographs taken with a vertical perspective at the measurement section that show the erosion and deposition patterns of sand for the low and medium plant density cases with illumination from the side (Burri et al. 2011b). Prior to these photographs, a free-stream velocity of  $U_\delta = 16 \text{ m s}^{-1}$  persisted for approximately 200 sec while drifting sand was present. The erosion and deposition patterns are qualitatively in excellent agreement with the spatial patterns of  $\psi$  found in our plant experiments (Fig. 4.7c, d). The deposited (or undisturbed) sand upwind and in the lee of the plants in the low density plant case (Fig. 4.7e)

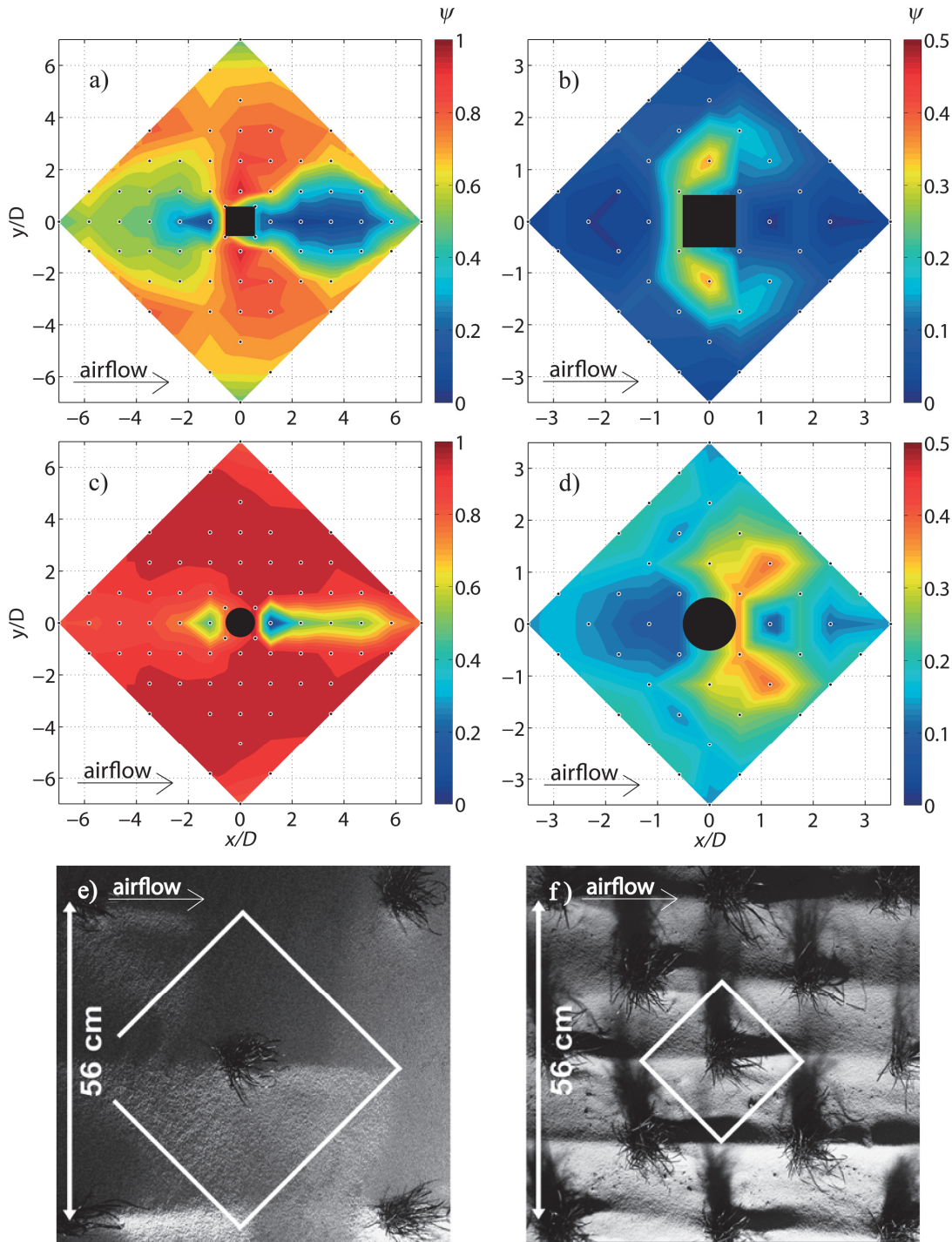


Fig. 4.7: Percentage of time  $\psi$  that a fluid threshold skin friction velocity  $u_{\tau} = 0.35 \text{ m s}^{-1}$  was exceeded for the low and the medium cube (a and b) and plant (c and d) density cases ( $U_{\delta} = 16 \text{ m s}^{-1}$ ,  $D = 40 \text{ mm}$ ). (e) and (f) are vertical photographs of plants and corresponding erosion patterns illuminated from the side for the low and medium roughness density of sand erosion experiments in live plant canopies ( $U_{\delta} = 16 \text{ m s}^{-1}$ ) (from Burri et al. 2011).

corresponds with the areas where  $\psi < 0.75$  in Fig. 4.7c. This shows that suppression of erosion and particle deposition are possible even if the skin friction velocity exceeds the threshold value  $u_{\tau}$  during 75% of the time. This is likely due to sand particles hitting the plant, losing some of their momentum, and being deposited in the wake behind the plant. In the medium density plant experiment (Fig. 4.7d, f), strong net erosion occurred outside the

sheltered area even at low  $\psi$  ( $0.25 < \psi < 0.5$ ). We hypothesize that this is due to a reduction in threshold skin friction velocity  $u_{\tau}$  after sediment transport has been initiated, as saltating particles can dislodge stationary particles on impact (Bagnold 1943). Therefore, for the case of sand transport in plant canopies discussed here, when  $\psi > 0.75$  erosion dominates, and for  $\psi < 0.25$  deposition does. In the range  $0.25 < \psi < 0.75$ , either may be true. For the high roughness density cases,  $\psi < 0.05$  was found everywhere in both the plant and the cube cases and the surface was entirely sheltered. This result is supported by the negligibly small total sediment mass flux found for the high density case by Burri et al. (2011b).

The strong differences in the spatial patterns of  $\psi$  in the cube and the plant cases (Fig. 4.7a-d) show that very different erosion patterns and perhaps differences in the total sediment mass flux would be expected in sediment transport experiments using cubes. This supports our assertion that investigations using rigid roughness elements may not provide appropriate data from which to draw conclusions regarding natural plant canopies.

It should be pointed out that a comparison between sand erosion patterns and surface shear-stress measurements in the absence of drifting sand may not be strictly appropriate. Drifting sand interacts with the boundary-layer and causes deceleration of the airflow within the saltation layer (Bagnold 1943). The drifting sand cases may thus have had slightly lower skin friction velocities than those measured with the Irwin sensors in the absence of drifting sand. Also, the topography of the surface changes when erosion and deposition take place, resulting in changes to the surface shear-stress distribution and the local wind field. The good correlation between the patterns of  $\psi$  and sediment erosion suggests that while these limitations might mean that the absolute values of  $\psi$  in the two cases were not identical, their spatial distributions were very close.

The above findings suggest that  $\psi$  could be a useful parameter for determining local erosion and deposition rates. Furthermore, our results demonstrate the importance of knowing the spatial and temporal variability of the shear-stress on the ground, rendering this method somewhat impractical for field studies. Experiments performed by Valyrakis et al. (2010) in a flume with a single coarse sediment grain (diameter: 12.7 mm) showed that not only the magnitude but also the duration of high surface shear events defines the onset of particle entrainment. We thus anticipate future work on this issue involving a similar study for smaller sand grains (0.4 - 0.8 mm) such as those used by Burri et al. (2011b) to define a criterion for the onset of local sand entrainment. This together with measurements of the local skin friction velocity time series can then be used to improve predictions of sand erosion magnitudes.

## 4.4 Summary and Conclusions

Several distinctive differences between spatiotemporally resolved surface shear-stress variations on the ground beneath live plant canopies and rigid cube arrays were found. Although the cubes provided a higher overall sheltering effect at the low and medium roughness density, identical experiments with plants generated lower average and peak surface shear-stress partitions at the high roughness density. However, the plant canopies had lower absolute peak shear-stress values at all roughness densities than the rigid cube arrays. The plants streamline with the flow, resulting in a decreasing sheltering effect at higher wind

velocities due to the narrower sheltered areas in their wakes. The patterns of surface shear-stress on the ground beneath the plants and cubes suggest significant differences in erosion and deposition patterns in such canopies.

The peak near-ground turbulence intensities are about 40% higher in the sheltered area relative to the smooth floor case at all plant densities. In contrast, the peak turbulence intensities upwind and at the sides of the cubes are 120%, 70% and 50% higher in the low, medium and high density cases relative to the smooth floor case. The turbulence intensity distributions support the hypothesis that horseshoe vortices are weakened or actually suppressed in the plant case.

The spatial patterns of the percentage of time when a certain threshold skin friction velocity is exceeded show compelling similarities to sand erosion and deposition patterns around plants found in a companion study (Burri et al. 2011b). We demonstrated that for our controlled experiments, net deposition (or no net erosion) is still possible even when the threshold value for erosion is locally exceeded 75% of the time, and that net erosion is possible even if the threshold is exceeded only 25% of the time.

Most importantly, all of our results demonstrate that rigid, non porous roughness elements provide inadequate approximations of live plants. Results from many earlier studies using rigid roughness elements may thus have limited application in studies of the sheltering effect of live plants on sediment transport and soil erosion in natural environments.

### **Acknowledgements**

We would like to thank the Swiss National Science Foundation (SNF) and the Vontobel foundation for financial support. The SLF workshop and GS technology assisted the development and the production of the measurement technique and the experiment set-up. Dr. Katrin Burri and Benjamin Eggert helped with the wind-tunnel experiments and provided many fruitful discussions.



# 5 Shear-stress partitioning in live plant canopies and modifications to Raupach's model

Walter B, Gromke C, Lehning M (2012c) *Shear stress partitioning in live plant canopies and modifications to Raupach's model. Boundary-Layer Meteorology*, doi:10.1007/s10546-012-9719-4

## 5.1 Introduction

Desertification driven by wind erosion, reduced accumulation of snow in arid regions or the development of dust storms entering areas with a high population density are all examples of the influences of aeolian processes on our steadily changing environment. During the last decade, numerical modelling of such aeolian processes to predict for example local water storage as snow in arid regions or the aggravation of desertification has become significant in environmental sciences. Model validation by means of experiments is essential to verify accuracy of predictions. Often, experiments are also necessary to determine model parameters.

The local surface shear stress  $\tau_S(x, y)$ , acting on the ground beneath plant canopies is the key parameter when identifying the shelter capability of vegetation against particle erosion and when modelling aeolian processes. Here,  $x$  is the streamwise and  $y$  the transverse direction of the flow (Fig. 5.1). The spatial peak surface shear stress  $\tau_S''$  defines the onset of erosion whereas most sediment transport models use the average friction velocity  $u_* = (\tau/\rho)^{1/2}$  on a surface to determine the magnitude of particle mass fluxes (e.g., Bagnold 1943). Raupach (1992) and Raupach et al. (1993) developed a model that allows the prediction of the total stress  $\tau$  as well as the peak  $(\tau_S''/\tau)^{1/2}$  and the spatial average  $(\tau_S'/\tau)^{1/2}$  shear stress ratio as a function of a set of parameters that describe the geometric and the aerodynamic roughness of the surface. This model has been repeatedly tested by means of several wind tunnel and field studies (Marshall 1971; Musick et al. 1996; Wolfe and Nickling 1996; Wyatt and Nickling 1997; Crawley and Nickling 2003; King et al. 2006; Gillies et al. 2007; Brown et al. 2008). However, all these studies are either from the field mainly using live plants with the limitation that wind conditions could not be controlled, or from wind tunnels using rigid and non porous plant imitations, which often (but not always, as will be shown in this study) poorly reflect the aerodynamic behaviour of live vegetation. Such plant imitations often result in strong differences in the surface shear stress distributions  $\tau_S(x, y)$  and in the peak surface

shear stress  $\tau_S''$  on the ground compared to live plants (Walter et al., 2012b). The highly irregular structures of live plants can be extremely flexible and porous allowing them to streamline with the flow. Hence, live plants cause considerable differences in the drag and flow regimes (e.g., Gromke and Ruck 2008) as well as in the size of the shed eddies compared to rigid and non-porous imitations.

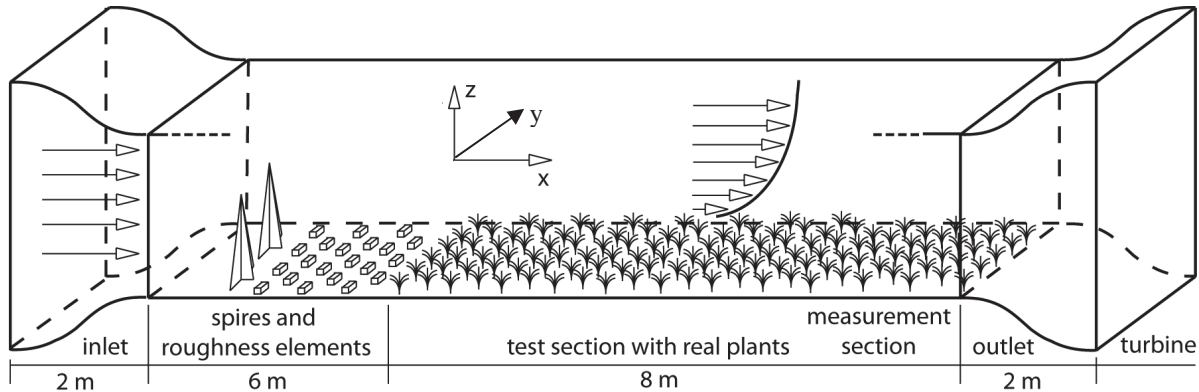


Fig. 5.1: Sketch of the SLF boundary-layer wind tunnel.

The model of Raupach (1992) and Raupach et al. (1993) incorporates up to four parameters and fits any of the data of different experiments from the literature reasonably well. Unfortunately, as a result, the range of possible values for the parameters obtained from the studies cited above is relatively large because of different experimental setups and roughness elements used. This makes it difficult for modellers to identify appropriate values for a specific vegetation canopy or surface with non-erodible roughness elements. Furthermore, no study systematically investigated how well the model predicts the differences in the shear stress ratios for different kinds of roughness elements such as cubes, cylinders, hemispheres or live plants. Most studies used solely one kind of roughness elements, sometimes of different size, to obtain variations in the roughness density  $\lambda$ . The roughness density  $\lambda$  is defined as the roughness element frontal area  $A_f$  divided by the ground area  $S$  per roughness element. An intercomparison between the studies is often restricted by the varying experiment setups and measurement techniques deployed resulting in disparate measurement accuracies. Some studies used Irwin sensors (Irwin 1981) or drag plates to measure the surface shear stress (e.g., Crawley and Nickling 2003; Brown et al. 2008) whereas other studies determined the friction velocity at the onset of particle entrainment from wind profiles (e.g., Marshall 1971; Musick et al. 1996).

This study presents an application and extension of Raupach's model to surface shear stress measurements in live plant canopies of a single species (*lolium perenne*) of varying roughness density and arrays of rectangular blocks to investigate and discuss the research gaps identified above. Model parameters a priori determined according to their definition are compared to their corresponding values obtained from least-square fits to the stress ratio data as well as to literature values. The ability of the model to predict the total stress  $\tau$ , the peak  $(\tau_S''/\tau)^{1/2}$  and the average  $(\tau_S'/\tau)^{1/2}$  shear stress ratio for the plant canopies and the block arrays



is tested. Finally, a model modification is presented that improves and facilitates its applicability in predicting peak stress ratios  $(\tau_S''/\tau)^{1/2}$  and suggests to replace the problematic  $m$ -parameter with a more universal parameter.

## 5.2 Background and Theory

Schlichting (1936) first defined the shear stress ratio for a rough surface as  $\tau = \tau_S + \tau_R$  where  $\tau$  is the total stress on the entire canopy,  $\tau_S$  the average surface shear stress on the ground beneath the roughness elements and  $\tau_R$  the stress on the roughness elements. A model that predicts the stress ratio  $(\tau_R/\tau)^{1/2} = a_1 \ln(1/\lambda) + a_2$  as a function of the roughness density  $\lambda$  and two fit parameters  $a_i$  was presented by Wooding et al. (1973), but fails for  $\lambda > 0.05$  (Raupach 1992). Arya (1975) presented a model for two dimensional roughness elements transverse to the mean wind that states  $(\tau_R/\tau)^{1/2} = [1 + (1 - a_3 \lambda) / (\lambda C_R / C_S)]^{-1}$  and Raupach (1992) presented an analytical treatment for predicting the total stress  $\tau$  and the shear stress ratio  $(\tau_R/\tau)^{1/2} = (\beta \lambda / (1 + \beta \lambda))^{1/2}$  and thus  $(\tau_S/\tau)^{1/2} = (1 / (1 + \beta \lambda))^{1/2}$  for three dimensional roughness elements. Here,  $\beta = C_R / C_S$  is the ratio of the roughness element and the surface drag coefficient. The model of Arya (1975) predicts the stress ratio as well as the model of Raupach (1992) except at  $\lambda > 0.1$  where Arya's model predicts  $\tau_R/\tau > 1$ , which is physically implausible. The widely accepted model of Raupach (1992 and et al. 1993) is entirely based on physically defined parameters and allows the prediction of the stress ratios  $\tau_R/\tau$  and  $\tau_S/\tau$  for different rough surfaces by determining solely  $\beta$  and  $\lambda$ . It must be noted that the roughness density  $\lambda$  is a geometric value that can easily be determined whereas the drag coefficients  $C_R$  and  $C_S$ , which define  $\beta$ , are flow dependent properties of the surface and the roughness elements. The drag force on an isolated roughness element can be written as

$$\Phi = \rho C_R b h U_h^2 \quad (5.1)$$

and defines  $C_R$  (Raupach 1992). Here,  $\rho$  is the air density,  $U_h$  the mean wind velocity at the roughness element height  $h$  and  $b$  is the roughness element width. Raupach (1992) further defined an unobstructed drag coefficient  $C_S$  for the substrate surface such that:

$$\tau_S(\lambda = 0) = \rho C_S U_h^2 \quad (5.2)$$

The model of Raupach is further based on the definition of an effective shelter area  $A$  and shelter volume  $V$  as well as on two hypotheses. The effective shelter area  $A$  is defined as “the area in the wake of the roughness element in which the stress on the ground  $\tau_S$  must be set to zero, to produce the same integrated stress deficit as that induced by the sheltering element” (Raupach 1992). “The effective shelter volume  $V$  describes the effect of a given roughness element upon the drag forces on other elements in its vicinity. It is the volume within which the drag force on the array of test obstacles must be set to zero, to produce the same integrated force deficit as induced by the sheltering element” (Raupach 1992). Hypothesis I states that the assumed wedge shaped shelter area  $A$  and shelter volume  $V$  scale according to:

$$A = c_1 b h U_h / u_* \quad (5.3)$$

$$V = c_2 b h^2 U_h / u_* \quad (5.4)$$

Here,  $u_*$  is the friction velocity and  $c_1$  and  $c_2$  are constants of proportionality of  $O(1)$ . Hypothesis II states that “when roughness elements are distributed uniformly or randomly across a surface, the combined effective shelter area or volume can be calculated by randomly superimposing individual shelter areas or volumes” (Raupach 1992). The above definitions and hypotheses are then used to determine the surface shear stress  $\tau_S$  and the stress on the roughness elements  $\tau_R$  according to:

$$\tau_S = \rho C_S U_h^2 \exp\left[-c_1 \left(\frac{U_h}{u_*}\right) \lambda\right] \quad (5.5)$$

$$\tau_R = \lambda \rho C_R U_h^2 \exp\left[-c_2 \left(\frac{U_h}{u_*}\right) \lambda\right] \quad (5.6)$$

The model thus allows the prediction of the total stress  $\tau = \tau_S + \tau_R$  on the entire surface using Eq. (5.5) and (5.6), which results in an implicit equation for  $u_*$ . To solve this equation the assumption  $c_1 = c_2 = c$  is made, which can be interpreted as “the elements shelter the ground and each other with the same efficiency” (Raupach 1992). This finally results in the implicit equation for  $U_h/u_*$ :

$$\frac{U_h}{u_*} = (C_S + \lambda C_R)^{-1/2} \exp\left[\frac{c\lambda}{2} \left(\frac{U_h}{u_*}\right)\right] \quad (5.7)$$

The stress ratio prediction of Raupach can then be obtained by using Eq. (5.5) and (5.6) and assuming again  $c_1 = c_2 = c$ :

$$\frac{\tau_S}{\tau} = \frac{1}{1 + \beta\lambda} \quad (5.8a)$$

$$\frac{\tau_R}{\tau} = \frac{\beta\lambda}{1 + \beta\lambda} \quad (5.8b)$$

In Eq. (5.8a),  $\tau_S$  is the average surface shear stress on the total surface area  $S$  rather than on the exposed surface area  $S'$ . Raupach et al. (1993) suggested the average surface shear stress on the exposed surface area  $S'$  to be  $\tau_S' = \tau_S/(1-\sigma\lambda)$  where  $\sigma$  is the ratio of the roughness element basal area to frontal area and  $\sigma\lambda = 1-S'/S$  the basal area index (the basal area per unit ground area). This results in:

$$\left(\frac{\tau_S'}{\tau}\right)^{1/2} = \left(\frac{1}{(1-\sigma\lambda)(1+\beta\lambda)}\right)^{1/2} \quad (5.9)$$

Eq. (5.9) was validated by various measurements and investigations (e.g., Marshall 1971; Crawley and Nickling 2003). Raupach et al. (1993) further argued that not the spatially averaged  $\tau_S'$  but rather the spatial peak surface shear stress  $\tau_S''$  at any location on the surface is responsible for the initiation of particle erosion. According to this, a rather empirical assumption on the relation between  $\tau_S''$  and  $\tau_S'$  was made due to the limited surface shear stress data available at that time. Raupach et al. (1993) defined that  $\tau_S''$  for a surface with roughness density  $\lambda$  is equal to  $\tau_S'$  for a less dense (lower  $\lambda$ ) rough surface composed of the same roughness elements:

$$\tau_s''(\lambda) = \tau_s'(m\lambda) \quad (5.10)$$

Here,  $m$  is supposed to be a constant  $\leq 1$ , which accounts for the difference between  $\tau_s''$  and  $\tau_s'$ . This finally results in the equation for the peak surface shear stress ratio:

$$\left(\frac{\tau_s''}{\tau}\right)^{1/2} = \left(\frac{1}{(1-m\sigma\lambda)(1+m\beta\lambda)}\right)^{1/2} \quad (5.11)$$

Eq. (5.11) has been validated by several wind tunnel and field experiments (e.g., Musick and Gillette 1990; Musick et al. 1996; Wolfe and Nickling 1996; Wyatt and Nickling 1997; Crawley and Nickling 2003). However, most studies used estimated values of  $C_R$  and  $C_S$  to determine the parameter  $\beta$  and applied best fit methods to obtain  $m$ . Wyatt and Nickling (1997) found  $m = 0.16$  for sparse desert creosote communities whereas Crawley and Nickling (2003) found  $m = 0.5-0.6$  for solid cylindrical roughness elements with a slight dependency of  $m$  on wind velocities. They further found a strong overestimation of the stress ratio prediction (Eq. (5.11)) when using  $m$  values obtained from the independent parameter definition (Eq. (5.10)). Brown et al. (2008) found that the prediction (Eq. (5.11)) works equally well for both, staggered roughness element arrangements and for more randomly arranged surface features. However, all these studies show that the  $m$ -parameter is not universal. Furthermore, the model of Raupach is based on a scaling argument (Eq. (5.3) and (5.4)) and stops behaving sensibly for  $U_h/u_*$  at roughness densities larger than about  $\lambda \approx 0.1 - 0.3$  (Raupach, 1992). Shao and Yang (2005) and (2008) presented extensions of the model for high roughness densities  $\lambda > 0.1$  with the argument that it is not clear how the effective shelter areas and volumes superimpose at higher roughness densities.

### 5.3 Methodology

Measurements of surface shear stress distributions  $\tau_s(x, y)$  on the ground beneath live plant canopies and rigid block arrays of different roughness densities  $\lambda$  were performed in the SLF atmospheric boundary-layer wind tunnel (Walter et al. 2009; Walter et al. 2012a; Walter et al. 2012b). The wind tunnel (Fig. 5.1) is 14 m long, has a cross section of 1 m  $\times$  1 m and has been used mainly in winter for investigating saltation, ventilation and the aerodynamic roughness length of naturally fallen snow (Clifton et al. 2006; Clifton and Lehning 2008; Clifton et al. 2008; Guala et al. 2008; Gromke et al. 2011) and in summer to investigate the sheltering effect of live plants against soil erosion (Burri et al. 2011a; Burri et al. 2011b).

The 8 m long test section covered with live plants allows for the generation of a natural boundary-layer flow (Walter et al. 2009). The wooden blocks (rectangular blocks with square basal cross-section of 40 mm  $\times$  40 mm and height of 80 mm) and the live plants (species: *lolium perenne*, height: 100 mm) were arranged in staggered rows on the wind tunnel ground (Fig. 5.2a, b). Four different roughness densities were investigated: 0, 5.25, 24.5, 55 plants or blocks  $m^{-2}$ , hereafter referred to as smooth-floor, the low-, medium- and high-density case, respectively, with  $\lambda = 0.017, 0.087$  and  $0.200$  for the plants (still air) and  $\lambda = 0.017, 0.078$  and  $0.176$  for the blocks. These configurations were investigated at three different free stream velocities  $U_\delta = 8, 12$  and  $16$  m  $s^{-1}$  to systematically determine the

differences in the shear stress ratios when using live plants rather than rigid and non-porous plant imitations. All measurements were performed at the downwind end of the test section. A 6 m long fetch with spires and additional artificial roughness elements was used upwind of the test section for preconditioning the boundary-layer flow (Fig. 5.1). The boundary-layer thickness was about  $\delta = 500$  mm and it was shown that the inertial sublayer was sufficiently developed (Walter et al., 2009).

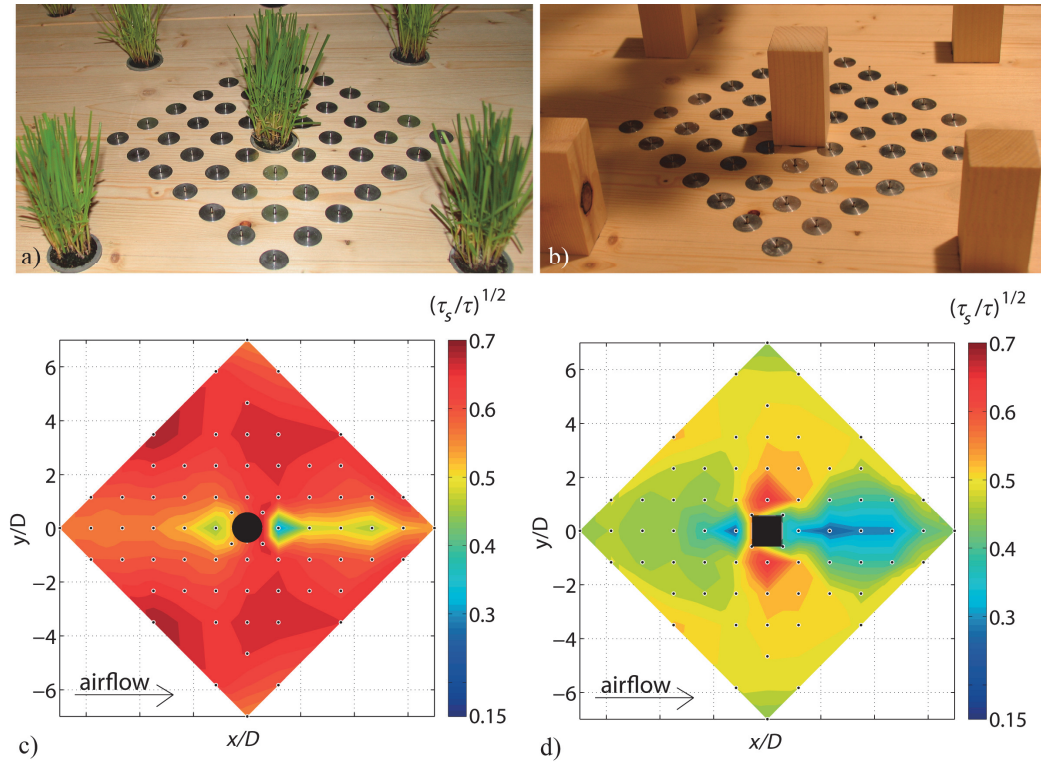


Fig. 5.2: Irwin sensors flush mounted with the wooden wind tunnel ground for the medium-density (a) live plant canopy (still air  $\lambda = 0.087$ ) and (b) wooden block array ( $\lambda = 0.078$ ). (c) and (d) show the surface shear stress distribution  $(\tau_s/\tau)^{1/2}$  for the low-density plant canopy ( $\lambda = 0.017$ ) and wooden block array ( $\lambda = 0.017$ ) at  $U_\delta = 12$  m s<sup>-1</sup> ( $D = 40$  mm; taken from Walter et al., 2012b)

Thirty-two Irwin sensors (Irwin 1981) were mounted flush with the wind tunnel floor in an array surrounding a roughness element to measure the surface shear stress distribution  $\tau_s(x, y)$  (Fig. 5.2a, b). The pressure differences at the sensors were measured using a custom made 32-channel pressure scanner (sampling rate: 200 Hz). Flow characteristics like vertical profiles of the mean wind velocity  $u$  and the kinematic Reynolds stress  $-\overline{u'w'}$  were measured using two-component hot-film anemometry (model: *Dantec Streamline*; sampling rate: 20 kHz) to determine the total stress  $\tau = \rho u_*^2 = -\rho \overline{u'w'}$  in the constant stress layer above the canopy, and to assure that well developed boundary-layers were generated (Walter et al., 2011b). Two-component hot-film anemometers are known to underestimate the kinematic Reynolds stress  $-\rho \overline{u'w'}$  in highly turbulent flows (Raupach et al. 1991). However, our kinematic Reynolds stress profiles (as presented in Walter et al., 2012b) suggest no measurement problems in the constant stress layer above the plant canopies and block arrays where  $u_*$  was determined. All shear stress and velocity values are 30 s time averaged.

Fig. 5.2c and d show the surface shear stress distribution  $\tau_s(x, y)$  as a fraction of the total stress  $\tau$  for the low-density plant and block case at a free stream velocity of  $U_\delta = 12 \text{ m s}^{-1}$  (taken from Walter et al., 2012b). The accuracy of the skin friction velocity  $u_\tau = (\tau_s/\rho)^{1/2}$  measurements averages to about  $\pm 5\%$  for  $u_\tau > 0.13 \text{ m s}^{-1}$  (Walter et al., 2012a). Additional details about the experiment setup and the measurements can be found in Walter et al. (2009) and (2012b). The accuracy of the Irwin sensor and the hot-film measurements are discussed in detail in Walter et al. (2012a).

## 5.4 Results and discussion

### 5.4.1 Total Stress Prediction

To predict the total stress  $\tau = \rho u_*^2$  on a canopy with non-erodible roughness elements using Eq. (5.7), the roughness element and the surface drag coefficients  $C_R$  and  $C_S$ , the roughness density  $\lambda$ , the mean velocity  $U_h$  at the top of the roughness elements and the constant of proportionality  $c$  need to be known.

Some studies (e.g., Brown et al., 2008) determined  $C_R$  and  $C_S$  by measuring the force on a single, wall-mounted roughness element and the surface using drag plates. However, in this study, the force  $\Phi$  (Eq. (5.1)) on a single roughness element was estimated using the difference between the total stress  $\tau$  above and the surface shear stress  $\tau_s'$  on the exposed surface area  $S'$  for the low-density case (5 roughness elements per  $\text{m}^2$ ,  $\lambda = 0.017$ ) with an isolated roughness flow regime to estimate  $C_R$  according to:

$$\Phi = \rho C_R b h U_h^2 \approx \tau S - \tau_s' S' \quad (5.12)$$

That an isolated roughness flow is obtained in the low roughness density case is substantiated by the fact that the shelter areas downwind of the roughness elements do not reach the next element (Fig. 5.2c and d; Walter et al., 2012b). The surface drag coefficient  $C_S$  was determined using Eq. (5.2) and the average surface shear stress  $\tau_s$  measured with thirty-two Irwin sensors for the smooth-floor case. This method used to determine  $C_R$  and  $C_S$ , however, does not check the full momentum balance as investigated by Marshall (1971) but results in reasonable values for the drag coefficients as will be shown later.

Fig. 5.3 shows the drag coefficients for the plant and the block cases. In the plant case, three different values for  $C_R$  and  $C_S$  were determined at the free stream velocities  $U_\delta = 8, 12$  and  $16 \text{ m s}^{-1}$  showing the influence of the plants ability to streamline with the flow resulting in slightly smaller plant drag coefficients  $C_R$  at higher roughness element Reynolds numbers  $Re_h = U_h h / \nu$ . Here,  $\nu$  is the kinematic viscosity of air. This  $C_R(Re_h)$  dependency is similar to that of fountain grass as found by Gillies et al. (2002), although their drag coefficients are larger most likely because of more voluminous plants. The drag coefficient  $C_R$  in the block case is



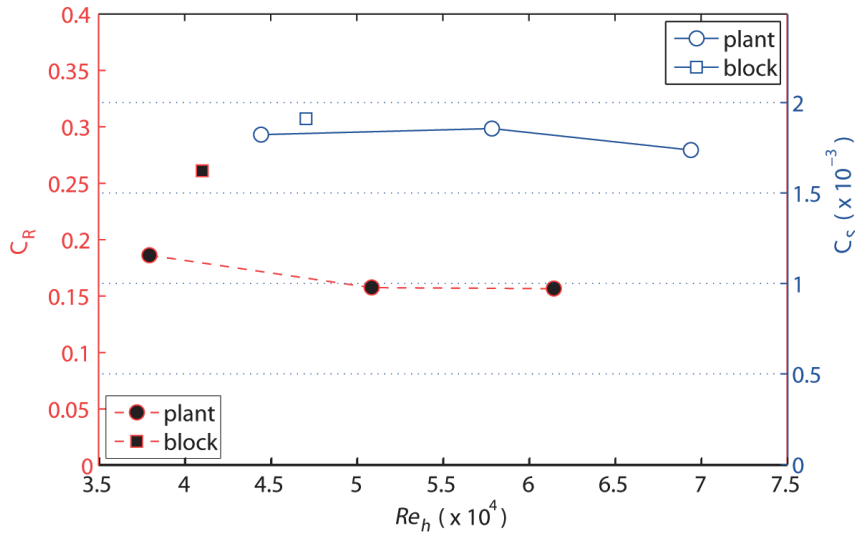


Fig. 5.3: Roughness element drag coefficient  $C_R$  and surface drag coefficient  $C_S$  for the plant case (as a function of the Reynolds number  $Re_h$ ) and the block case (at  $U_\delta = 12 \text{ m s}^{-1}$ ).

about 35% greater than in the plant case which can be explained by the rigid and non-porous shape of the block and suggests a greater flow resistance for the blocks than for the plants. The surface drag coefficient  $C_S$  for the plants remains constant ( $C_S \approx 0.0018$ ) at higher wind velocities suggesting Reynolds number independency. Note the different scaling for  $C_R$  (left side ordinate) and  $C_S$  (right side ordinate) in Fig. 5.3. The surface drag coefficient  $C_S = 0.0019$  determined for the block case is slightly higher compared to the plant case because the height and thus the wind velocity  $U_h$  are slightly higher for the plant than for the block (Eq. (5.2)). The roughness lengths of the wooden substrate surface is of the order of magnitude of  $z_0 = 0.01 \text{ mm}$  and was determined by fitting the logarithmic law to the mean velocity profile  $u(z)$  measured with the two component hot-film anemometer. Combining Eq. (5.2) with the logarithmic law allows the determination of the surface drag coefficient  $C_S$ . The resulting drag coefficient is  $C_S = 0.0017$  (with  $z_0 = 0.01 \text{ mm}$ ) for the plant case which agrees very well with the drag coefficients from Fig. 5.3. To obtain the roughness density  $\lambda$ , the frontal area  $A_f$  of the plants was determined by digital image analysis of front view pictures of the plants at different wind velocities (Walter et al., 2012b). This analysis shows a decrease in  $A_f$  and thus in  $\lambda$  for higher wind velocities for each density case (Appendix). For the remaining parameter  $c$  (Eq. (5.7)), Raupach (1992) suggested a constant of proportionality of  $O(1)$  and used  $c = 0.25, 0.5$  and  $1$  for his plots to illustrate the influence of  $c$  on the total stress prediction.

Fig. 5.4a shows the normalized friction velocity  $u_* / U_h = (\tau / \rho U_h^2)^{1/2}$  for our plant and block canopies against the roughness density  $\lambda$  together with literature data taken from Raupach (1992) and Raupach's model (Eq. (5.7)). The block data agrees well with the literature data for cubes, cylinders and different vegetation canopies validating our measurements. It needs to be mentioned that the data for the different roughness elements from the literature do not overlap at different  $\lambda$ -ranges. This inhibits a clear identification of roughness element shape, porosity or flexibility effects on the total stress generation. Because of the limited data available, Raupach (1992) used generalized drag coefficients  $C_R = 0.3$  and  $C_S = 0.003$  for all three kinds of roughness elements to apply the model (Eq. (5.7)). Although



the model of Raupach fits the literature data and our block data satisfactorily well, the fact that our  $C_R$  values for the plants do not agree with the generalized value of  $C_R = 0.30$  assumed by Raupach (1992) results in a poor agreement of the model with our plant data (Fig. 5.4a). Furthermore, the range of possible values for  $c$  defined in Raupach (1992) still remained relatively large between  $0.25 < c < 1$ .

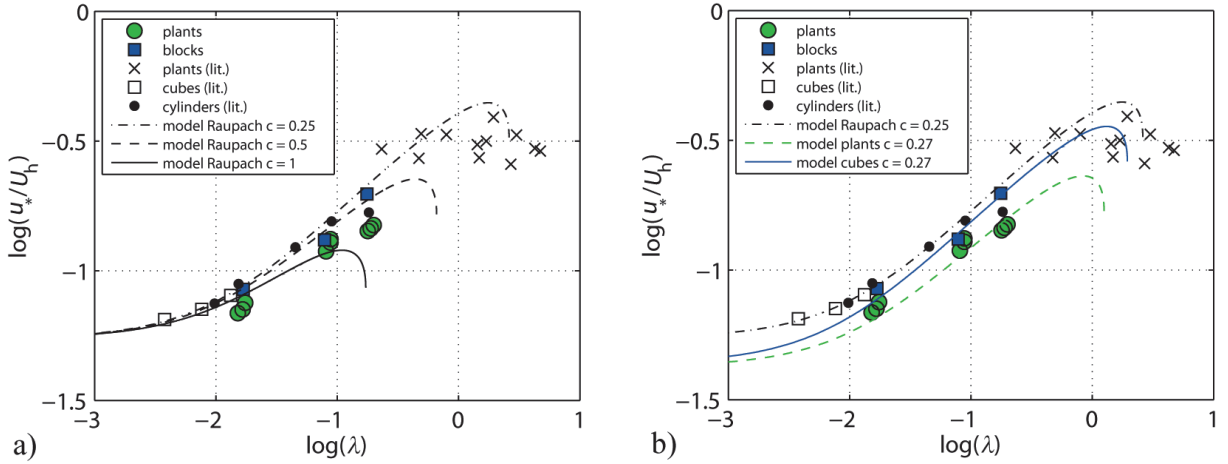


Fig. 5.4: Normalized friction velocity  $u_*/U_h$  as a function of the roughness density  $\lambda$  for the plant and block case together with literature data and the model of Raupach (1992): a) using the original model parameters  $C_R = 0.3$ ,  $C_S = 0.003$  and  $c$  from Raupach (1992) and b) using individually determined drag coefficients:  $C_R = 0.166$  and  $C_S = 0.0018$  for the plants and  $C_R = 0.261$  and  $C_S = 0.0019$  for the blocks.  $c = 0.27$  has been chosen for both the plant and the block case for better comparison.

An improved agreement of the model with our plant and block data was found when using the individual drag coefficients  $C_R$  and  $C_S$  from Fig. 5.3 (Fig. 5.4b). A  $Re_h$ -averaged  $C_R$ -value ( $C_R = 0.166$ ) was used in the plant case to obtain a clearer picture. This is justified because the measurement inaccuracies in  $u_*/U_h$  and  $\lambda$  are larger than the changes of the model prediction when implementing a Reynolds number dependent drag coefficient  $C_R(Re_h)$  for the plants (not shown here). The model is able to predict the difference in total stress generation between the two different kinds of roughness elements correctly. Here, the parameter  $c$  was used as an independent best fit-parameter where  $c = 0.29 \pm 0.03$  was found for the plants and  $c = 0.25 \pm 0.04$  for the blocks. All errors presented here are given as one standard deviation. This suggests that the constants of proportionality  $c_1 = c_2 = c$  of Raupach's model, which connect the size of the effective shelter area and volume to the flow parameters  $U_h$  and  $u_*$  (Eq. (5.3) and (5.4)), can be given a value of about  $c = 0.27$ . This value of  $c = 0.27$  was used for the model in Fig. 5.4b to achieve a better qualitative comparison.

## 5.4.2 Shear Stress Partitioning

In this section, a straightforward application of Raupach's stress ratio prediction model (Eq. (5.9) and (5.11)) to our plant and block measurements using model parameters a priori determined according to their definition is presented. Earlier studies (e.g., Marshall 1971 and Brown et al., 2008) applied Raupach's model to solely one kind of roughness elements. However, since the model contains up to four parameters it can be tuned to fit any data well if one or more of those parameters are reasonably adjusted. The following analyses show that

the model is capable of predicting the differences in stress ratio for different roughness elements correctly when using the independently determined model parameters.

#### 5.4.2.1 Average Stress Ratio

The average shear stress  $\tau_S'$  on the exposed surface area  $S'$  beneath a canopy is an important measure to estimate the overall sheltering capability of non-erodible roughness elements. Fig. 5.5 shows the average stress ratio  $(\tau_S'/\tau)^{1/2}$  for the plant and the block experiments as a function of the roughness density  $\lambda$  together with literature values from similar studies (Marshall 1971; Lyles and Allison 1975; Crawley and Nickling 2003). Despite a good overall agreement of our data with the literature values, significant differences were found between the stress ratios of the plants and the blocks at a constant roughness density  $\lambda$ . Furthermore, the blocks provide the lower stress ratio at low roughness densities relative to the plants. This changes for the high roughness density case where the plants provide the lower stress ratios relative to the blocks. The different free stream velocities  $U_\delta = 8, 12$  and  $16 \text{ m s}^{-1}$  in the plant case result in three different data points for each canopy density in Fig. 5.5. Note that the slightly lower roughness densities  $\lambda$  at higher free stream velocities  $U_\delta$  are a result of the decreased frontal areas  $A_f$  of the plants (Appendix). This results in higher flow velocities close to the ground and higher surface shear forces with slightly higher average stress ratios  $(\tau_S'/\tau)^{1/2}$ .

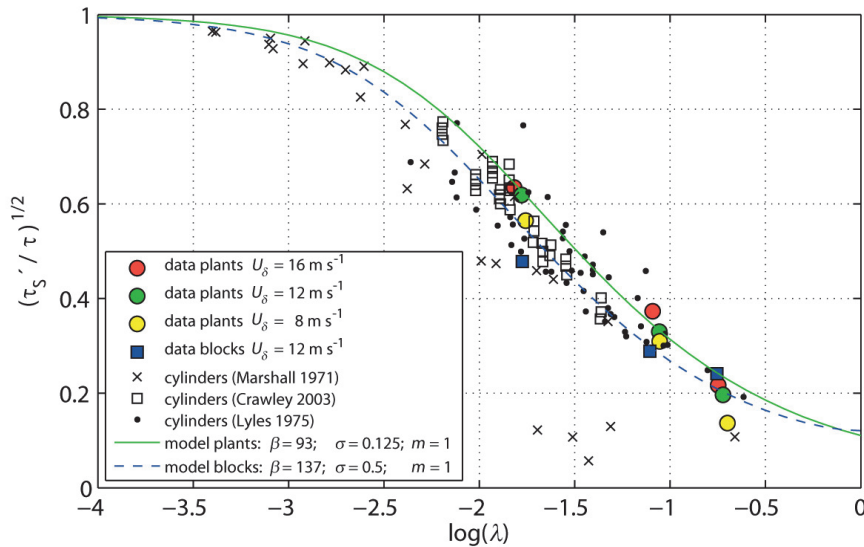


Fig. 5.5: Average surface shear stress ratio  $(\tau_S'/\tau)^{1/2}$  as a function of the roughness density  $\lambda$ . Measurement and literature data together with a straight forward application of Raupach's model using model parameters determined according to their definition.

Parameters  $\sigma$  and  $\beta$ , determined a priori from their definition were used to assess the performance of Raupach's model (Eq. (5.9)) in predicting the stress ratio  $(\tau_S'/\tau)^{1/2}$  (Fig. 5.5). The basal to frontal area index  $\sigma$  is  $\sigma = 0.5$  in case of the blocks and was estimated as  $\sigma \approx 0.125$  in case of the plants. Because the plants streamline with the flow,  $\sigma$  slightly increases by about 30% for higher wind velocities. However,  $\sigma$  significantly impacts the stress partition prediction only at roughness densities higher than our high-density case ( $\lambda > 0.2$ ) (Raupach et al., 1993). The value of  $\sigma = 0.125$  for the plants has thus been used for any calculation

presented in this study. The parameter  $\beta = C_R/C_S$  was calculated using the values from the previous section (Fig. 5.3) and is  $\beta = 137$  for the blocks and  $\beta = 93$  for the plants when using again a  $Re_h$ -averaged  $C_R$ -value for the plants, for the same reasons as before. For comparison, the model has been applied with  $\beta$  as an independent least-square fit parameter where  $\beta = 167 \pm 67$  was found for the blocks and  $\beta = 107 \pm 10$  for the plants. These values are both about 15% larger than the independently determined values from the previous section, which can be explained by the influence of the isolated roughness flow that seems to result in a slight under-prediction of the  $\beta$ -parameter. Please note that the correct determination of  $C_R$  strictly requires a flow around a single surface-mounted roughness element.

Fig. 5.5 shows that the model is able to predict the general difference between the two different roughness elements for low  $\lambda$  and supports the statement of Raupach (1992) that the shear stress ratio is fully controlled by the  $\beta$ -parameter. However, the model does not reflect the fact that the plants provide the lower stress ratio  $(\tau_S'/\tau)^{1/2}$  for the high roughness density case ( $\lambda \approx 0.18$ ) while for the low-density case ( $\lambda \approx 0.017$ ) the blocks provide the lower stress ratio. This reversal in the sheltering effect at high roughness densities is relatively small and thus needs to be interpreted with caution. However, it is an important finding and the reversal itself as well as the reasons why it is not captured by the Raupach model can be explained:

First, the Raupach model is expected to become progressively worse for  $\lambda$  larger than about 0.1 - 0.3 for theoretical reasons (Shao and Yang 2008). However, the model predictions generally agree with our data even for the high-density case suggesting a limiting value for the model of  $\lambda > 0.2$ . Secondly, the model of Raupach does not account for the streamlining behaviour and the fluttering capability of the plants. The streamlining effect of the plants results in generally less flow resistance (which means an effectively smaller  $u_*$ ) compared to the blocks at the low and medium roughness density (e.g., Walter et al., 2012b). For the high-density case, the blocks result in a skimming flow regime with a reduced flow resistance (smaller  $u_*$ ) compared to the medium-density block case (Walter et al., 2012b). This supports the above assumption that our high-density block case might fall within the range where Raupach's model starts to become invalid. This decrease in  $u_*$ , however, has not been found for the plants. The fluttering capability of the plants has the opposite effect of the streamlining behaviour in that it is able to enhance the flow resistance. This effect is strongest for the high-density plant case, because of the large amount of plants, and explains the higher total stress production (larger  $u_*$ ) relative to the high-density block case (Walter et al., 2012b). Moreover, the streamlining effect of the plants results in a higher horizontal coverage of the surface compared to the blocks and is also strongest in the high-density case. This is a specific effect resulting from our highly flexible plant species and may well be different for rigid shrubs. However, the horizontal coverage is the reason why a lower average surface shear stress  $\tau_S'$  was found for the high-density plant case compared to the block case (Walter et al., 2012b). The latter effect together with the higher total stress  $\tau$  generated by the plants compared to the blocks in the high-density case explains the reversal in the stress ratios  $(\tau_S'/\tau)^{1/2}$ .

One way to implement this reversal into Raupach's model would be to introduce additional parameters to account for the horizontal coverage and the fluttering capability of the plants. However, since the model already contains parameters that are still relatively unspecified and difficult to determine for various canopies, an inclusion of additional

parameters was rejected for this work. The above discussion points out that characteristics like the porosity, the flexibility and the shape of the roughness elements can have complex influence on the stress partition and its dependency on  $\lambda$ . Accordingly, results based on measurements using rigid and non-porous plant imitations have to be considered cautiously when estimating the shelter capability of live plant canopies.

#### 5.4.2.2 Peak Stress Ratio

Fig. 5.6 shows the peak surface shear stress ratio  $(\tau_S''/\tau)^{1/2}$  as a function of  $\lambda$  for the plant and the block experiments together with literature data and the results from the Raupach model (Eq. (5.11)) applied to our data. An overall agreement of our data with the relative widely spread ensemble of literature data is obtained. Interestingly, our plant and block peak stress ratios  $(\tau_S''/\tau)^{1/2}$  are fairly similar for the different roughness densities, at least for the low and the medium-density case. This can be explained as follows: The rigid and non-porous blocks result in a stronger flow deflection around their body compared to the flexible and porous plants. Hence, the higher wind velocities in the speed up zones at both sides of the blocks result in higher peak surface shear stress values  $\tau_S''$  relative to the plants. However, the stronger flow deflection in the block case also causes higher flow resistance and thus a higher total stress  $\tau$  on the entire block array compared to the plant canopy. This suggests that peak surface shear stress ratios  $(\tau_S''/\tau)^{1/2}$  obtained by measurements using rigid and non-porous plant imitations can be quite similar to those for real vegetation canopies. Thus, artificial plant imitations might satisfactorily represent real canopies considering investigations of the peak stress ratio  $(\tau_S''/\tau)^{1/2}$ . Nevertheless, the spatial distributions and the absolute values of  $\tau_S(x, y)$  can be very different for canopies with plant imitations such as rigid and non-porous obstacles compared to live plant canopies (Walter et al., 2012b). The same reversal in the sheltering effect from low to high roughness densities as found for the average stress ratio was found for the peak stress ratio and can be made plausible with similar arguments as discussed in the previous section.

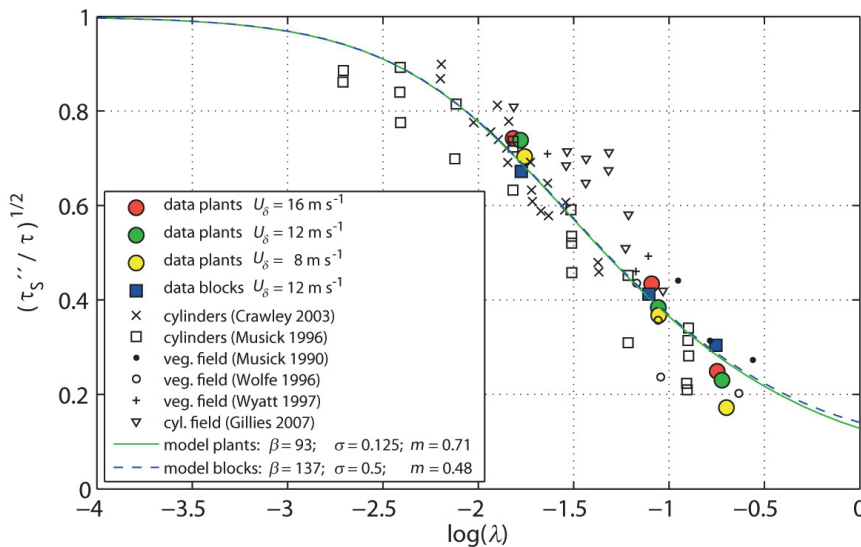


Fig. 5.6: Peak surface shear stress ratio  $(\tau_S''/\tau)^{1/2}$  as a function of the roughness density  $\lambda$ . Measurement and literature data together with a best fit application of Raupach's model with  $m$  as the independent fit parameter.

The application of the Raupach model (Eq. (5.11)) with  $m$  as an independent least-square fit parameter results in  $m = 0.48 \pm 0.07$  ( $R^2 = 0.991$ ) for the blocks and  $m = 0.71 \pm 0.08$  ( $R^2 = 0.957$ ) for the plants. Wyatt and Nickling (1997) found  $m = 0.16$  for sparse desert creosote communities in field experiments which is a relatively small value compared to the findings of other studies where  $0.4 < m < 0.6$  was found for cylinders or blocks (e.g., Crawley and Nickling 2003; Brown et al. 2008). Crawley and Nickling (2003) explained this difference as an effect of flow dynamics influenced by porous roughness elements. However, our data suggests that the blocks produce higher peak and lower average surface shear stresses than the plants due to the stronger flow deflection around the blocks for the low and the medium-density case. This in turn implies that the  $m$ -value, according to its definition  $\tau_S''(\lambda) = \tau_S'(m\lambda)$  has to be smaller for blocks than for plants as observed in our study. However, a direct comparison is difficult since Wyatt and Nickling (1997) used fairly different plants (*creosote bushes*) with a high porosity and low flexibility whereas the plants used in this study (*ryegrass*) have a high flexibility and a relatively low porosity.

### 5.4.3 The $m$ -parameter

A similar approach as presented by Crawley and Nickling (2003) has been used to determine the  $m$ -parameter according to its definition (Eq. (5.10)). Therefore, in a first step, the peak  $\tau_S''$  and the average  $\tau_S'$  surface shear stresses were plotted against the roughness density  $\lambda$  for a free stream velocity  $U_\delta = 16 \text{ m s}^{-1}$  and logarithmic regression relations were applied (Fig. 5.7):

$$\tau_S' = a_1 \cdot \ln(\lambda) + b_1 \quad (5.13a)$$

$$\tau_S'' = a_2 \cdot \ln(\lambda) + b_2 \quad (5.13b)$$

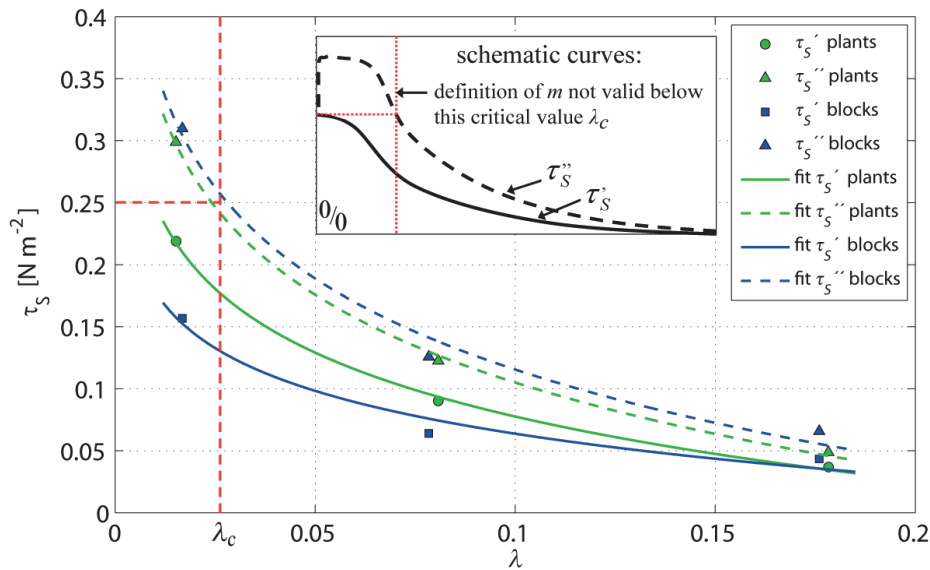


Fig. 5.7: Peak  $\tau_S''$  and average  $\tau_S'$  surface shear stress data as a function of the roughness density  $\lambda$  for the plant and the block experiments at  $U_\delta = 16 \text{ m s}^{-1}$ . Logarithmic regression relations (Eq.13) were applied to the data. Schematic curves are shown in the upper box to visualize the assumed behavior of  $\tau_S''$  and  $\tau_S'$  outside the measurement range.



The independent least-square fit parameters are  $a_1 = -0.074 \text{ N m}^{-2}$  and  $b_1 = -0.094 \text{ N m}^{-2}$  ( $R^2 = 0.999$ ) and  $a_2 = -0.102 \text{ N m}^{-2}$  and  $b_2 = -0.130 \text{ N m}^{-2}$  ( $R^2 = 0.999$ ) for the plant case. Identical analyses were made for  $U_\delta = 8$  and  $12 \text{ m s}^{-1}$  (not shown here) to identify the dependency of the  $m$ -parameter on the wind velocity or the Reynolds number  $Re_h$ , respectively. Logarithmic regression relations (Eq. (5.13)) were used by Crawley and Nickling (2003) because of both a good fit and the convergence of  $\tau_S''$  and  $\tau_S'$  for small ( $\lambda \rightarrow 0$ ) and large ( $\lambda \rightarrow 1$ ) roughness densities. These relations satisfactorily represent the dependency of  $\tau_S''$  and  $\tau_S'$  on  $\lambda$  within the measurement range  $0.015 < \lambda < 0.18$  (Fig. 5.7).

Schematic curves are shown in the upper box in Fig. 5.7 to visualize the expected dependency of  $\tau_S''$  and  $\tau_S'$  on  $\lambda$  outside the measurement range for our kind of roughness elements. For both the plant and the block experiment,  $\tau_S'$  converges against a constant value of  $\tau_S' = 0.25 \text{ N m}^{-2}$  for  $\lambda \rightarrow 0$ , which was measured for the smooth-floor case at a free stream velocity of  $U_\delta = 16 \text{ m s}^{-1}$ . Below a critical roughness density  $\lambda_c$ ,  $\tau_S''$  is expected to be larger than any  $\tau_S'$  at  $\lambda < \lambda_c$ , so the parameter definition for  $m$  (Eq. (5.11)) is not valid below  $\lambda_c$  (schematic curves in Fig. 5.7). Just as the last roughness element on a large unit ground area  $S$  is removed to achieve a roughness density  $\lambda = 0$ , a point of discontinuity occurs and  $\tau_S'' = \tau_S'$ . When decreasing the roughness element size to achieve lower roughness densities  $\lambda$ , the point of discontinuity vanishes and  $\tau_S''$  decreases steadily until it reaches  $\tau_S'$  for  $\lambda = 0$ .

The peak surface shear stress  $\tau_S''$  can be even larger than the total stress  $\tau$  at very low  $\lambda$  considering widely spaced roughness elements on a surface with a strong deflection of the air flow resulting in locally very high wind velocities close to the ground in the speed up zones. This is in conflict with the order suggested by Raupach et al. (1993) that  $\tau_S < \tau_S' < \tau_S'' < \tau$ , however, he already mentioned that assuming  $\tau_S'' < \tau$  is a rather speculative assumption due to the lack of available data. That  $\tau_S''$  can be larger than  $\tau$  results in enhanced erosion by the roughness elements at low canopy densities as validated e.g. by Burri et al. (2011b).

For high roughness densities  $\lambda$ , both  $\tau_S''$  and  $\tau_S'$  converge to zero (schematic curves in Fig. 5.7). This is obtained by the fact that  $\ln(\lambda \rightarrow 1) = 0$  in Eq. (5.13) although the parameter  $b_i$  is needed to obtain reasonable fits. However, the values for  $a_i$  and  $b_i$  from the fits are all slightly smaller than zero permitting  $\tau_S'$  and  $\tau_S''$  becoming zero for  $\lambda < 1$ . This is in agreement with literature results which suggest completely sheltered surfaces already for  $\lambda > 0.3$  (e.g., Raupach 1992).

In a second step, an iterative comparison of  $\tau_S''$  with  $\tau_S'$  from Fig. 5.7 over the entire  $\lambda$ -range was carried out to evaluate Eq. (5.10) and to obtain the dependency of the  $m$ -parameter on the roughness density  $\lambda$  (Fig. 5.8). This was done for the free stream velocities  $U_\delta = 8, 12$  and  $16 \text{ m s}^{-1}$  and for both the plant and the block experiments. The  $m(\lambda)$ -curve determined by Crawley and Nickling (2003) for solid cylinders at a free stream velocity of  $U_\delta = 17.07 \text{ m s}^{-1}$  is included as well for  $\lambda < 0.0434$  which was the upper limit of their measurement range. Crawley and Nickling (2003) used different sizes of solid cylinders to obtain different roughness densities  $\lambda$ . As indicated in Fig. 5.8, Crawley's logarithmic regression relations result in  $m(\lambda)$  converging against 1 for  $\lambda \rightarrow 0$  as it should be when reducing the roughness density  $\lambda$  by decreasing not just the amount of roughness elements per unit area but also the roughness element size. Contrary, in our case and as mentioned before,  $\tau_S'$  converges against our constant "smooth-floor" limit-value of  $\tau_S' = 0.25 \text{ N m}^{-2}$  for small roughness densities, while  $\tau_S''$  values significantly larger than  $\tau_S'$  occur. This means that



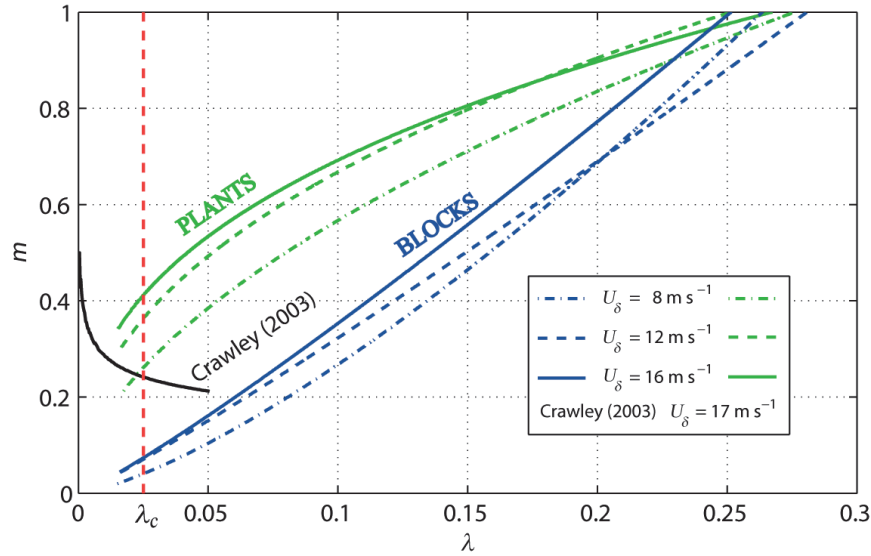


Fig. 5.8: Parameter  $m$  as a function of the roughness density  $\lambda$  and  $U_\delta$  for the plant and the block case. The curve from Crawley and Nickling (2003) for wooden cylinders is included as well. Our data are incorrect below  $\lambda_c \approx 0.025$  (dotted line) because the definition for  $m$  is not valid below (see also Fig. 5.7).

below the critical value  $\lambda_c$  there is no corresponding  $\tau_S'(m\lambda)$  to determine  $\tau_S''(\lambda)$  according to Eq. (5.10) (schematic curves in Fig. 5.7). As a result, our  $m(\lambda)$  curves are incorrect below  $\lambda_c \approx 0.025$  (red dotted line in Fig. 5.8) which is larger than the lower limit of our measurement range ( $\lambda = 0.017$ ). However, for the sake of completeness, the  $m$ -values have been plotted down to  $\lambda = 0.017$ .

When predicting  $m(\lambda)$  for larger roughness densities outside the measurement range ( $\lambda > 0.18$ ), the fact that  $\tau_S''$  and  $\tau_S'$  converge against zero and both become zero for a completely sheltered surface means that  $m$  has to converge against one. Our  $m(\lambda)$ -curves in Fig. 5.8 suggest that in both the plant and the block cases and for all free stream velocities  $U_\delta$ , the surface becomes completely sheltered at a roughness density of  $\lambda \approx 0.25$ , i.e. when  $m = 1$ . This agrees with results presented by Raupach (1992) who found completely sheltered surfaces for  $\lambda > 0.3$ . Strictly, the  $m(\lambda)$  curves should asymptotically converge against  $m = 1$  and not cross it like in our case. However, this can be explained by the limited measurement accuracy as well as the limitations of the logarithmic regression relations from Eq. (5.13).

When averaging the  $m$ -values from Fig. 5.8 over the measured  $\lambda$ -range, the average values for the plants are  $m = 0.63, 0.69, 0.70$  and for the blocks  $m = 0.37, 0.40, 0.44$  for the free stream velocities  $U_\delta = 8, 12$  and  $16 \text{ m s}^{-1}$ . These values agree quite well with the  $m$ -values obtained by the least-square fit method given in Fig. 5.6 where  $m = 0.71$  was found for the plants and  $m = 0.48$  for the blocks. When using the least-square fit  $\beta$ -values ( $\beta = 107$  and  $167$  for the plants and the blocks as presented in Section 5.4.2.1) to obtain least-square fit  $m$ -values, the values are  $m = 0.61$  for the plants and  $m = 0.39$  for the blocks.

Fig. 5.8 shows that  $m$  is a function of  $U_\delta$  or the Reynolds number  $Re_h$ , the roughness density  $\lambda$  and the roughness element shape (see also Crawley and Nickling 2003; Brown et al., 2008). Crawley and Nickling (2003) found that the model strongly overestimates the shear stress ratio  $(\tau_S''/\tau)^{1/2}$  when using their  $\lambda$ -dependent  $m$ -parameter. Fig. 5.9 shows the modelled against the measured stress ratios first when using the constant least-square fit  $m$ -parameters from Fig. 5.6 ( $m = 0.71$  and  $m = 0.48$ ) and second when using  $m = m(Re_h, \lambda, \text{shape})$  from Fig.

5.8 for the model. An overall better agreement is found for the constant  $m$ -parameter whereas the modelled data points in the high-density plant case, i.e. for the lowest stress ratios, slightly improve when using  $m = m(Re_h, \lambda, \text{shape})$ . For the medium roughness density, only the block data point deteriorates and in the low-density case, i.e. for the highest shear stress ratios, all modelled values deteriorate when using  $m = m(Re_h, \lambda, \text{shape})$ . The latter can be explained by the fact that the  $m(Re_h, \lambda, \text{shape})$  values become physically not meaningful below  $\lambda < \lambda_c$  because of the limitations of Eq. 10 at low roughness densities as discussed earlier in this section (Fig. 5.7 and Fig. 5.8). This suggests that an improvement of the predictability of Raupach's model can be accomplished when using  $m(Re_h, \lambda, \text{shape})$ , at least for medium and high-density canopies. However, determining  $m(Re_h, \lambda, \text{shape})$  using Eq. (5.10) is very difficult, time consuming and laborious suggesting that using a constant  $m$ -parameter is more practicable.

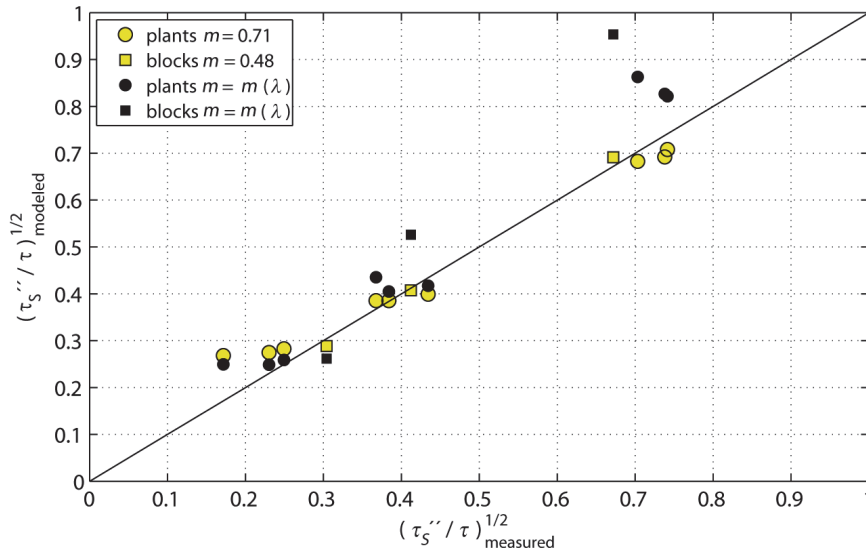


Fig. 5.9: Modelled against measured peak surface shear stress ratios  $(\tau_s''/\tau)^{1/2}$  when using a constant  $m$ -parameter and when using  $m = m(Re_h, \lambda, \text{shape})$  from Fig. 5.8.

For rigid cylinders,  $m = 0.4 - 0.5$  has been found by other studies (e.g., Brown et al., 2008) which agrees very well with our rigid block values for  $m$ . For live plants, a large variation of possible  $m$ -values ranging from  $m = 0.16$  (Wyatt and Nickling 1997) to  $m = 0.71$  (this study) has been found. The variation of the  $m$ -parameter strongly affects the applicability of the model since it is difficult to choose an appropriate  $m$ -value for a canopy of interest. To determine the  $m$ -parameter for a specific type of roughness elements, a very time consuming series of measurements at different roughness densities is required to obtain the constant  $m$ - or the non constant  $m(Re_h, \lambda, \text{shape})$ -parameter.

#### 5.4.4 The peak-mean stress ratio $a$

The model of Raupach becomes a useful tool if one can independently and easily determine the parameters  $\sigma$ ,  $\lambda$ ,  $\beta$ , and  $m$  to calculate the stress ratio for a certain canopy. The geometric parameters describing the roughness of the canopy, the frontal to basal area index  $\sigma$  and the roughness density  $\lambda$  are relatively easy to determine. Literature values for  $\beta = C_R/C_S$  are

available for different kinds of roughness elements (e.g., Gillies et al., 2002). Additionally,  $\beta$  can be determined by measuring the force  $\Phi$  on a single wall-mounted roughness element using a force gauge to determine  $C_R$  (Eq. (5.1)) and by measuring  $\tau_S$  in the absence of any roughness elements using an Irwin sensor or other techniques (e.g., hot-film anemometry) to determine  $C_S$  (Eq. (5.2)).

In the previous section it was shown that a large range of  $m$  has been reported ( $m = 0.16 - 0.71$ ) and that it is cumbersome to determine  $m$  from fits of shear stress ratio data (e.g., Fig. 5.6) or directly using the independent parameter definition (Eq. (5.10)). It was shown that the non-constant  $m(Re_h, \lambda, \text{shape})$ -parameter is even more difficult to determine (Fig. 5.7 and Fig. 5.8) and only improves the peak stress ratio prediction when determined with high accuracy (Fig. 5.9). Furthermore, an extensive experimental setup and high accuracy measurements of the surface shear stress distribution are required to determine  $m$  adequately. These facts show that the  $m$ -parameter according to its definition from Eq. (5.10) is rather impracticable and that there is a demand for a new, physically more solid definition to describe the relation between the peak shear stress  $\tau_S''$  and the surface average shear stress  $\tau_S'$ .

We suggest the definition of a new parameter  $a$  that linearly relates the peak shear stress  $\tau_S''$  to the surface average shear stress  $\tau_S'$  instead of using the definition  $\tau_S''(\lambda) = \tau_S'(m\lambda)$  (Eq. (5.10)):

$$\tau_S'' = a \cdot \tau_S' \quad (5.14)$$

This parameter is hereafter named the peak-mean stress ratio  $a$ . Crawley and Nickling (2003) presented a linear relationship between  $\tau_S''$  and  $\tau_S'$  independent of  $\lambda$  and  $U_\delta$ . King et al. (2006) found a linear relation between  $(\tau_S''/\tau)^{1/2}$  and  $(\tau_S'/\tau)^{1/2}$ , which means in fact the same as Eq. (5.14).

Fig. 5.10 shows  $\tau_S''$  as a function of  $\tau_S'$  for both the plant and the block experiments and for all measured roughness densities  $\lambda$ . For all cases, this relationship is independent of  $U_\delta$  and strongly linear with  $R^2 > 0.99$  in average. The strong linear dependency can be made physically plausible when considering the air flow close to the ground in-between the roughness elements. First, it is assumed that the spatiotemporally averaged wind velocity inside the canopy  $\langle U_i \rangle$  is driven by the air flow above and is linearly related to the free stream velocity  $U_\delta$ . Second, we assume that there are no large changes in the spatial surface shear stress distribution  $\tau_s(x, y)$  when increasing  $U_\delta$ , i.e. that the location of  $\tau_S''$  and the dimensions of the shelter area remain unaltered. These assumptions hold for a Reynolds number independent flow. Since the friction velocity  $u_*$  is proportional to  $U_\delta$  (neglecting effects of stratification) and so the total stress  $\tau$  is proportional to the square of the free stream velocity ( $\tau \sim U_\delta^2$ ), it can be assumed that the local surface shear stress  $\tau_s(x, y)$  scales with  $\langle U_i \rangle^2$  and thus with  $U_\delta^2$ . Therefore, the peak and the average surface shear stress  $\tau_S''$  and  $\tau_S'$  are assumed to be proportional to the square of the free stream velocity according to:

$$\tau_S' = c' \cdot U_\delta^2 \quad (5.15a)$$

$$\tau_S'' = c'' \cdot U_\delta^2 \quad (5.15b)$$

Here,  $c'$  and  $c''$  are constants of proportionality. This finally results in  $\tau_S''/\tau_S' = c''/c' = a = \text{constant}$  as defined in Eq. (5.14) and substantiated by Fig. 5.10.

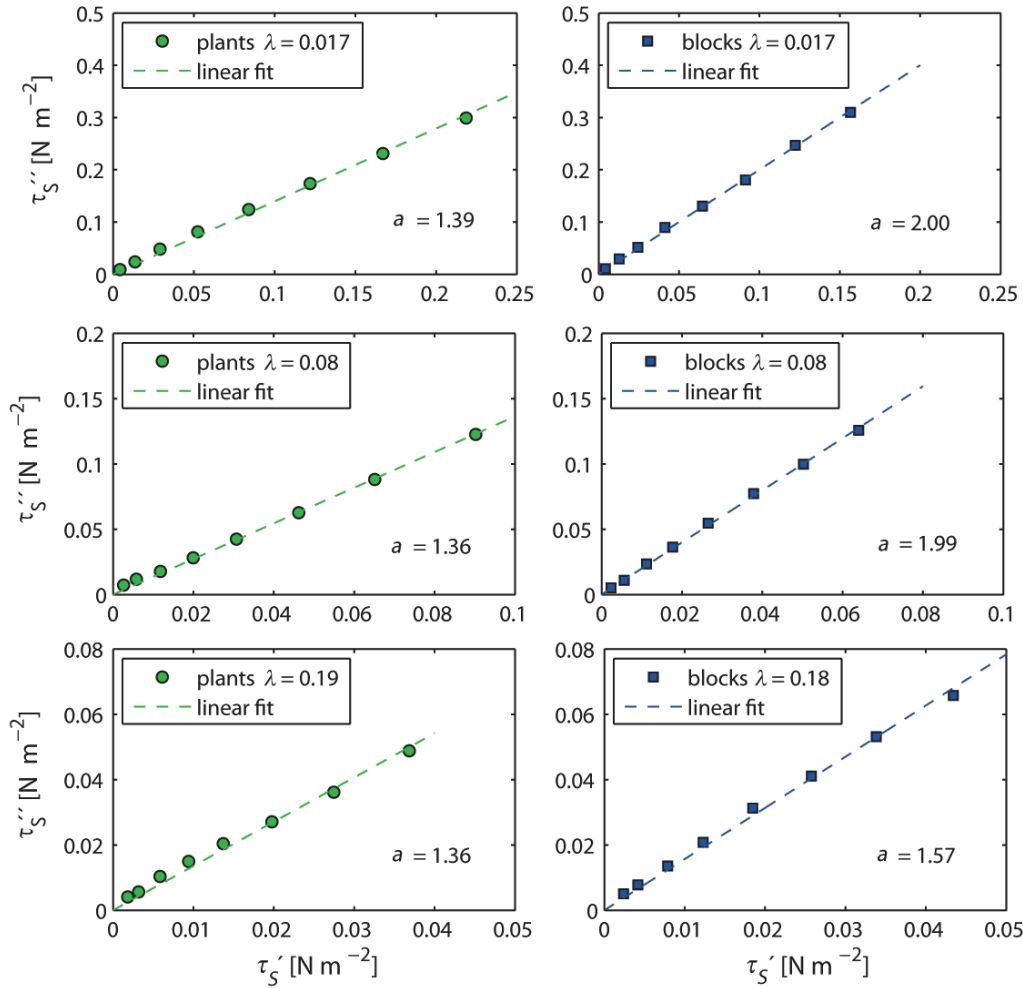


Fig. 5.10: Peak surface shear stress  $\tau_S''$  as a function of the average surface shear stress  $\tau_S'$  for the plant and the block experiments and for different roughness densities  $\lambda$ . The eight data points in each plot correspond to free stream velocities  $U_\delta = 2 - 16 \text{ m s}^{-1}$ .

Further, the peak-mean stress ratio  $a$  remains approximately constant for different roughness densities with  $a = 1.39 \pm 0.02$ ,  $1.36 \pm 0.02$  and  $1.36 \pm 0.04$  for the low-, the medium- and the high-density plant case. For the blocks,  $a$  is constant for the low- and the medium-density case with  $a = 2.00 \pm 0.02$  and  $1.99 \pm 0.02$  and decreases for the high-density case to  $a = 1.57 \pm 0.03$ . This suggests that for sparse canopies (e.g. our low- and medium-density cases) with isolated roughness and wake interference flows (Walter et al., 2012b), the strength of the deflection of the air flow around the roughness element and the sizes of the resulting eddies shed by the obstacles is independent of the inter roughness element spacing and thus  $\lambda$ . The medium-density cases are examples of wake interference flow because the sheltered areas reach the next roughness element downstream while a significant fraction of the surface remains unsheltered (Walter et al., 2012b). The lower value of  $a = 1.57$  found for the high-density block case suggests that this is no longer true for high roughness densities with a skimming flow regime. This can be explained by the smaller eddies shed due to the influence of the neighbouring obstacles, which limit the space in between the roughness elements. The fact that this is not the case for the high-density plant case and  $a$  is still the same as for the low and the medium-density case is attributed to the fact that the eddies shed by grass swards of the plants in our case are relatively small compared to the inter roughness element spacing

even for the high-density case. This hypothesis is supported by the findings from Walter et al. (2012b) that no large horseshoe vortices develop in the plant case. To summarize, the data suggests that for live vegetation canopies the peak-mean stress ratio  $a$  (Eq. (5.14)) is independent of  $\lambda$  and  $U_\delta$  or  $Re_h$  respectively, and that  $a$  only depends on the roughness element shape itself:  $a = a(\text{shape})$ . This is a big advantage compared to the  $m$ -parameter, which depends on  $\lambda$ ,  $Re_h$  and the shape as shown in Section 5.4.3. Consequently,  $a$  is easier to determine for different vegetation species than  $m$ . The fact that  $a$  is independent of  $Re_h$  seems to be implausible when considering the high flexibility of our plants that streamline with the flow at higher wind velocities. However, this can be explained by the plants fluttering motion of the upper part of the plants and the rather non flexible stems of the lower part of the plants. A discussion on that can be found in the Appendix.

Finally it needs to be shown how well the definition  $\tau_s'' = a \tau_s'$  (Eq. (5.14)) works when combined with Eq. (5.9) to predict the peak stress ratio according to:

$$\left(\frac{\tau_s''}{\tau}\right)^{1/2} = \left(\frac{a}{(1-\sigma\lambda)(1+\beta\lambda)}\right)^{1/2} \quad (5.16)$$

Fig. 5.11 contains the same data set as Fig. 5.6 but now with the modified model of Raupach (Eq. (5.16)) applied to our data. The modified model provides a fit to the data as well as the old model using the constant  $m$ -parameter within the measurement range. For very low roughness densities ( $\log(\lambda) < -2$ ) the modified model seems to overestimate the general trend of the literature data, however, only the cylinder data from Musick et al. (1996) are noticeably lower than the prediction, which is the case for the whole  $\lambda$ -range. We attribute this to the method they deployed to determine the shear stress ratio, which has been done visually at the onset of particle erosion.

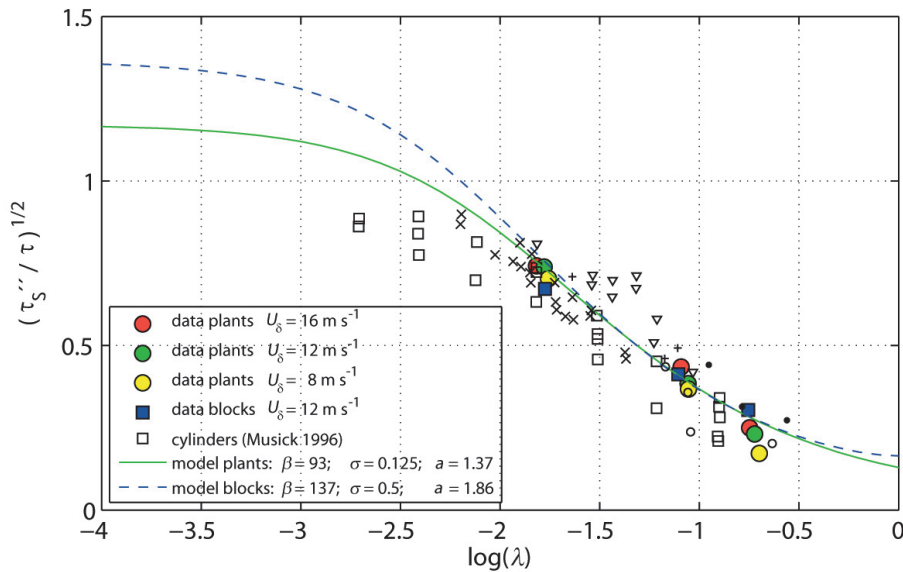


Fig. 5.11: Peak surface shear stress ratio  $(\tau_s''/\tau)^{1/2}$  as a function of the roughness density  $\lambda$  (same data as in Fig. 5.6). Measurement and literature data together with the modified model of Raupach from Eq. (5.16) which includes the new parameter  $a$  with values determined using its definition from Eq. (5.14).

The modified model results in stress ratio predictions larger than one at very low roughness densities  $\lambda < 0.005$  ( $\log(\lambda) < -2.25$ ) which means that  $\tau_S'' > \tau$  (Fig. 5.11). At a first glance, this seems to be unphysical, since  $\tau_S'' = \tau_S' = \tau$  has to hold for  $\lambda = 0$ . However, it was already discussed in Section 5.4.3 that  $\tau_S''$  may be larger than  $\tau$  at very low roughness densities. Therefore, the low roughness densities need to be realized by decreasing the number of roughness elements per unit area rather than by decreasing the roughness element size, to keep the strength of the deflection of the air flow around each obstacle constant. A single, relatively large roughness element of the size of a plant or a block as used in our experiments on a large unit ground area might thus result in a high peak shear stress  $\tau_S'' > \tau$ . At the same time, the few remaining roughness elements do not result in a strong increase in the total stress  $\tau$  above the canopy compared to the smooth-floor case. With these assumptions, it is physically plausible that  $(\tau_S''/\tau)^{1/2} > 1$  for low  $\lambda$ , furthermore,  $(\tau_S''/\tau)^{1/2} \rightarrow a^{1/2} = (\tau_S''/\tau_S')^{1/2}$  as  $\lambda \rightarrow 0$  since  $\tau_S'$  is the same as the total stress  $\tau$  in the smooth-floor case.

The latter allows for estimating the parameter  $a$  for roughness elements by using solely a single element and a single surface shear stress sensor. First, the sensor is placed in the centre of the wind tunnel to measure the total stress  $\tau$ , which is the same as the surface averaged stress in the smooth-floor case  $\tau_S'$  assuming a horizontally homogenous boundary-layer. Second, the roughness element is placed close to the shear stress sensor, so that the sensor is in the speed up zone at the position where the peak surface shear stress  $\tau_S''$  is present. To check if the position of  $\tau_S''$  is measured correctly, the roughness element can be moved slightly until the correct position of  $\tau_S''$  is found. Fig. 5.2c and d show the locations of the speed up zones for our low-density plant and block case. This procedure has been tested and as a result,  $a = 1.49$  has been determined for a single live plant slightly larger than those used for the canopy experiments. The slightly larger plant results in a stronger deflection of the air flow around and thus in higher wind velocities in the speed up zones. This in turn results in a slightly larger  $\tau_S''$  and  $a$ -value compared to the canopy measurements where  $a = 1.37$  was found. Additionally, the limited spatial measurement resolution in the canopy case potentially results in a slight underestimation of  $\tau_S''$  and thus  $a$ . The  $a$ -parameter has also been determined for a circular cylinder (diameter = 50 mm, height = 90 mm) where  $a = 2.12$  and for a block (width  $\times$  depth  $\times$  height = 60  $\times$  60  $\times$  100 mm) where  $a = 2.79$  was found. The peak-mean stress ratio  $a$  can thus be seen as a value that quantifies the strength of the flow deflection around a wall-mounted obstacle. Larger values of  $a$  mean stronger flow deflection around the obstacle, which results in larger peak stress values  $\tau_S''$ .

The performance of the modified model (Eq. (5.16)) is at least equivalent to the original Raupach model (Fig. 5.12). Fig. 5.12 is analogue to Fig. 5.9, but now compares the original model (Eq. (5.11)) with a  $Re_h$ - and  $\lambda$ -averaged constant  $m$ -parameter for the plants ( $m = 0.67$ ) and for the blocks ( $m = 0.40$ ) determined after Eq. (5.10) (Fig. 5.8) against the new modified model (Eq. (5.16)) using an average of the independently determined  $a$ -parameters from Fig. 5.10 ( $a = 1.37$  for the plants and  $a = 1.86$  for the blocks). The essential benefit of using the  $a$ -parameter, however, is its independence of  $\lambda$  and  $Re_h$  and the relatively simple experimental setup needed to determine  $a$  for different types of roughness elements compared to the extensive setup needed to determine  $m$  accurately. Further, the definition of  $a$  is more physically based and the relationship of  $\tau_S''$  on  $\tau_S'$  as well as its independency of  $Re_h$  and  $\lambda$  can be made plausible using simple fluid dynamical arguments.



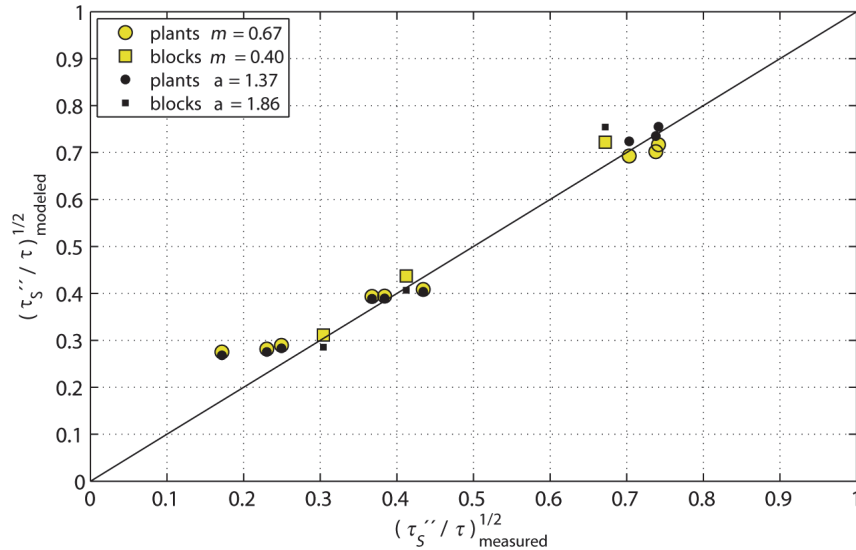


Fig. 5.12: Modelled against measured peak surface shear stress ratios  $(\tau_s''/\tau)^{1/2}$  when using the original Raupach model with a constant  $m$ -parameter and when using the new, modified model with the peak-mean stress ratio  $a$ .

A limitation of the results presented here for real erosive conditions needs to be mentioned: For natural vegetation canopies with sediment on a partially sheltered surface, spatial gradients in the surface shear stress  $\tau_s(x, y)$  result in horizontal particle transport that changes the surface topography (Raupach et al. 1993). According to this, the surface topography gets reorganized so that the spatial gradients in  $\tau_s(x, y)$  reduce and  $\tau_s''$  and  $\tau_s'$  more and more adapt to each other. Raupach et al. (1993) concluded that the  $m$ -parameter (and thus also the new  $a$ -parameter) depends on the surface morphology and changes towards one as erosion reconfigures the surface. How strong  $m$  or  $a$  change towards one for natural vegetation canopies, however, depends on additional factors like soil properties and the frequency of changes in the wind direction for example.

## 5.5 Conclusions and Outlook

Detailed investigations of the applicability and the accuracy of the model of Raupach, which predicts the ratio of the surface shear stress  $\tau_s$  to the total stress  $\tau$  above vegetation canopies of different densities, are presented. It was found that the proportionality factor  $c$  (Eq. (5.7)), which was formerly rather unspecified can be set to  $c = 0.27$  and that the model is capable of predicting the difference in total stress generation between our investigated block and plant canopies. Our plants (*ryegrass*) ability to streamline with the flow results in a lower normalized total stress  $(\tau/\rho U_h^2)^{1/2} = u_* / U_h$  generated by the plants than generated by the rigid, non-porous blocks (Fig. 5.4b).

Although Raupach's model predicts the general differences in the average shear stress ratio  $(\tau_s'/\tau)^{1/2}$  between the blocks and the plants adequately, the model does not capture the phenomenon that the blocks provide the lower stress ratios for the low roughness densities while our plant species used for the experiments provides the lower stress ratios for the high roughness densities (Fig. 5.5). Characteristics like the porosity, the flexibility and the shape of the roughness elements can have complex influence on the stress partition and its dependency

on  $\lambda$ . In the case of the peak stress ratio  $(\tau_S''/\tau)^{1/2}$ , the results for the blocks and the plants agree quite well because the blocks result in both a higher peak surface shear stress  $\tau_S''$  as well as total stress  $\tau$  compared to the plants (Fig. 5.6). This result suggests that experiments using plant imitations can be capable of representing live plant canopies quite well with respect to investigations of  $(\tau_S''/\tau)^{1/2}$ .

Moreover, it was found that the empirical model parameter  $m$ , which relates the peak  $\tau_S''$  to the average  $\tau_S'$  surface shear stress (Eq. (5.10)), is impracticably defined in Raupach's model and that a new more physically based definition in the form of  $\tau_S'' = a \tau_S'$  (Eq. (5.14)) results in model predictions of  $(\tau_S''/\tau)^{1/2}$  which are as accurate as the original formulation. The main benefit from the new definition is that  $a$  was found to be independent of the roughness density  $\lambda$  for the plants and the free stream velocity  $U_\delta$  unlike  $m$  which makes it easier to determine  $a$  than  $m$ . A method was suggested to determine  $a$  for various roughness elements by using a relatively simple experimental setup.

Although our live plant canopies partly differ from natural vegetation canopies, the fact that our plants are of similar size, trimmed to a standard height and arranged with regular spacing allowed us to systematically investigate the influence of plant flexibility and porosity on the shear stress partition. In addition, the live plant canopies used here are far closer to natural plant canopies than any roughness array used in previous wind-tunnel investigations of shear-stress partitioning and results may be similar for other plant species with comparable morphology.

Further improvements of the model may be accomplished by quantifying the increase in the horizontal coverage of the surface and the fluttering capability of flexible plants when increasing the wind velocities. The fluttering of the plants was found to result in a relatively large total stress for skimming flow regimes. Supplementary investigations may be performed to determine the parameters  $\sigma$ ,  $\beta$  and  $a$  for a range of different plant species with variations in morphology, flexibility and porosity. Such a data set can then be used by modellers and practitioners.

### Acknowledgements

We would like to thank the Vontobel foundation and the Swiss National Science Foundation (SNF) for financing this project. Thanks also to the SLF workshop and GS technology for supporting us with the development and the production of the measurement technique and the experiment setup. Thanks also to Dr. Katherine Leonard, Dr. Andrew Clifton, Dr. Katrin Burri and Benjamin Eggert for their help with the wind tunnel experiments and many fruitful discussions. Finally, we would like to thank Dr. Michael Raupach for preparing a detailed review that helped to improve the quality of this work.

## APPENDIX: $Re_h$ -independency of $a$ for plants

In section 5.4.4, it was shown that for our highly flexible plants (*ryegrass*), the peak-mean stress ratio  $a$  is independent of the free stream velocity  $U_\delta$  or the Reynolds number  $Re_h$ , respectively (Fig. 5.10). The strong linearity in  $\tau_S''(U_\delta) = a \tau_S'(U_\delta)$  (Eq. (5.14)) seems at first view to be implausible for flexible plants as for higher wind velocities, where the plants frontal area  $A_f$  and the drag coefficient  $C_R$  decrease (Fig. 5.3), a  $Re_h$ -dependence of the surface shear stress  $\tau_S$  and accordingly of  $a$  would be expected. However, there are substantive arguments that support the obtained linearity for the plants:

The spatiotemporally averaged wind velocity  $\langle U_i \rangle$  inside the plant canopy increases with  $U_\delta$  (see Section 5.4.4). The plants frontal areas  $A_f$  decrease as the plants streamline with the flow (Fig. 5.13) which in turn results in an additional slight increase of  $\langle U_i \rangle$  caused by the plants flexibility. Since now the local stress  $\tau_S(x, y)$  scales with  $\langle U_i \rangle^2$  (see Section 5.4.4),  $\tau_S''$  and  $\tau_S'$  similarly increase with  $U_\delta$  or  $\langle U_i \rangle$  and  $\tau_S'' = a \tau_S'$  holds also for flexible plants. In other words: When the plants streamline with the wind, resulting in slightly higher wind velocities close to the ground, both the peak as well as the mean surface shear stress increase similarly.

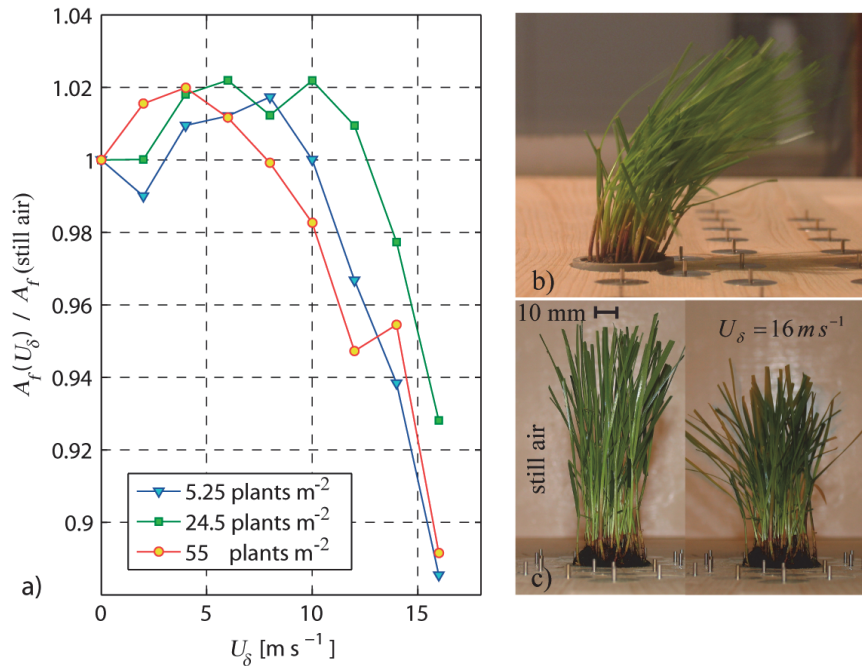


Fig. 5.13: (a) Temporally averaged frontal area  $A_f$  of the plants normalized by their still air frontal area as a function of the free stream velocity  $U_\delta$  and different canopy densities. (b) Plant (*lolium perenne*) streamlining with the flow (low-density case,  $\lambda = 0.015$ ,  $U_\delta = 16 \text{ m s}^{-1}$ ) and (c) front view pictures (streamwise direction) of a plant in still air and for  $U_\delta = 16 \text{ m s}^{-1}$  (high-density case,  $\lambda = 0.178$ ) taken from Walter et al. (2012b).

The above explanation is only true if the strength of the flow deflection around a plant remains constant at higher wind velocities, so that  $\tau_S''$  and  $\tau_S'$  increase similarly with  $\langle U_i \rangle$ . For a flexible plant with a favourable aerodynamic shape at higher wind velocities, one would expect exactly the opposite. Namely, that the strength of the flow deflection decreases for

higher wind velocities so that  $\tau_s''$  does not increase as strong as  $\tau_s'$  with  $\langle U_i \rangle$ . However, the lower parts of our plants, the stems that connect the grass swards with the ground, are relatively inflexible (Fig. 5.13b and c) which supports the finding of a velocity independent strength of the flow deflection around the plant close to the ground.

Furthermore, the flexible blades of the upper part of the plants allow the plants to respond to the turbulence in the flow. The flexible plants are very efficient in absorbing momentum of strong eddies and transforming this energy in potential energy of elastic deformation. This stored elastic energy is then released in time intervals of low turbulence and mean wind velocities, forcing the plant to re-erect to its still air shape. As a result, the time averaged frontal areas  $A_f$  do not change much with wind velocity even for our highly flexible plants (Fig. 5.13a). First,  $A_f$  increases slightly by about 2% for intermediate wind velocities (around  $U_\delta = 8 \text{ m s}^{-1}$ ) because the blades of the plants expand in the wind. Then,  $A_f$  decreases only by about 10% when increasing  $U_\delta$  from 8-16  $\text{m s}^{-1}$  (Fig. 5.13). This small decrease in  $A_f$  suggests a rather small influence of the plants flexibility on the strength of the flow deflection for different wind velocities and additionally supports the finding that  $a$  is independent of  $Re_h$ . The decrease in  $A_f$  of the plants appears to be the reason for the about 10% reduction in the drag coefficient  $C_R$  at higher wind velocities (Fig. 5.3).

## 6 Overall summary and conclusions

The main purpose of this dissertation was to improve the quantification of the sheltering effect of live vegetation against wind erosion of soil surfaces. Experiments under controlled wind tunnel conditions were performed to systematically investigate the influence of the flexibility and porosity of plants on shear stress partitioning. The four chapters presented in this thesis treat several individual topics to address this goal: (i) preliminary experiments; (ii) development of the experimental setup and the measurement technique; (iii) surface shear stress measurements in live plant canopies; (iv) application and modification of a shear stress partitioning model.

In Chapter 2 (Walter et al., 2009) the turbulent boundary-layer generated above a live vegetation canopy in the SLF wind tunnel was characterized. Spires and additional roughness elements on the fetch upwind of the test section were found to facilitate the boundary-layer development (Fig. 2.3). The adjusted ceiling allowed for flows with vanishing pressure gradients ensuring the development of turbulent boundary-layers comparable to natural atmospheric conditions (Fig. 2.3). Despite the limited dimensions of the wind tunnel and the proportionally large roughness elements in the test section, plants and blocks, the boundary-layer was found to be sufficiently developed at the measurement section. This was substantiated by the good agreement of integral length scale profiles and power spectral densities with established literature data (Fig. 2.4 and Fig. 2.5). The results revealed that the boundary-layer over live vegetation produced in the wind tunnel was well developed and suited for the experiments on shear stress partitioning.

In Chapter 3 (Walter et al., 2012a) the accuracy of the experiment setup and the measurement technique, the custom made pressure scanner and the surface shear stress sensors (Irwin sensors), were investigated. A sensor calibration procedure to determine a universal calibration function that can be applied to multiple Irwin sensors was developed. The coefficients of the universal calibration function are in excellent agreement with those originally determined by Irwin (1981), supporting the validity of both calibrations (Fig. 3.3). This finding suggests that using Irwin's original calibration function without performing any calibration of identically-built sensors can result in measurement accuracies similar to those found in this study. Tests verified that sufficiently accurate skin friction velocity distributions can be measured with the universal calibration function. Nevertheless, an intercomparison of

all sensors prior to the measurements needs to be carried out to guarantee their functionality and to reject sensors with poor agreement with the sensors used for the calibration and thus the universal calibration function. The overall accuracy of the skin friction velocity measurements averaged to about  $\pm 5\%$  for  $u_\tau > 0.13 \text{ m s}^{-1}$  and decreased strongly to  $\pm 20\%$  at lower  $u_\tau$  (Fig. 3.6). The reliability of the skin friction velocity measurements was validated by: i) the strong linear relationship between  $u_\tau$  and  $U_\delta$ , ii) the good agreement of independent  $u_\tau$ - and  $u_*$ - measurements using Irwin sensors and the two-component hot-film anemometer (Fig. 3.7) and iii) the excellent streamwise symmetry of the skin friction velocity distribution around a single wall-mounted block (Fig. 3.8a). The skin friction velocity measurements on the ground beneath a single wall mounted block can serve as high resolution validation data for CFD-models (Fig. 3.8a). Overall, Irwin sensors were found to be well suited for measuring skin friction velocity distributions with high spatial resolution, and should thus be considered as an excellent resource for application in environmental fluid mechanics studies as well as their historic use in wind comfort issues.

In Chapter 4 (Walter et al., 2012b) spatiotemporally resolved surface shear-stress variations on the ground beneath live plant canopies and rigid block arrays were presented and discussed. Four different roughness densities ( $\lambda = 0, 0.017, 0.08, 0.18$ ) were investigated at various wind velocities. A comparison between the plant and the block results revealed the influence of the plant's flexibility and porosity on the shear stress partition and the sheltering effect against wind erosion. The blocks provided a higher overall sheltering effect at the low and medium roughness densities, however, they generated higher peak shear-stress values at all roughness densities compared to the plants (Fig. 4.4 and Table 4.1). The plants streamline with the flow, resulting in a decreasing sheltering effect at higher wind velocities due to the narrower sheltered areas in their wakes (Fig. 4.4). This particularly suggests the use of plants with low flexibility for renaturation projects in areas with high wind speeds. The surface shear-stress patterns on the ground beneath the plants and blocks suggest significant differences in erosion and deposition in such canopies (Fig. 4.5). The influence of surface shear stress distributions on spatial variations in the particle mass fluxes still needs to be investigated and will provide useful information to improve the modelling of wind erosion. The peak near-ground turbulence intensities were found to be higher for the block than for the plant experiments which can be explained by the fact that the plants streamline with the flow resulting in less flow resistance and turbulence being produced (Fig. 4.6). The near surface turbulence intensity distributions support the hypothesis that horseshoe vortices are weakened or actually suppressed in the plant case. The reason for this might be a weakened flow deflection around the plant relative to the solid block. This further explains the lower peak shear stress values found for the plants than for the blocks in the speed up zones beside the roughness elements (Table 4.1). The spatial patterns of the percentage of time  $\psi$  when locally a threshold skin friction velocity is exceeded show compelling similarities to sand erosion and deposition patterns around the plants (Fig. 4.7). These findings suggest that  $\psi$  could be a useful parameter for determining local erosion and deposition rates. In general, our results demonstrate the importance of knowing the spatial and the temporal variability of the surface shear-stress to fully quantify local particle erosion. It was found that artificial plant imitations such as rigid and solid blocks or cylinders provide inadequate approximations of live plants. Results from many earlier studies using rigid roughness elements may thus have limited



application in studies of the sheltering effect of live plants on sediment transport and soil erosion in natural environments. Some limitations to the surface shear stress variations presented here compared to real erosive conditions are discussed in the following Chapter (Chapter 7).

In Chapter 5 (Walter et al., 2012c) detailed investigations of the applicability and the accuracy of Raupach's shear stress partitioning model were presented and model modifications were suggested. The model accurately predicts the difference in total stress  $\tau$  generation between the investigated block and plant canopies (Fig. 5.4b). The proportionality factor  $c$ , needed to determine the total stress and which was poorly specified prior to this study, was found to have a value of about  $c = 0.27$ . This finding suggests that  $c$  is a universal constant which is a very useful result allowing for more accurate predictions of the total stress for many rough surfaces. Although Raupach's model predicts the general differences in the average stress ratio  $\tau_S'/\tau$  between the blocks and the plants adequately, the model does not capture the phenomenon that the blocks provide the lower stress ratios for the low while the plants provide the lower stress ratios for the high roughness densities (Fig. 5.5). This shows that characteristics like the porosity, the flexibility and the shape of the roughness elements can have complex influence on the stress partition and its dependency on  $\lambda$ . Future work may incorporate additional parameters to the Raupach model to account for the plants flexibility and porosity. However, since the model already contains parameters that are still relatively unspecified and difficult to determine for various canopies, an inclusion of additional parameters was rejected for this work. The peak stress ratios  $\tau_S''/\tau$  were very similar for the plant and block cases suggesting that experiments using plant imitations can represent live plant canopies quite well in this regard (Fig. 5.6). Nevertheless, the spatial distributions and the absolute values of  $\tau_S$  can be very different for canopies with plant imitations such as rigid and non-porous obstacles compared to live plant canopies as shown in Chapter 4. The empirical model parameter  $m$ , which is needed to predict the peak stress ratio  $\tau_S''/\tau$ , was found to be impracticably defined and a new more physically based definition was suggested (Eq. (5.14)). The new  $a$ -parameter was found to be independent of the roughness density  $\lambda$  and the free stream velocity  $U_\delta$  (Fig. 5.10) unlike  $m$  (Fig. 5.8) which makes it much easier to determine  $a$  than  $m$  for individual roughness elements. A method was suggested to determine  $a$  for various roughness elements by using a relatively simple experimental setup. This will allow the first systematic quantification of the sheltering effect of different plant species with relatively simple methods. An accurate prediction of the peak shear stress  $\tau_S''/\tau$  is needed because  $\tau_S''$  determines the onset of sediment erosion on a partially sheltered surface. An important goal for revegetation projects is to find the lowest possible roughness density which still provides a sufficient sheltering effect. This significantly reduces the amount of plants needed and therewith the costs. Precisely determined values for the  $a$ -parameter are thus particularly important for both practical applications and the modelling of wind erosion.



## 7 Limitations and outlook

Some limitations to these investigations of the sheltering effect of live plants against wind erosion compared to real natural conditions need to be mentioned:

First, the live plant canopies used in the wind tunnel differ in important ways from natural vegetation canopies. Natural vegetation canopies typically consist of various plant species with different sizes that are irregularly distributed on the ground. However, the fact that our plants are of similar size, trimmed to a standard height, and arranged with regular spacing, allowed us to systematically investigate the influence of the canopy density and the plant's flexibility and porosity on the sheltering effect. Furthermore, the live plant canopies used here are far closer to natural plant canopies than any roughness array used in previous systematic wind-tunnel investigations of shear-stress partitioning, and results are expected to be similar for other plant species with comparable morphology. The regular spacing of the plants in the wind tunnel may even be beneficial, considering that seeding machines typically used in revegetation projects arrange the plants in regular arrays.

A second important limitation was the lack of driftable sediment in these wind tunnel studies. The surface shear-stress distributions measured in the absence of drifting sand or snow may differ from the surface shear stress for real erosive conditions. Drifting particles interact with the boundary-layer and cause deceleration of the airflow within the saltation layer resulting in slightly lower surface shear stresses than those measured in the absence of drifting sediment. However, the influence of drifting particles is assumed to be similar for the different setups investigated in this study with minor influence on the quantification of the sheltering effect of different roughness elements and canopy densities against wind erosion.

Finally, the topography of a natural surface changes when erosion and deposition take place, resulting in changes to the local wind field and the surface shear-stress distribution. However, the magnitude of this effect depends on the magnitude of the surface topography changes which in turn depend on additional factors such as soil properties and the frequency of changes in the wind direction. Thus the decision was taken not to venture into this additional vast parameter field.

Future work on the quantification of the sheltering effect of live plants against wind erosion may incorporate detailed investigations of the sheltering effect of various plant species. Different plant morphologies may result in strong variations in individual sheltering

effects. Highly flexible plants, as used in this study, certainly result in a different sheltering effect than a rigid shrub. Also the plant shape, e.g. the plants dimensions close to the ground may have a strong influence on the strength of the flow deflection and thus on the local peak and average surface shear stresses. Such information about individual sheltering capabilities of different plant species may be very useful for revegetation projects worldwide. Beside the plants durability against climatic conditions, its ability to prevent wind erosion will be the major decision criteria when choosing suitable species for the revegetation of arid regions. The modifications of Raupach's shear stress partitioning model presented in this dissertation will allow for the first time investigation of the sheltering capability of various plant species with relatively simple methods.

Further, improvements to the Raupach model may be accomplished by adding additional parameters to quantify the increase in the horizontal coverage of the surface and the fluttering capability of flexible plants at higher wind velocities. The horizontal coverage together with the fluttering of the plants was found to be the reason for unexpected difference in sheltering capability between the plant and the block experiments at different roughness densities (Fig. 5.5 and Fig. 5.6). This effect was not captured by the model so far, but might be solved by adding additional parameters describing the flexibility of the plants.

Finally, the research results on shear stress partitioning presented in this dissertation are another step towards a comprehensive description of the sheltering effect of vegetation against wind erosion. Precise predictions of the sheltering effect of plants are important to identify reasonable and sustainable counteractive measures against wind erosion. Particularly revegetation projects in regions where land degradation, desertification and increased particulate matter concentrations in the atmosphere have considerable impact on the ecosystem and human societies will benefit from simplified and improved predictions of the sheltering effect of plants. Furthermore, numerical modelling of aeolian processes becomes more and more important in times of global warming. Experiments such as those presented in this dissertation provide indispensable data for model validation as well as values for model parameters needed to run reasonable simulations.

## List of symbols:

$A$  = effective shelter area

$A_f$  = roughness element frontal area

$C_R$  = roughness element drag coefficient

$C_S$  = surface drag coefficient

$D$  = average roughness element diameter

$Q$  = mass transport rate

$R^2$  = coefficient of determination

$Re_h = U_\delta h/\nu$  = roughness element Reynolds number

$S$  = ground area per roughness element

$S'$  = exposed surface area per roughness element

$U_h$  = mean velocity at top of roughness elements

$U_\delta$  = free-stream velocity

$U_s$  = wind speed at Irwin sensor-tube height

$\langle U_i \rangle$  = spatiotemporally averaged velocity inside canopy

$V$  = effective shelter volume

$a = \tau_S''/\tau_S'$  peak-mean stress ratio

$a_i$  = fit parameters

$b$  = roughness element width

$b_i$  = fit parameters

$c, c_i, c'$  and  $c''$  = constants defined where used

$d$  = sand grain diameter

$f$  = 20 kHz = hot-film sampling frequency

$f_c$  = cut off frequency

$h$  = roughness element height

- $h_s$  = Irwin sensor tube height  
 $m$  = parameter relating  $\tau_s''$  to  $\tau_s'$   
 $\Delta p$  = pressure difference measured by Irwin sensor  
 $\Delta p'$  = fluctuations over pressure signal  
 $u$  = mean streamwise wind velocity  
 $u'$  = fluctuations in mean streamwise wind velocity  
 $u_* = (\tau/\rho)^{1/2}$  = friction velocity  
 $u_{*t}$  = fluid threshold friction velocity  
 $u_\tau$  = skin friction velocity  
 $u_\tau = (\tau_s/\rho)^{1/2}$  = skin friction velocity  
 $u_{\tau t}$  = fluid threshold skin friction velocity  
 $\overline{u'w'}$  = kinematic Reynolds stress  
 $w'$  = fluctuations in mean vertical wind velocity  
 $z_0$  = aerodynamic roughness length  
 $\beta_c$  = Irwin sensor calibration constant  
 $\beta = C_R/C_S$  = roughness element to surface drag ratio  
 $\lambda = A_f/S$  = roughness density  
 $\nu \approx 1.5 \times 10^{-5} \text{ m}^2 \text{ s}^{-1}$  = kinematic viscosity of air  
 $\Phi$  = force on single roughness element  
 $\psi$  = percentage of time that threshold skin friction velocity is exceeded  
 $\rho$  = density of air  
 $\sigma$  = ratio of roughness element basal to frontal area  
 $\sigma_u$  = standard deviation of wind speed  $U_s$   
 $\tau = \rho u_*^2$  = total shear-stress averaged over entire canopy  
 $\tau_R$  = shear-stress acting on roughness elements  
 $\tau_S$  = spatiotemporally-averaged surface shear stress on area  $S$   
 $\tau_S(t, x, y)$  = local shear-stress acting on surface  
 $\tau_S'$  = spatiotemporally-averaged surface shear-stress on exposed surface area  $S'$   
 $\tau_S''$  = spatial peak of temporally-averaged surface shear-stress distribution  
 $\tau_{S0}$  = spatiotemporally-averaged surface shear-stress in the absence of roughness elements  
 $\xi$  = normalized turbulence intensity



## Bibliography:

- (1) Ambühl D (2004) Simulation of an atmospheric boundary-layer in a wind tunnel. Term Paper, Institute of Fluid Dynamics, ETH Zürich, pp. 56
- (2) Anderson RS, Sorensen M (1991) A review of recent progress in our understanding of aeolian sediment transport. *Acta Mech* 1:1-19
- (3) Arya SPS (1975) A Drag Partition Theory for Determining the Large-Scale Roughness Parameter and Wind Stress on the Arctic Pack Ice. *J Geophys Res.* 80:3447-3454
- (4) Bagnold R (1943) *The physics of blown sand and desert dunes.* Meghuen, London
- (5) Brown S, Nickling WG, Gillies JA (2008) A wind tunnel examination of shear stress partitioning for an assortment of surface roughness distributions. *J Geophys Res.* doi:10.1029/2007JF000790
- (6) Bruun HH (1995) *Hot-Wire Anemometry, principles and signal analysis.* Oxford Science Publications.
- (7) Burri K, Gromke C, Graf F (2011a) Mycorrhizal fungi protect the soil from wind erosion: a wind tunnel study. *Land Degrad Dev.* doi:10.1002/ldr.1136
- (8) Burri K, Gromke C, Lehning M, Graf F (2011b) Aeolian sediment transport over vegetation canopies: A wind tunnel study with live plants. *Aeolian Res* 3:205-213
- (9) Burri K (2011c) *Plants and Mycorrhizal Fungi on Wind Erosion Control.* Dissertation, ETH Zürich. doi:10.3929/ethz-a-006570793
- (10) Clifton A, Lehning M (2008) Improvement and validation of a snow saltation model using wind tunnel measurements. *Earth Surface Process Landf* 33:2156-2173. doi:10.1002/Esp.1673
- (11) Clifton A, Manes C, Ruedi JD, Guala M, Lehning M (2008) On shear-driven ventilation of snow. *Boundary-Layer Meteorol* 126:249-261
- (12) Clifton A, Ruedi JD, Lehning M (2006) Snow saltation threshold measurements in a drifting-snow wind tunnel. *J Glaciol* 52 (179):585-596
- (13) Clifton A (2007) *Wind tunnel investigations of boundary-layer conditions before and during snow drift.* Dissertation. ETH Zürich, 10.3929/ethz-a-005420531.
- (14) Crawley DM, Nickling WG (2003) Drag partition for regularly-arrayed rough surfaces. *Boundary-Layer Meteorol* 107:445-468

- (15) Durgin FH, (1992) Pedestrian level wind studies at the Wright brothers' facility. *Journal of Wind Engineering and Industrial Aerodynamics* 44, 2253-2264
- (16) Gillette DA, Stockton PH (1989) The effect of nonerodible particles on wind erosion of erodible surfaces. *Journal of Geophysical Research* 94:12,885-12,893
- (17) Gillies JA, Nickling WG, King J (2002) Drag coefficient and plant form response to wind speed in three plant species: Burning Bush (*Euonymus alatus*), Colorado Blue Spruce (*Picea pungens glauca.*), and Fountain Grass (*Pennisetum setaceum*). *Journal of Geophysical Research* doi:10.1029/2001JD001259
- (18) Gillies JA, Nickling WG, King J (2007) Shear stress partitioning in large patches of roughness in the atmospheric inertial sublayer. *Boundary-Layer Meteorology*. 122:367-396
- (19) Gromke C, Ruck B, (2005) Die Simulation atmosphärischer Grenzschichten in Windkanälen, 13. GALA Fachtagung, Cottbus, Germany, 51-1 – 51-8
- (20) Gromke C, (2009) Einfluss von Bäumen auf die Durchlüftung von innerstädtischen Strassenschluchten, Dissertation, Institut für Hydromechanik, Universität Karlsruhe, pp. 142
- (21) Gromke C, Manes C, Walter B, Lehning M, Guala M (2011) Aerodynamic roughness length of fresh snow. *Boundary-Layer Meteorology* doi:10.1007/s10546-011-9623-3
- (22) Gromke C, Ruck B (2008) Aerodynamic modelling of trees for small-scale wind tunnel studies. *Forestry* 81:243-258
- (23) Grosse S, Schröder W (2009) The Micro-Pillar Shear-Stress Sensor MPS3 for Turbulent Flow. *Sensors* 9, 2222-2251
- (24) Guala M, Manes C, Clifton A, Lehning M (2008) On the saltation of fresh snow in a wind tunnel: Profile characterization and single particle statistics. *Journal of Geophysical Research: Earth Surface* 113:F03024
- (25) Haritonidis JH (1989) The measurement of wall shear-stress. *Advances in Fluid Mechanics Measurements* A90-30668 12-34, 229-261
- (26) Ho CM, Tai YC (1998) Micro-Electro-Mechanical-Systems (MEMS) and Fluid Flows. *Annual Review of Fluid Mechanics* 30, 579-612
- (27) Irwin HPAH (1981) A Simple Omnidirectional Sensor for Wind-Tunnel Studies of Pedestrian-Level Winds. *Journal of Wind Engineering and Industrial Aerodynamics* 7:219-239
- (28) Kaimal JC, Finnigan JJ (1994) *Atmospheric Boundary-layer Flows – Their Structure and Measurements*, Oxford University Press, pp. 289
- (29) Kim DS, Cho GH, White BR (2000) A wind-tunnel study of atmospheric boundary-layer flow over vegetated surfaces to suppress PM<sub>10</sub> emission on Owens (dry) Lake. *Boundary-Layer Meteorology* 97:309-329
- (30) King J, Nickling WG, Gillies JA (2006) Aeolian shear stress ratio measurements within mesquite-dominated landscapes of the Chihuahuan Desert, New Mexico, USA. *Geomorphology* 82:229-244
- (31) Lakehal D, Rodi W (1997) Calculation of the flow past a surface-mounted cube with two-layer turbulence models. *Journal of Wind Engineering and Industrial Aerodynamics* 67&68, 65-78.
- (32) Lancaster N, Baas A (1998) Influence of vegetation cover on sand transport by wind: Field studies at Owens Lake, California. *Earth Surf Processes and Landforms* 23:69-82
- (33) Lyles L, Allison BE (1975) Wind erosion: Uniformly spacing nonerodible elements eliminates effects of wind direction variability. *Journal of Soil and Water Conservation* 30:225-226
- (34) Marshall JK (1971) Drag Measurements in Roughness Arrays of Varying Density and Distribution. *Agricultural Meteorology* 8:269-292

- (35) Martinuzzi R, Tropea C (1993) The Flow Around Surface-Mounted, Prismatic Obstacles Placed in a Fully Developed Channel Flow. *Journal of Fluids Engineering* 115, 85-92
- (36) Musick HB, Gillette DA (1990) Field Evaluation of Relationships between a Vegetation Structural Parameter and Sheltering against Wind Erosion. *Land Degradation and Rehabilitation* 2:87-94
- (37) Musick HB, Trujillo SM, Truman CR (1996) Wind-Tunnel Modelling of the Influence of Vegetation Structure on Saltation Threshold. *Earth Surface Processes and Landforms* 21:589-605
- (38) Morris HM (1955) Flow in rough conduits. *American Society of Civil Engineers* 120:373-398
- (39) Preston JH (1953) The determination of turbulent skin friction by means of pitot tubes. *Journal of Royal Aeronautical Society* 71, 52-53
- (40) Raupach MR, Antonia RA, Rajagopalan S (1991) Rough-wall turbulent boundary-layers, *Applied Mechanical Review* 44:1-25
- (41) Raupach MR (1992) Drag and Drag Partition on Rough Surfaces. *Boundary-Layer Meteorology* 60:375-395
- (42) Raupach MR, Gillette DA, Leys JF (1993) The Effect of Roughness Elements on Wind erosion Threshold. *Journal of Geophysical Research* 98:3023-3029
- (43) Raupach MR, Finnigan JJ, Brunet Y (1996) Coherent eddies and turbulence in vegetation canopies: the mixing-layer analogy. *Boundary-Layer Meteorology* 78:351-383
- (44) Schlichting H (1936) Experimental investigations of the problem of surface roughness. *NASA Technical Memo* 823, Washington, D.C.
- (45) Schultz MP, Flack KA (2007) The rough-wall turbulent boundary-layer from the hydraulically smooth to the fully rough regime. *Journal of Fluid Mechanics* 580, pp 381-405
- (46) Shao Y, Yang, Y (2005) A scheme for drag partition over rough surfaces. *Atmospheric Environment* 39:7351-7361
- (47) Shao Y, Yang, Y (2008) A theory for drag partition over rough surfaces. *Journal of Geophysical Research* 113:F02S05
- (48) Shao Y (2008) *Physics and Modelling of Wind Erosion*. Springer ISBN:978-1-4020-8894-0
- (49) Stull RB (1988) *An introduction to boundary-layer meteorology*. Kluwer Academic Publishers, Boston.
- (50) Sutton SLF, McKenna-Neumann C (2008). Variation in bed level shear-stress on surfaces sheltered by nonerodible roughness elements. *Journal of Geophysical Research* doi:10.1029/2007JF000967
- (51) Valyrakis M, Diplas P, Dancy C, Greer K, Celik AO (2010) Role of instantaneous force magnitude and duration on particle entrainment. *Journal of Geophysical Research* doi:10.1029/2008JF001247
- (52) Walter B, Gromke C, Lehning M (2009) The SLF Boundary-layer Wind Tunnel - An Experimental Facility for Aerodynamical Investigations of Living Plants. 2<sup>nd</sup> Int Conf Wind Eff Trees, Freiburg, Germany
- (53) Walter B (2011) [http://www.swiss-experiment.ch/index.php/Irwin\\_sensor\\_accuracy](http://www.swiss-experiment.ch/index.php/Irwin_sensor_accuracy), last update: 2011-11-30
- (54) Walter B, Gromke C, Leonard K, Clifton A, Lehning M (2012a) Spatially resolved skin friction velocity measurements using Irwin sensors: A calibration and accuracy analysis. *Journal of Wind Engineering and Industrial Aerodynamics* doi:10.1016/j.jweia.2012.02.018

- (55) Walter B, Gromke C, Leonard K, Manes C, Lehning M (2012b) Spatio-temporal surface shear stress variability in live plant canopies and cube arrays. *Boundary-Layer Meteorology* doi:10.1007/s10546-011-9690-5
- (56) Walter B, Gromke C, Lehning M (2012c) Shear stress partitioning in live plant canopies and modifications to Raupach's model. *Boundary-Layer Meteorology*, doi:10.1007/s10546-012-9719-4
- (57) Wissink JG (2006) Large Eddy Simulation in Fluid Mechanics, lectural notes, Institute for Hydromechanics, University of Karlsruhe (KIT), Germany, pp. 49
- (58) Wolfe SA, Nickling WG (1996) Shear Stress Partitioning in Sparsely Vegetated Desert Canopies. *Earth Surface Processes and Landforms* 21:607-619
- (59) Wooding RA, Bradley EF, Marshall JK (1973) Drag due to Regular Arrays of Roughness Elements of Varying Geometry. *Boundary-Layer Meteorology* 5:285-308
- (60) Wu H, Stathopoulos T (1993) Further experiments on Irwin's wind sensor. *Journal of Wind Engineering and Industrial Aerodynamics* 53:441-452
- (61) Wyatt VE, Nickling WG (1997) Drag and shear stress partitioning in sparse desert creosote communities. *Canadian Journal of Earth Sciences* 34:1486-1498

# Curriculum vitae

## Personal

Benjamin Andreas Walter

Born on February 14<sup>th</sup>, 1982 in Wolfach im Kinzigtal, Germany

German Citizen.

## Education

- 2008-2012 Ph.D student at the WSL Institute for Snow and Avalanche Research SLF Davos. Dissertation: Wind tunnel studies of shear stress partitioning in live plant canopies
- 2007-2008 Academic studies: Physics (Diploma), Karlsruhe Institute of Technology and Fraunhofer Institute for solar energy systems, Freiburg: Diploma thesis: Quantitative analysis of spatially resolved Lock-In-Thermography measurements for the characterization of silicon solar cells
- 2002-2007 Academic studies: Physics (Diploma), Karlsruhe Institute of Technology (KIT)

## Scientific publications

### Peer-reviewed

Kasemann M, Walter B, Meinhardt C, Ebser J, Kwapil W, Warta W (2008) Emissivity-corrected power loss calibration for lock-in thermography measurements on silicon solar cells, *Journal of Applied Physics*, 103:11, 113503-113503-8

Kasemann M, Walter B, Warta W (2009) Reliable hot-spot classification in 10 ms using ultra-fast lock-in thermography, *Progress in photovoltaics: Research and applications*, 17:441–450

Gromke C, Manes C, Walter B, Lehning M, Guala M (2011) Aerodynamic roughness length of fresh snow. *Boundary-Layer Meteorology*, doi:10.1007/s10546-011-9623-3

Walter B, Gromke C, Leonard K, Clifton A, Lehning M (2012a) Spatially resolved skin friction velocity measurements using Irwin sensors: A calibration and accuracy analysis. *Journal of Wind Engineering and Industrial Aerodynamics*, doi:10.1016/j.jweia.2012.02.018

Walter B, Gromke C, Leonard K, Manes C, Lehning M (2012b) Spatio-temporal surface shear-stress variability in live plant canopies and cube arrays. *Boundary-Layer Meteorology*, doi:10.1007/s10546-011-9690-5

Walter B, Gromke C, Leonard K, Manes C, Lehning M (2012c) Shear stress partitioning in live plant canopies and modifications to Raupach's model. *Boundary-Layer Meteorology*, doi:10.1007/s10546-012-9719-4

### **Conference proceedings**

Walter B, Kasemann M, Grote D, Ebser J, Kwapil W, Warta W (2008) Verification of Power Loss Mechanisms Contributing to the Illuminated Lock-In Thermography (ILIT) Signal, 23<sup>rd</sup> European Photovoltaic Solar Energy Conference and Exhibition Valencia, Spain

Kasemann M, Kwapil M, Schubert M, Habenicht H, Walter B, The M, + (2008) Spatially resolved silicon solar cell characterization using infrared imaging methods, In: Proceedings of the 33<sup>rd</sup> IEEE Photovoltaic Specialists Conference, PVSC, San Diego, CA

Walter B, Gromke C, Lehning M (2009) The SLF Boundary-layer Wind Tunnel - An Experimental Facility for Aerodynamical Investigations of Living Plants. In: Proceedings of the 2<sup>nd</sup> International Conference on Wind Effects on Trees, Freiburg, Germany

Gromke C, Walter B, Manes C, Lehning M, (2009) Aerodynamic roughness lengths of snow. In: Proceedings of the International Conference on Alpine Meteorology, Rastatt, Germany

Gromke C, Guala M, Manes C, Walter B, Lehning M, (2009) Aerodynamic and surface characteristic length scales of snow covered flat planes. In: Proceedings of the International Snow Science Workshop ISSW, Davos, Switzerland

Walter B, Gromke C, Leonard K, Clifton A, Lehning M (2011) Measurements of surface shear stress distribution in live plant canopies. In: Proceedings of the 13<sup>th</sup> International Conference on Wind Engineering ICWE13, Amsterdam, The Netherlands

### **Oral presentations at International conferences**

Walter B, Gromke C, Lehning M (2009) The SLF Boundary-layer Wind Tunnel - An Experimental Facility for Aerodynamical Investigations of Living Plants. At the 2<sup>nd</sup> International Conference on Wind Effects on Trees, Freiburg, Germany

Walter B, Gromke C, Leonard K, Clifton A, Lehning M (2011) Measurements of surface shear stress distribution in live plant canopies. At the 13<sup>th</sup> International Conference on Wind Engineering ICWE13, Amsterdam, The Netherlands

Walter B, Gromke C, Leonard K, Lehning M (2011) Wind tunnel measurements of spatial and temporal surface shear stress variations in live plant canopies and in rigid cube arrays. At the Coherent flow structures in geophysical flows at earth's surface conference, Simon Fraser University, Burnaby, British Columbia